Design and Implementation of a Depth-Dependent Matched Filter to Maximize Signal-to-Noise Ratio in Optical Coherence Tomography

by

Ameneh Boroomand

A thesis submitted to the Faculty of Graduate Studies of
The University of Manitoba
in partial fulfillment of the requirements of the degree of

MASTER OF SCIENCE

Department of Electrical and Computer Engineering
University of Manitoba
Winnipeg, MB, Canada

To my wonderful parents for all their support

Abstract

Obtaining higher depth of imaging is an important goal in Optical Coherence Tomography (OCT) systems. One of the main factors that affect the depth of OCT imaging is the presence of noise. That's why the study of noise statistics is an important problem. In the first part of this thesis we obtain an empirical estimate of the second order statistics of noise by using a sequence of Time domain (TD) OCT images. These estimates confirm the non-stationary nature of noise in TD-OCT. In the second part of the thesis these estimates are used to design a depth-dependent matched filter to maximize the Signal-to-Noise Ratio (SNR) and increase the Contrast-to-Noise Ratio (CNR) in TD-OCT. By applying our filter to TD-OCT images of both vascular rabbit tissue and a human tooth, both SNR and CNR were increased and a higher imaging depth was achieved.

Acknowledgements

First and foremost, I would like to thank Dr. Sherif Sherif, my research advisor, for his help and support. He always provided me with helpful suggestions and ideas to overcome the problems that I encountered along my work.

I thank Dr. Michael Sowa, Dr. Dan. Popescu and Dr. Michael Smith, the members of Institute for Bio-diagnostics (IBD) group at National Research Council Canada (NRC), for their contribution in this work and their support to provide our OCT images.

I also thank Dr. Zahra Mousavi, Dr. Jitendra Paliwal and Dr. Dan Popescu, my committee members, for their effort to evaluate this work.

I would like to thank my family and friends for their continual support.

Table of Contents

Abstract i

Acknowledgements ii

List of Figures vi

List of Tables xii

Abbreviations xiii

1. Introduction 1

2. Theoretical Analysis of OCT 5

- 2.1 OCT principles 5
  - 2.1.1 Coherence of light 6
  - 2.1.2 Low coherence interferometry 6
  - 2.1.3 Scanning modes in OCT 9
- 2.2 Different types of OCT systems 10
  - 2.2.1 Time domain OCT 10
  - 2.2.2. Frequency domain OCT 14
- 2.3 Resolution in OCT imaging 18

3. Image Processing in OCT 20

- 3.1 Source of noise in TD-OCT 21
  - 3.1.1 TD-OCT system noise 21
  - 3.1.2 Speckle noise in OCT images 24
- 3.2 Source of artifacts in OCT images 25
- 3.3 Image processing in OCT 26
  - 3.3.1 Deconvolution methods in OCT 26
  - 3.3.2 Speckle noise reduction methods 31
  - 3.3.3 Dispersion compensation in OCT 33
  - 3.3.4 Distortion removal of OCT image 35

4. Statistical Modeling of Depth-Scan Photocurrent in TD-OCT System 37

4.1 Statistical model of depth scan photocurrent in TD-OCT 38

4.2 TD-OCT with direct optical detection 39

4.2.1 Mean of photocurrent in direct light detection configuration............................41

4.2.2 Autocorrelation Function of the photocurrent in direct light detection configuration...45

4.3 TD-OCT with differential optical detection 47

4.3.1 Mean of photocurrent in differential light detection configuration...................47

4.3.2 Autocorrelation function of photocurrent in differential light detection configuration...49

4.4 Joint PDF of TD-OCT photocurrent and effect of thermal electronic fluctuations 50

4.5 Signal dependent noise in TD-OCT 51

5. Empirical Estimation and Verification of Noise Statistics in TD-OCT..................53

5.1 TD-OCT setup 54

5.2 Empirical estimation and verification of photocurrent statistics............................ 58

5.3 Results of estimated photocurrent noise covariance matrix................................... 59

5.4 Constructing an OCT image using depth-scan photocurrents................................ 66

5.5 Post-processing of depth-scan photocurrent in TD-OCT....................................... 68

5.6 Relation between SNR value in depth-scan photocurrent and its corresponding envelope 69

5.7 Empirical estimation and verification of noise statistics for photocurrent envelope 71

6. Depth-Dependent Matched Filter..81

6.1 Theory of matched filter... 82

6.2 Depth-dependent matched filter for single depth-scan envelope............................ 85

6.3 SNR analysis method and CNR calculation... 89

6.4 Results of applying depth-dependent matched filter on OCT images 91

6.4.1 Discussion of imaging results for rabbit vascular tissue 107

6.4.2 Discussion of imaging results for a human tooth 123

7. Conclusions & Future work...126

7.1 Conclusions 126
7.2 Future work 127

References...128

Appendix A...136

A.1 SNR relation of input and output of envelope detector....................................... 136

Appendix B...141

List of Figures

Figure 2.1: General configuration of a typical time-domain oct system 7

Figure 2.2: A typical OCT signal 9

Figure 2.3: An example of A-scan and B-scan in TD-OCT 10

Figure 2.4: A typical TD-OCT setup with direct optical detection 11

Figure 2.5: A sample of photocurrent signal acquired in TD-OCT system 13

Figure 2.6: A typical TD-OCT configuration with differential optical detection setup 14

Figure 2.7: A typical configuration of a SD-OCT system 15

Figure 2.8: A typical configuration for an SS-OCT system 17

Figure 4.1: Input-output model of an optical photo-detector 39

Figure 4.2: A typical TD-OCT setup with direct optical detection 42

Figure 4.3: A typical TD-OCT setup with differential optical detection 47

Figure 5.1: A sample of TD-OCT image of vascular rabbit tissue. 56

Figure 5.2: A sample of TD-OCT of fishing-line imaged along its length direction. 57

Figure 5.3: A sample of TD-OCT of fishing-line imaged along its width direction. 58

Figure 5.4: Ensemble average of a depth-scan photocurrent of vascular rabbit tissue, (b) diagonal elements of covariance matrix for the depth-scan photocurrent of part (a). 60

Figure 5.5: Empirical estimates of noise covariance matrix of a depth-scan photocurrent of vascular rabbit tissue at different ranges of imaging depth. 61

Figure 5.6: Diagonal elements of covariance matrix in different ranges of imaging depth. 62

Figure 5.7: (a) An arbitrary depth-scan photocurrent of vascular rabbit tissue, (b) diagonal elements of the covariance matrix for the depth-scan photocurrent of part (a). 63

Figure 5.8: Empirical estimates of noise covariance matrix of depth-scan photocurrent of vascular rabbit tissue at different ranges of imaging depth. 64

Figure 5.9: Diagonal elements of covariance matrix at different ranges of imaging depth. 65

Figure 5.10: (a) A sample of depth-scan photocurrent of vascular rabbit tissue, (b) corresponding depth-scan photocurrent envelope. 66

Figure 5.11: (a) A sample of depth-scan photocurrent of vascular rabbit tissue, (b) corresponding depth-scan photocurrent envelope. 67

Figure 5.12: (a) A sample of constructed OCT image of rabbit vascular tissue using a set of 650 photocurrent envelopes. 68

Figure 5.13: Block diagram of common post-processing stage in a TD-OCT system. 69

Figure 5.14: Block diagram of an envelope detector. 70

Figure 5.15: (a) A sample of depth-scan photocurrent envelope of vascular rabbit tissue, (b) diagonal elements of covariance matrix for photocurrent envelope of part (a). 72

Figure 5.16: Estimates of local covariance matrix of a depth-scan envelope of vascular rabbit tissue at different ranges of imaging depth. 73

Figure 5.17: Diagonal elements of covariance matrix of a depth-scan envelope of vascular rabbit tissue at different ranges of imaging depth. 74

Figure 5.18: (a) A sample of depth-scan photocurrent of a fishing-line imaged along its length, (b) diagonal elements of the covariance matrix of the photocurrent envelope of part (a). 75

Figure 5.19: Estimates of local covariance matrices of a depth-scan envelope of a fishing line imaged along its length direction and for different ranges of imaging depth. 76

Figure 5.20: Diagonal elements of covariance matrix of a depth-scan envelope of a fishing line imaged along its length direction at different ranges of imaging. 77

Figure 5.21: A sample of depth-scan photocurrent envelope of a fishing-line imaged along its width direction, (b) diagonal elements of covariance matrix of photocurrent envelope of part (a). 78

Figure 5.22: Estimates of local covariance matrices of a depth-scan envelope of a fishing line imaged along its width direction and for different ranges of imaging depth. 79

Figure 5.23: Diagonal elements of covariance matrix of a fishing line imaged along its width direction at different ranges of imaging depth. 80

Figure 6.1: A block diagram of a matched filter. 82

Figure 6.2: (a) Averaged OCT image; (b) averaged depth-scan envelope of vascular rabbit tissue; (c) noise power; (d) SNR; (e) contrast;(f) CNR values of averaged depth-scan envelope of part (b). 93

Figure 6.3: (a) Filtered OCT image; (b) filtered depth-scan envelope of vascular rabbit tissue (window size 3 pixels); (c) noise power; (d) SNR; (e) contrast; (f) CNR values of filtered depth-scan envelope of part (b). 94

Figure 6.4: (a) Filtered OCT image; (b) filtered depth-scan envelope of vascular rabbit tissue (window size 5 pixels); (c) noise power; (d) SNR; (e) contrast; (f) CNR values of filtered depth-scan envelope of part (b). 95

Figure 6.5: (a) Filtered OCT image; (b) filtered depth-scan envelope of vascular rabbit tissue (window size 7 pixels); (c) noise power; (d) SNR; (e) contrast; (f) CNR values of filtered depth-scan envelope of part (b). 96

Figure 6.6: (a) Filtered OCT image; (b) filtered depth-scan envelope of vascular rabbit tissue (window size 9 pixels); (c) noise power; (d) SNR; (e) contrast; (f) CNR values of filtered depth-scan envelope of part (b). 97

Figure 6.7: (a) Filtered OCT image; (b) filtered depth-scan envelope of vascular rabbit tissue (window size 11 pixels); (c) noise power; (d) SNR; (e) contrast; (f) CNR values of filtered depth-scan envelope of part (b). 98

Figure 6.8: (a) Filtered OCT image; (b) filtered depth-scan envelope of vascular rabbit tissue (window size 13 pixels); (c) noise power; (d) SNR; (e) contrast; (f) CNR values of filtered depth-scan envelope of part (b). 99

Figure 6.9: (a) Filtered OCT image; (b) filtered depth-scan envelope of vascular rabbit tissue (window size 15 pixels); (c) noise power; (d) SNR; (e) contrast; (f) CNR values of filtered depth-scan envelope of part (b). 100

Figure 6.10: (a) Filtered OCT image; (b) filtered depth-scan envelope of vascular rabbit tissue (window size 17 pixels); (c) noise power; (d) SNR; (e) contrast; (f) CNR values of filtered depth-scan envelope of part (b). 101

Figure 6.11: (a) Filtered OCT image; (b) filtered depth-scan envelope of vascular rabbit tissue (window size 19 pixels); (c) noise power; (d) SNR; (e) contrast; (f) CNR values of filtered depth-scan envelope of part (b). 102

Figure 6.12: QM values of SNR plots of filtered depth-scan envelope of vascular rabbit tissue with different window sizes (3-19 pixels). 105

Figure 6.13: QM values of CNR plots of filtered depth-scan envelopes of vascular rabbit tissue for different window sizes (3-19 pixels). 107

Fig 6.14: (a) Averaged OCT image; (b) averaged depth-scan envelope of a human tooth; (c) noise power; (d) SNR;(e) contrast; (f) CNR values of averaged depth-scan envelope of part (b). 110

Figure 6.15: (a) Filtered OCT image; (b) filtered depth-scan envelope of a human tooth (window size 3 pixels); (c) noise power; (d) SNR; (e) contrast; (f) CNR values of filtered depth-scan envelope of part (b)..111

Figure 6.16: (a) Filtered OCT image; (b) filtered depth-scan envelope of a human tooth (window size 5 pixels); (c) noise power; (d) SNR; (e) contrast; (f) CNR values of filtered depth-scan envelope of part (b)..112

Figure 6.17: (a) Filtered OCT image; (b) filtered depth-scan envelope of a human tooth (window size 7 pixels); (c) noise power; (d) SNR; (e) contrast; (f) CNR values of filtered depth-scan envelope of part (b)..113

Figure 6.18: (a) Filtered OCT image; (b) filtered depth-scan envelope of a human tooth (window size 9 pixels); (c) noise power; (d) SNR; (e) contrast; (f) CNR values of filtered depth-scan envelope of part (b)..114

Figure 6.19: (a) Filtered OCT image; (b) filtered depth-scan envelope of a human tooth (window size 11 pixels); (c) noise power; (d) SNR; (e) contrast; (f) CNR values of filtered depth-scan envelope of part (b)..115

Figure 6.20: (a) Filtered OCT image; (b) filtered depth-scan envelope of a human tooth (window size 13 pixels); (c) noise power; (d) SNR; (e) contrast; (f) CNR values of filtered depth-scan envelope of part (b)..116

Figure 6.21: (a) Filtered OCT image; (b) filtered depth-scan envelope of a human tooth (window size 15 pixels); (c) noise power; (d) SNR; (e) contrast; (f) CNR values of filtered depth-scan envelope of part (b)..117

Figure 6.22: (a) Filtered OCT image; (b) filtered depth-scan envelope of a human tooth (window size 17 pixels); (c) noise power; (d) SNR; (e) contrast; (f) CNR values of filtered depth-scan envelope of part (b).......118

Figure 6.23: (a) Filtered OCT image; (b) filtered depth-scan envelope of a human tooth (window size 19 pixels); (c) noise power; (d) SNR; (e) contrast; (f) CNR values of filtered depth-scan envelope of part (b).......119

Figure 6.24: QM values of SNR plots of filtered depth-scan envelopes of a human tooth for different window sizes (3-19 pixels).......121

Figure 6.25: QM values of CNR plots of filtered depth-scan envelopes of a human tooth for different window sizes (3-19 pixels).......123

Figure A.1: Envelope detector (demodulator) block diagram.......136

Figure A.2: Power spectral densities of $\boldsymbol{nc}(\boldsymbol{t})$ and $\boldsymbol{ns}(\boldsymbol{t})$. 138

Figure A.3: Power spectral densities of $\boldsymbol{nc}(\boldsymbol{t})$ and $\boldsymbol{ns}(\boldsymbol{t})$ after passing through a band-pass filter.......138

List of Tables

Table 6. 1: Mean; variance and QM values of SNR plots of averaged depth-scan envelope and filtered depth-scan envelopes of vascular rabbit tissue. 104

Table 6. 2: Mean; variance and QM values of CNR plots of averaged depth-scan envelope and filtered depth- scan envelopes of vascular rabbit tissue. 106

Table 6. 3: Mean; variance and QM values of SNR plots of averaged depth-scan envelope and filtered depth- scan envelopes of a human tooth. 120

Table 6. 4: Mean; variance and QM values of CNR plots of averaged depth-scan envelope and filtered depth- scan envelopes of a human tooth. 122

Abbreviations

OCT	Optical Coherence Tomography
TD-OCT	Time-domain optical coherence tomography
SD-OCT	Spectral Domain OCT
SS–OCT	Swept Source OCT
LCI	Low Coherence Interferometry
DG	Diffraction Grating
SNR	Signal-to-Noise Ratio
DFT	Discrete Fourier Transform
LSI	Linear Shift Invariant
PSF	Point Spread Function
CNR	Contrast-to-Noise Ratio
FWHM	Full Width at Half Maximum
SLD	Super Luminescent Diodes
JPDF	Joint Probability Distribution Function
PCA	Principal Component Analysis
FPGA	Field Programmable Gate Array
AM	Amplitude Modulation

Chapter 1

Introduction

Imaging of deeper layers of an object and the ability to better visualize its internal patterns, structures and features is an important goal in different imaging applications. To date, increasing the depth of imaging is an important research goal in imaging systems. Currently, there's much effort to overcome this imaging depth limitation to provide good quality images from higher depths of an object. Achieving this goal would be very useful in different imaging applications.

Optical Coherence Tomography (OCT) is a relatively new and advanced imaging technology that can be used for the depth-resolved noninvasive cross-sectional imaging. This imaging technique was first proposed by Huang [1]. The principle of this imaging method is somewhat similar to ultrasound imaging except that it uses light instead of sound. In comparison with the ultrasound, OCT has less penetration (2 ~ 3 mm) but higher resolution in depth [1]. Both Time-domain optical coherence tomography (TD-OCT) and Spectral-domain OCT use low coherence interferometry to generate subsurface cross-sectional images from internal layers of an imaged object. TD-OCT and SD-OCT imaging is performed by measuring the magnitude and echo time delays of backscattered light that comes from different depths of an object to produce a two-dimensional data set that represents this object [2]. Axial and lateral resolution of OCT images are in the range of few microns (µm) and the penetration depth of imaging is in the range of few mm. One of the main advantages of OCT is its high axial resolution, which is decoupled from its transversal resolution. OCT techniques are divided into two broad methods: Time Domain (TD) and Frequency domain FD-OCT which includes Spectral Domain (SD) and Swept Source (SS) OCT. In Chapter 2 of this thesis, the general principle of OCT systems is explained and different types of OCT techniques are demonstrated in more details.

To date, many applications of OCT systems have been reported. It has been used in wide variety of industrial fields such as surface and thickness measurements, noncontact material characterization of ceramics, glass, polymers, fiber and paper composites, quality evaluation of data storage devices, non destructive testing and also optical sensing with many more application still emerging [3]. The most common application of OCT is in medical imaging, in particular imaging of tissue. It has been applied, as a diagnostic tool, to the study of various biological tissues [4]. In most cases, the aim is to extract specific features of biological tissue by measuring the local reflectivity of backscattered light from its different depths. OCT has found many applications in ophthalmology, dermatology, gastroenterology, dentistry, cardiology and tumor margining [2].

One of the important issues that affect the depth of OCT imaging is the presence of noise. It always degrades the quality of the OCT image and causes difficulties in seeing deeper object structures. Noise in OCT systems can arise from both optical source and optical detector. In addition, OCT images are usually affected by speckle noise due to the multiple scattering of light inside the object.

In Chapter 3 of this thesis, different sources of noise in OCT systems are discussed. All noise types limit the depth of OCT imaging and prevent visualization of microstructures in deeper layers of an object. In most of OCT applications, this is a major problem and may lead to the inaccurate final images. To date much attention has been given to the enhancement and development of new OCT systems with higher depth of imaging. In addition to the improvement of OCT technology, improving post-processing techniques of OCT images is an important topic. To date most of these OCT image processing techniques are deterministic in nature and few of them applied the statistical features of OCT image to process and enhance the OCT image. In previous studies, average SNR of OCT setups was used to evaluate the performance of different OCT experimental configurations [5], [6], [7]. In another study, the statistical properties of speckle noise were extracted from OCT images [8]. Also, a statistical model was proposed for single A-scan photocurrent in a TD-OCT system [5]. In Chapter 3 of this thesis, image processing methods that are applied to OCT images are reviewed and discussed.

Studying the statistical characteristics of noise and its impact on OCT data could be very useful to reduce its negative effect on the OCT image. In Chapter 4 of this thesis, a statistical model of a depth-scan photocurrent that is proposed in [5] is reviewed. In this study, the authors theoretically prove the dependency of depth-scan photocurrent on the OCT signal and correspondingly to the depth of imaging.

The contributions of this thesis are presented in Chapters 5 and 6: first, we empirically estimate and investigate the statistical properties of noise in a TD-OCT system with differential light detection. Second, based on these empirical estimations, we design and implement a statistical filter to maximize the pixel based SNR values of TD-OCT images. .

In Chapter 5, the second order statistics (mean and covariance matrix) of noise are empirically estimated for each A-scan photocurrent and their corresponding envelope. Using these empirical estimates, the dependence of the noise covariance matrix on the photocurrent (or its envelope) is verified and its variation with different imaging depths of imaging is demonstrated. This investigation practically proves the non-stationary characteristic of the depth-scan photocurrent and its corresponding envelope in TD-OCT system. These results confirm the theory reviewed in Chapter 4 about the statistical properties of noise in TD-OCT system. Also presented in this Chapter is a, a relationship showing that the maximization of SNR of the photocurrent results in the maximization of SNR of its envelope.

In Chapter 6, an optimal statistical depth-dependent matched filter is proposed to maximize the value of the SNR value in TD-OCT images. This filter is designed using the empirical estimates of noise statistics discussed in Chapter 5. In Chapter 6, the theory and derivation of general matched filter are also discussed along with our depth-dependent matched filter designed for application to TD-OCT photocurrent envelopes. The results of applying our proposed depth-dependent matched filter on an OCT image of vascular rabbit tissue are presented and discussed at the end of Chapter 6. A general discussion and future work are presented in the last chapter of the thesis.

Chapter 2

Theoretical Analysis of OCT

Optical technology has a long history and has contributed to different types of imaging systems and applications. Optical imaging systems have various applications in medicine since they are typically safe because of the non-ionizing nature of light. OCT is a novel imaging technology that uses low coherence interferometry or wavelength swept lasers to produce high resolution cross-sectional images from the internal microstructures of an object. Since the invention of OCT [1], it has been applied to different medical and industrial applications [2],[3].

2.1 OCT principles

The function of an OCT system is somewhat similar to ultrasound in the sense that it measures the intensity of light that is reflected from different depths of an imaged sample [6]. In ultrasound, back reflected echoes from the internal layers of an object are measured and their time delays are calculated. In OCT, due to the high speed of light, the time delays of reflected light are in order of femtoseconds. Thus it is difficult to calculate these delays. Therefore time-domain OCT systems use an optical interferometer to measure these time delays. As the optical signals reflected from different depths of an object are usually very weak, interfermoetry is a central technique in all types of OCT systems. This could be realized by using either a Michelson or a Mach-Zehnder interferometer, which in time-domain OCT is illuminated by a low coherence light source [5].

2.1.1 Coherence of light

Coherence is one of the primary features of light that quantifies its random nature [7]. There are two broad types of light coherence: spatial and temporal. Temporal coherence is defined as the correlation between an optical field and a delayed version of itself. Temporal coherence indicates how well an optical field can interfere with a delayed version of itself. Spatial coherence describes the correlation between different points of an optical field in space. In time-domain OCT, temporal coherence affects the axial resolution of an OCT image, while spatial coherence affects both lateral and axial resolutions. Light sources typically used in OCT systems are spatially coherent.

2.1.2 Low coherence interferometry

Interferometry is a powerful technique for measuring with very high sensitivity the magnitude and echo time delay of backscattered light from a sample. Back-scattered light from different depths of a sample interfere with the light that has traveled a known distance though a reference path result in an interference pattern [7].

As mentioned earlier, time-domain OCT systems are based on Low Coherence Interferometry (LCI). This technique relies on the coherence gating (a powerful means of examining light returned from a localized region of a sample) to estimate a precise axial position of an object in the direction of light propagation. Furthermore, by good focusing the light in a sample, a good transverse resolution can also be obtained. General configuration of a typical time-domain OCT system using a Michelson interferometer and fiber optics is shown in Figure 2.1.

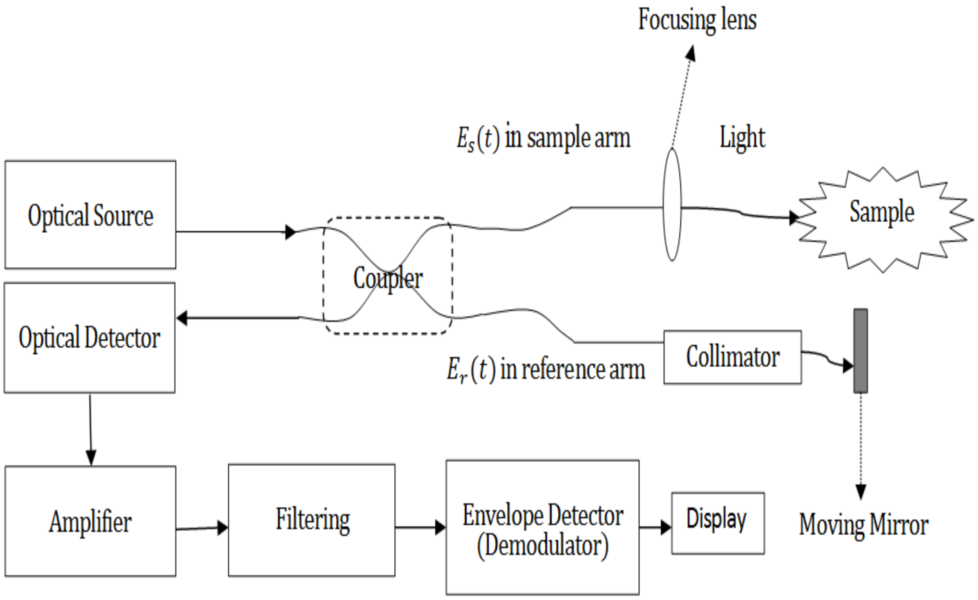

Figure 2.1: General configuration of a typical time-domain OCT system.

A 2x2 optical fiber coupler is used to implement a Michelson interferometer. In a time-domain OCT system, the incident light of optical source is split into a reference beam $E_r(t)$ and a sample beam, $E_s(t)$, that travel different distances in the two arms of the interferometer and through the fiber coupler. Then the back reflected light from different depths of the sample is combined with the reference beam reflected from a moving mirror. The back-reflected light from both sample and reference arms are directed by the fiber coupler towards an optical detector. Post processing such as amplification, filtering and demodulation are applied to the output of detected optical signal.

Optical detectors measure the intensity of the optical field rather than its amplitude or phase. The detected intensity in TD-OCT,$I_{detector}$ could be written as [12],

$$I_{detector} = \langle |E_{detector}|^2 \rangle = 0.5(I_r + I_s) + Re\{\langle E_r{}^*(t+\tau) E_s(\tau) \rangle\} = 0.5(I_r + I_s) + |G(\tau)| cos[2\pi \nu_0 \tau + \phi(\tau)], \tag{2.1}$$

where I_r and I_s are the mean (dc) intensities related to the reference and sample arms of the interferometer, τ is the optical time delay, $\nu_0 = c/\lambda_0$ is the central frequency of source and $G(\tau)$ is its complex temporal coherence function. Due to the low coherence of the source, optical interference is observed only when the optical path lengths of the back reflected beams from sample and reference mirror differ by less than the coherence length of optical source, defined as the width, e.g., full wave-half maximum, of $G(\tau)$.

Figure 2.2 shows a typical photocurrent signal that is generated with a time-domain OCT system, and recorded by a detector for a single reflector in the sample arm. This photocurrent signal is plotted as a function of the optical path difference in μm. This recorded signal is the result of several successive constructive and destructive interferences between $E_r(t)$ and $E_s(t)$ at the detector.

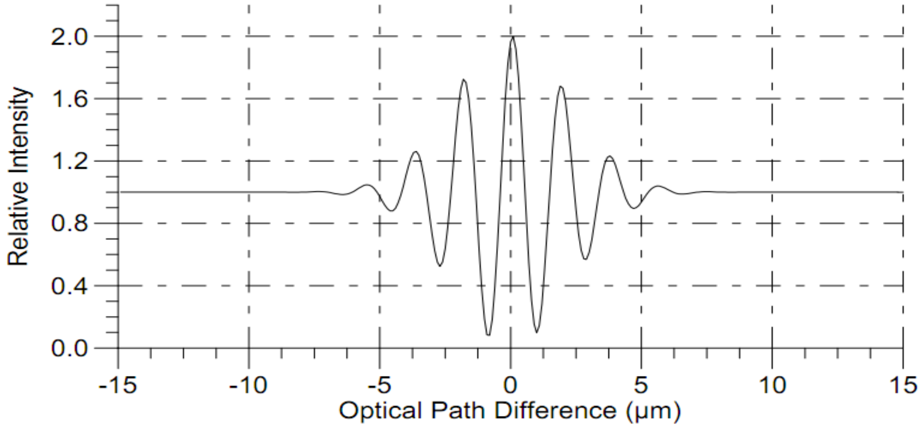

Figure 2.2: A typical signal recorded by the optical detector for a single reflector in the sample arm as a function of the optical path difference.

2.1.3 Scanning modes in OCT

In OCT different sample scanning modes are defined. The simplest form of imaging a sample is achieved through a single axial scan (depth-scan) of the sample which is called an A-scan. By moving the imaging light beam along one lateral direction of the sample, several A-scans are measured. The combination of these A-scans constitutes a cross-sectional image of the sample and is called a B-scan. Furthermore, by acquiring many of B-scans next to each other, we can construct a 3D image of a sample. An example of an A-scan and a B-scan are shown in Figure 2.3.

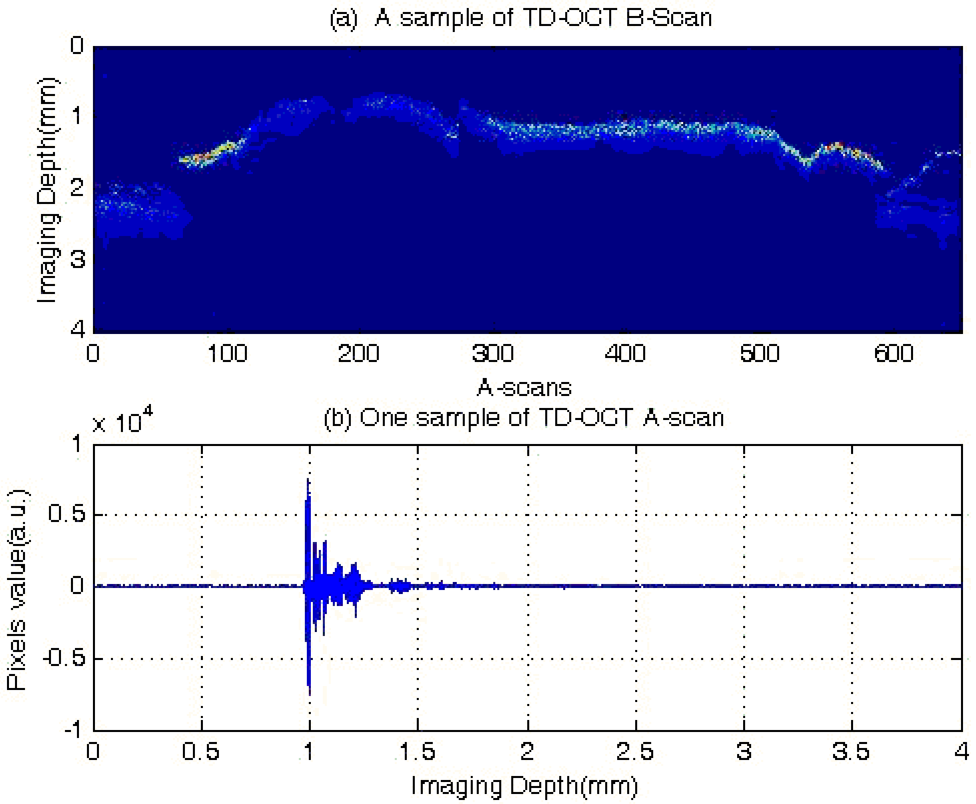

Figure 2.3: (a) An example of a TD-OCT B-scan, (b) an example of a TD-OCT A-scan.

2.2 Different types of OCT systems

OCT imaging systems are divided into two main categories: Time Domain OCT (TD-OCT) and Frequency Domain OCT (FD-OCT), where FD-OCT includes both Spectral Domain (SD) OCT and Swept Source (SS) OCT. In the following sections, the principle and function of such OCT systems are described in detail.

2.2.1 Time domain OCT

In this type of OCT system, the interferometer uses a broad band (low-coherence) light source with a short coherence length, e.g., several microns. The different interferometer configurations that have been used are explained in the following sections.

2.2.1.1 TD-OCT with direct optical detection

A typical TD-OCT configuration using direct optical detection is shown in Figure 2.4.

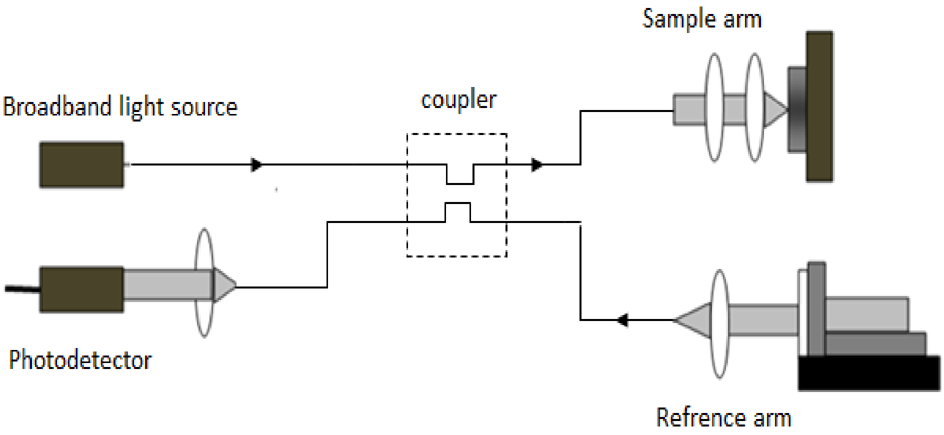

Figure 2.4: A typical TD-OCT setup with direct optical detection.

In this configuration the optical path lengths of the two interferometer arms are usually adjusted to be equal at the surface of the object. On increasing the length of the reference arm by scanning its mirror, the depth at which the object is imaged also increases. The mirror of the reference arm is typically scanned at the rate of a few kHz where a single scan results in a one-dimensional image of the object in depth, known as an A-scan. During an A-scan, the time delays that exist between the reflected field from the reference mirror and the field back scattered from different depths of the sample could be expressed by $\tau + f(t)$, where τ represents the time delay due to propagation inside the object, and $f(t)$ represents the delay due to the movement of the mirror. Thus the *instantaneous* optical power at the detector could be written as [2],

$$I_{OCT}(t) = |V_r[t - f(t)]|^2 + \left|\int_0^\infty V_s(t-\tau)R(\tau)d\tau\right|^2 +$$

$$2Re\left\{V_r[t - f(t)]\int_0^\infty V_s^*(t-\tau)R(\tau)d\tau\right\}, \quad (2.2)$$

where V_r and V_s are the analytic signals of the electric fields of reference and sample arms respectively, R is the axial reflectance of the object and * denotes the complex conjugation operator. The second RHS term of Eq. (2.2) is the sum of back reflected fields from all different depths of object (that is weighted by the reflectance of the object, R, at different depths). The third RHS term of Eq. (2.2) represents the interference term between the fields from the reference and sample arms. Since the absolute values of R for most objects of interest are much smaller than unity, the $\left|\int_0^\infty V_s(t-\tau)R(\tau)d\tau\right|^2$ term in Eq. (2.2) could be ignored in all practical cases. This method is called TD-OCT since the depth information is achieved by processing the acquired signal in the time domain. Finally, the optical detected signal is amplified, filtered by a band pass filter, rectified and low pass filtered in order to obtain the envelope of the acquired signal. A sample of a photocurrent signal detected in a TD-OCT system with a mirror as object is shown in Figure 2.5.

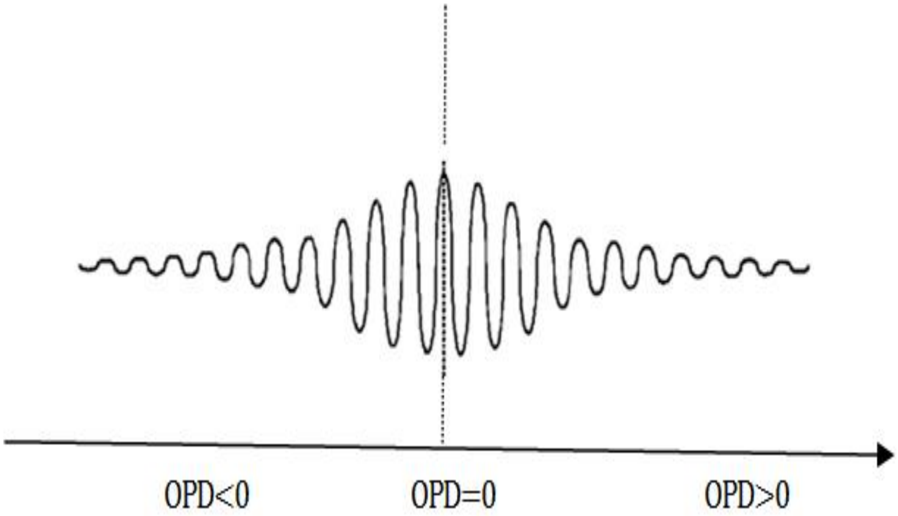

Figure 2.5: A sample of photocurrent signal acquired in TD-OCT system versus Optical Path Difference (OPD)

2.2.1.2 TD-OCT with differential optical detection

A typical TD-OCT system with differential optical detection setup is shown in Figure 2.6. This technique is used in order to reduce photon noise and optimize the sensitivity of the system and improve its SNR. The instantaneous optical power at each of the two optical detectors is according to the Eq. (2.2). The light is equally split into two beams and a phase shift of 180° is introduced between the two interfering optical fields. This is achieved by using two similar optical couplers that are shown in Figure 2.6, where each coupler introduces a phase shift of 90° between the field at one of its input ports and the field at the non corresponding output port. After propagating the light through the same optical distance, these beams are detected by using two identical but independent photo detectors. Finally the detected photocurrents at these detectors are subtracted to obtain the final A-scan.

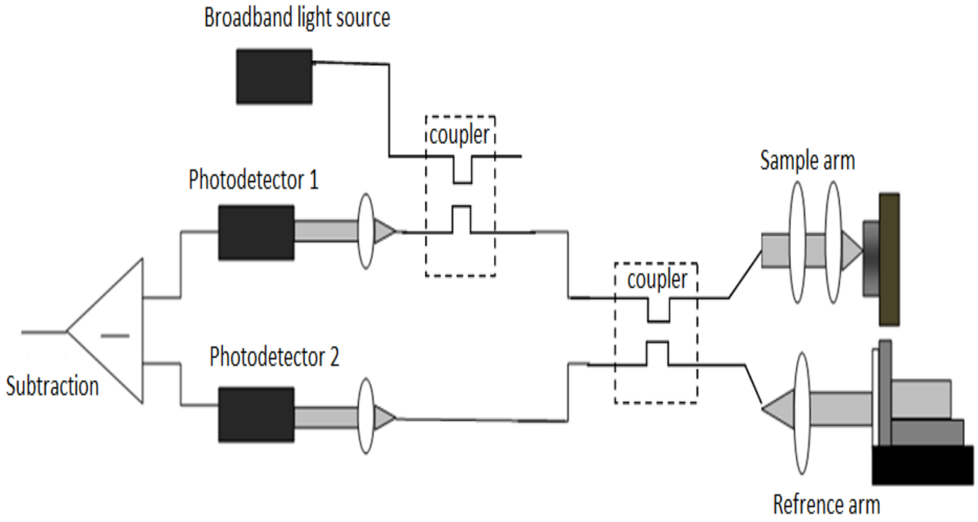

Figure 2.6: A typical TD-OCT configuration with differential optical detection setup.

In a previous study by Podoleanu *et al.* [8], it was shown that using a balanced differential light detection configuration has higher SNR in comparison with unbalanced and/or direct light detection configuration. When the two detectors are well matched, it reduces the photon noise. I, but in the case of mismatched photo-detectors (unbalanced) it could lead to an additional noise term.

2.2.2. Frequency domain OCT

In a TD OCT system, a mirror in the reference arm (a mechanical part moves during the acquisition of each A-scan. Thus the rate of scanning is limited by the movement of this mirror, so that it takes a relatively long time to scan larger samples. FD-OCT solves this problem by keeping the reference mirror fixed while the path lengths are matched within typically a few hundred microns. FD-OCT systems include two different configurations; SD-OCT and SS-OCT which are described in the following sections

2.2.2.1 Spectral domain OCT

In SD-OCT, the photo-detector is replaced by an optical spectrometer. The spectrometer consists of several light collecting optical elements and a CCD camera. Similar to TD-OCT, a broad band light source is utilized as a source. A typical configuration of an SD-OCT system is shown in Figure 2.7.

In SD-OCT, each A-scan is achieved by detecting the spectrum of the sum of backscattered light from the object and the light reflected from the reference mirror by the CCD. This recombined signal, after passing through the Diffraction Grating (DG), disperses into its different wavelengths. Ultimately, object's depth structure is obtained by the Fourier transform of spectrometer output [9] .

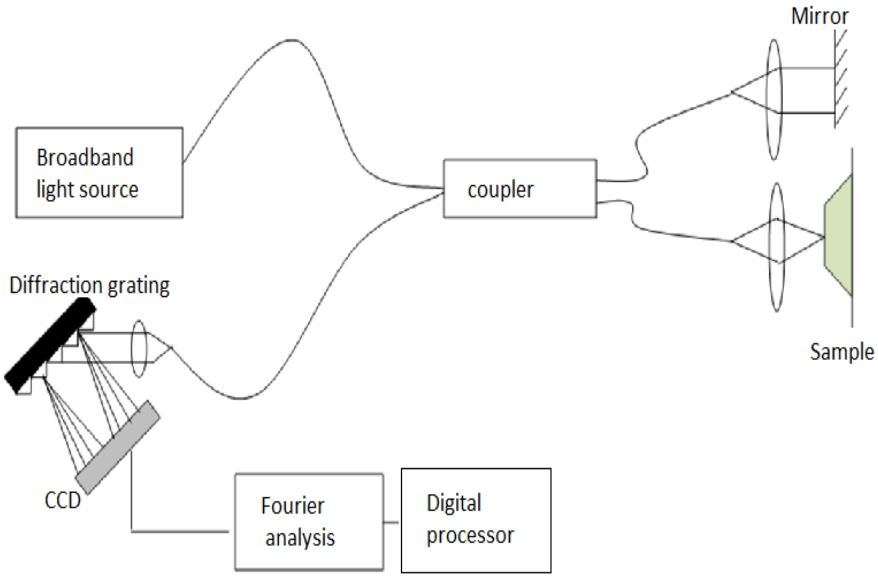

Figure 2.7: A typical configuration of a SD-OCT system.

In SD-OCT, we can have simultaneous depth imaging without the need to change the reference path. The main advantages of this method are that it dramatically increases the imaging rate compared to TD-OCT (> 20 times faster), provides higher SNR, and performs the imaging with more sensitivity than conventional TD-OCT [10]. In SD-OCT system the total interference signal $I(k)$ is denoted by [11],

$$I(k) = G(k)(1 + \int_{-\infty}^{\infty} A(z) e^{-i2knz} dz + \frac{1}{4}\int_{-\infty}^{\infty} AC[A(z')]\, e^{i2kn(z)z} dz)$$

$$A(z) = \tfrac{1}{2}\, a(z) + \tfrac{1}{2}\, a(-z), \qquad (2.3)$$

where $I(k)$ includes: a DC term of $G(k)$, depth information of the object (second term) and the mutual interference of all elementary waves (third term) while the back reflection intensity is found in $A(z)$. We note that $k = 2\pi/\lambda$ is the wave number, $G(k)$ is the spectral density distribution of the light source, $a(z)$ is the back scattering coefficient of the sample signal, which is symmetric with respect to $z = 0$, and n is the refractive index. It should be mentioned that in SD-OCT, the axial resolution depends on the combination of light source bandwidth, spectrometer bandwidth and also on the number of pixels in the CCD [12].

2.2.2.2 Swept source OCT

Another type of FD-OCT systems is the swept-source OCT (SS-OCT). In this setup, a wavelength swept laser source and a photo-detector are employed as a source and detector respectively, whereas in TD-OCT and SD-OCT a broad band light source is utilized. Similar to the previous OCT configurations, the light beam is divided by a beam splitter and then a fraction of light is delivered to the object and the rest is guided to the reference arm. Ultimately, the signals from both arms of the interferometer interfere at the photo-detector. The spectral components of $I_{detector}(k)$ are captured by recording the signal using a photo-detector while synchronously sweeping the wave number of a narrowband swept laser source. The axial reflectivity profile is achieved by computing the Fourier transform of the sequentially acquired signal. A typical configuration of an SS-OCT system is shown in Figure 2.8.

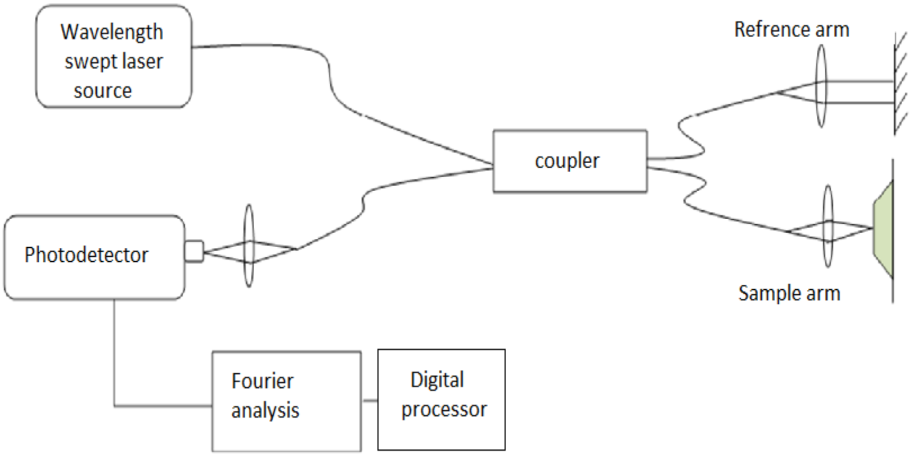

Figure 2.8: A typical configuration for an SS-OCT system.

In SS-OCT, the photocurrent $I_{detector}(t)$ at detector can be denoted as [13],

$$I_{detector}(t) =$$

$$\frac{\eta q}{hv}\left(P_R + P_S \int r^2(z)dz + 2\sqrt{P_R P_S}\int r(z)\Gamma(z)cos(2k(t)z + \phi(z))dz\right), \qquad (2.4)$$

where η is the detector sensitivity, q is the quantum of electric charge, hv is the single photon energy, P_R is the optical power reflected from the reference arm at the photo-detector, P_S is the optical power illuminating the sample and z is the axial coordinate where $z = 0$ corresponds to zero optical path length difference. Here, $r(z)$ and $\phi(z)$ are the amplitude and phase of backscattered profile of the object respectively,

$\Gamma(z)$ is the coherence function of the instantaneous laser output, and $k(t) = 2\pi/\lambda(t)$ is the wave number which changes over the time by tuning of the laser. The third term represents the interferometric signal, and the first and second terms contribute to the non-interference background. As a result, the axial A-scan is constructed by performing the Discrete Fourier Transform (DFT) of $I_{detector}(t)$ [13]. In practice, the detector output is digitized and sampled into a finite number of data points.

2.3 Resolution in OCT imaging

One very important parameter in all types of OCT systems is resolution. There are two different types of resolution in OCT systems: axial resolution and lateral or transverse resolution. One of the advantages of low-coherence source based OCT is that axial and lateral resolutions are independent of each other. Axial resolution in time-domain and spectral-domain OCT systems is a function of the coherence length of the light source. In these OCT systems, sources with a Gaussian spectrum are usually used. Therefore the axial resolution for a time-domain OCT system with a source having a Gaussian spectrum is given by [2],

$$\Delta z = \frac{2ln2}{\pi}\left(\frac{{\lambda_0}^2}{\mathrm{n}\Delta\lambda}\right), \qquad (2.5)$$

where $\Delta\lambda$ is line width of the light source, λ_0 is its central wavelength and n denotes the refractive index of the object. As Eq. (2.5) shows, the axial resolution of the time-domain OCT image is inversely proportional to the bandwidth of the light source; thus optical sources with a broad line width are needed to achieve higher axial resolution. In FD-

OCT, the axial resolution depends on several parameters such as the bandwidth of light source, the bandwidth of the spectrometer and also the number of CCD pixels [14].

The transverse resolution in an OCT system is dependent on the properties of the optical elements in the sample arm, e.g., numerical aperture, in addition to the wavelength of the used light [6].The transverse resolution of OCT system can be written as [15],

$$\Delta x = \frac{4\lambda}{\pi}\left(\frac{f}{d}\right), \tag{2.6}$$

where d is the spot size of imaging lens, and f denotes its focal length. Higher transverse resolution can be obtained by using a lens with a high numerical aperture that would focus the imaging beam to a smaller spot size. In the case of a Gaussian beam incident on the object, the transverse resolution is also related to the depth of focus or the beam's confocal parameter, b, which is two times of Rayleigh range z_R as denoted by [15],

$$b = 2z_R = \pi \Delta x^2/\lambda. \tag{2.7}$$

Thus, increasing the transverse resolution would result in a decrease in the depth of focus, similar to conventional microscopy [6]. In any OCT system there are also several other factors beyond the ones mentioned above that could further limit its resolution. These factors include light dispersion, light multiple-scattering and light absorption and refraction. All these factors could have negative effects on OCT measurements and resolution of OCT systems. Effects such as absorption and scattering reduce the optical power collected during imaging, while dispersion and refraction alter the OCT signal without power loss [16].

Chapter 3

Image Processing in OCT

Application of OCT imaging technology in medical and biological studies has been growing fast. One of the main goals of any kind of medical imaging system is to provide high-resolution images with higher depth of imaging. Higher imaging depth helps a physician, to have better visualization from the internal structures of tissue and to better distinguish any abnormalities in-depth. One of the important issues that limit the imaging depth in OCT systems is the existence of noise and image artifacts. Similar to the other imaging systems, the performance of OCT systems could be improved using both hardware and software.

In the context of hardware improvement, there have been lots of efforts in designing new OCT systems with optimizing the light source, designing new detectors and also improving mechanical and electrical modules of OCT systems. In the software aspect, most work has been concentrated on applying advanced image processing methods to the OCT image. Having higher depth of imaging is one important issue that can be increased by applying some image or signal processing methods on the OCT image. Different OCT techniques are developed to increase the rate of OCT scanning, enhance the depth of imaging and also increase the axial and lateral resolutions of the acquired OCT image.

To obtain better OCT images, software development of OCT systems can be more economic and easier in comparison to changing of an OCT setup that is usually expensive, time consuming and difficult.

In the past decades, there has been an increasing interest in applying different image and signal processing methods to enhance OCT images. These techniques were mainly deconvolution algorithms, speckle noise reduction methods, dispersion compensation and distortion removal. In this Chapter, different sources of noise and image artifacts in OCT system are discussed. Then, some of the main image processing methods that have been applied on the OCT images are reviewed.

3.1 Source of noise in TD-OCT

Noise is an undesirable effect that exists in all types of OCT imaging to lower the quality of the obtained OCT image. It also can limit the depth of OCT imaging. Two main types of noise in the OCT systems are: system noise (from optical and electrical modules in OCT systems) and also speckle noise. In the following sections, these types of noise and their origin in OCT systems are explained.

3.1.1 TD-OCT system noise

Different electrical and optical modules of OCT systems can generate noise in an OCT image. The most important noise sources in an OCT system are given by [15]:

- Optical source noise
- Thermal noise

- Electronic noise
- CCD pixel noise

Two major types of noise in OCT systems that are related to the optical source are photon shot noise and photon excess noise [11]. The photon shot noise is related to the quantum nature of light radiation. This kind of noise is related to the fact that photons arrives randomly to the surface of detector and this flux of photons reaching to the detector during an interval T produces random electric current given by [15],

$$I = \frac{e}{T} n, \tag{3.1}$$

where, e represents the electron charge and n is the number of generated photo-electrons. The value of shot noise has a direct dependency on the number of photo-electrons n and also the bandwidth of the electronic circuit. The contribution of photocurrent due to the shot noise to the total photocurrent of OCT system is denoted by [15],

$$< \Delta i_{SN}^2 >= 2e < i > B, \tag{3.2}$$

where, $< \Delta i_{SN}^2 >$ is the average of shot noise photocurrent fluctuations, e is the electron charge, B is the bandwidth of the electronic circuit and i is the total photocurrent in OCT system.

Excess photon noise is due to the self-interference of a broad spectrum optical source. It can be shown that the contribution of the excess photon noise to the total OCT photocurrent is expressed by [9],

$$< \Delta i_{EPN}^2 >= (1 + \Pi^2) \frac{B}{\Delta \upsilon_{eff}} < i >^2, \tag{3.3}$$

where Π is a factor related to the polarization state of the optical radiation and $\Delta\upsilon_{eff}$ is the effective bandwidth of the incoherent light source.

Thermal noise is produced by random motion of electrons at finite temperatures and inside resistive materials [17]. These movements produce a certain electric current even in the absence of optical radiation at the detector. The contribution of thermal noise to the photocurrent is expressed in terms of the variance of thermal photocurrent as denoted by [15],

$$< \Delta i_{th}^{2} >= \frac{4K_B T}{R_L} B, \tag{3.4}$$

where, K_B is the Boltzmann's constant, B is the bandwidth of the detector and R_L is the equivalent load resistance at temperature of *T*. Another source of noise is related to the existence of electrical circuits in the OCT system. These electrical circuits can cause several sources of noise such as $1/f$ noise, thermal noise, dark current, pre-amplifier noise and also analog-to-digital conversion (quantization) noise [9]. Another source of noise comes from the detector of OCT system. Photo-diodes and CCDs could also produce additional noise [11].

In general, the effect of all noise sources above can be considered as an additive photocurrent term in the final photocurrent i, as denoted by,

$$i = i_{sig} + i_{Noise} \ , \tag{3.5}$$

where, i is the total measured OCT photocurrent, i_{sig} is the true signal photocurrent and i_{Noise} is that part of photocurrent that is due to the noise in the OCT system.

3.1.2 Speckle noise in OCT images

Speckle noise had much attention in the image processing stage of all types of coherent imaging systems such as radar, synthetic aperture radar , radio astronomy, ultrasound, in addition to OCT [18], [19], [20]. Speckle noise is the result of cross-interference that happens between the random phases of back scattered optical fields from different depths of object. This is much more common in highly scattering objects.

In OCT systems, speckle arises as a natural consequence of the limited spatial bandwidth of the interference measured signals [21].In highly scattering samples, speckle has a dual role, first as a source of noise and second as a carrier of information from the object. The effect of speckle noise is in reducing the contrast of OCT image and in giving a grainy and granular appearance to the acquired image. Speckle noise can complicate the post-processing stage of OCT images such as segmentation, feature extraction and edge or boundary detection [22], [23], [24], [25], [26]. In an OCT image, speckle noise can be considered as a multiplicative factor, denoted by [27],

$$f(x, y) = [s(x, y) \times n_{Speckle}(x, y)] + n_{Additive}(x, y), \quad (3.6)$$

where, $s(x, y)$ represents the noise free OCT image, $n_{Speckle}(x, y)$ is the multiplicative speckle noise and $n_{Additive}(x, y)$ represents OCT system noise. The amount of OCT system noise is often less than the amount of speckle noise in OCT systems. Hence, in most noise reduction methods that are applied to OCT images this term is sometimes ignored. Although the effect of OCT system noise is less than speckle noise, still it can reduce the amount of SNR in the OCT image and can have a negative effect on the depth of OCT imaging.

3.2 Source of artifacts in OCT images

In addition to the OCT system noise and speckle noise, another source of image degradation in the OCT system is the existence of artifacts. The presence of artifacts in the OCT image usually causes difficulties in the analysis of images and reduces the sensitivity and accuracy of the results. It can also cause to misrepresentation of the object morphologies and complicates the interpretation of images.

To date, several types of instrument and sample induced artifacts are reported for OCT images. Instrument induced artifacts are included mirror artifact [28], [29], optical aberrations (or fan distortions) [30], [31], [32] and autocorrelation [33], [34], [35][36], [37]. On the other hand, sample-induced artifacts can have different types, e.g., birefringence artifact [38], [39], shadowing, refraction [40], [41], motion of sample [32], [42], [43], [44],[45] and distortion [46], [47]. Intensity distortion is the prominent type of sample-induced artifact in an OCT system [48], [49]. The main reason of intensity distortion in the OCT system is the dependency of optical path length on the refractive index of the sample. As different values of air and tissue have an effect on the optical path length, thus the shape and thickness of the sample can affect the real intensity of image pixels in the OCT image. These artifacts are present particularly when the system is used in noncontact mode, i.e. when an air-gap exists between the object and the focusing optics of the OCT scanner [47]. Another important type of distortion that frequently occurs in OCT is due to the optical dispersion. Dispersion occurs when the group velocity of an optical pulse is not constant inside the imaged sample such that its low frequencies travel faster than high frequencies. Dispersion causes blurring in an axial A-scan and consequently a reduction of axial resolution in OCT systems [16].

3.3 Image processing in OCT

In the two previous sections of this Chapter, different sources of noise that exist in the OCT imaging systems were discussed. In addition, different kinds of artifacts that are present could destroy the quality of OCT images were explained. The main goal of most image processing methods that are applied on OCT images is to reduce the degrading effects of different noise source and image artifacts on the OCT imaging. These processing methods are mainly categorized in the following groups:

- Deconvolution algorithms
- Speckle noise reduction methods
- Dispersion compensation
- Distortion removal in OCT images

In the following section, the image processing research that is done in each of these categories will be explained.

3.3.1 Deconvolution methods in OCT

In practice, a typical imaging system can be considered as a Linear Shift Invariant (LSI) system with an impulse response function $\boldsymbol{h}$ which determines the relation between the input and output of system. Therefore the interaction of an OCT imaging system with tissue can be considered as an LSI system. In an OCT system the intensity of the interferometric photocurrent signal, i, is proportional to the correlation of the back-reflected electric optical fields from the reference arm, $E_r(z)$, and sample arm, $E_s(z)$, and is denoted by [50],

$$i(\tau) \propto Re\{< E_r^*(z+\tau)E_s(z) >\}, \tag{3.7}$$

where, τ, denotes time delay, * indicates complex conjugate operator, and $<\cdot>$ denotes time average. In addition, the field returning from the sample arm, $E_s(z)$, could be considered the convolution of the incident field on the sample, $E_r(z)$, and the impulse response function of the sample, $h(z)$, [50]

$$E_s(z) = E_r(z) \otimes h(z). \tag{3.8}$$

The impulse response function of a sample $h(z)$, can be interpreted as the reflectivity pattern of imaged tissue that is dependent on the refractive index of tissue. The axial coordinate is determined by $z = ct$, where c is the speed of light in the sample. Therefore the interferometric signal, $i(\tau)$, of Eq. (3.7) is proportional to the $E_r(z)$ and $h(z)$ denoted by [50],

$$\begin{gathered} i(\tau) \propto Re\{< E_r^*(z+\tau)[E_r(z) \otimes h(z)] >\} \\ i(\tau) \propto Re\{\Gamma(\tau) \otimes h(\tau)\}, \end{gathered} \tag{3.9}$$

where $\Gamma(\tau) = < E_r^*(z+\tau)E_r(z) >$, is the coherence function of the light source, that is the inverse Fourier transform of the power spectral density $S(\lambda)$. In a TD-OCT system, interferometeric distortions (blurring) occurs due to the convolution of Eq. (3.9). In addition, considering the optics of an OCT system and neglecting the effect of the sample Eq. (3.9), the Point Spread Function (PSF) of a TD- OCT system in both axial and transversal directions causes blurring in the OCT image. This is due to the convolution between the PSF of OCT-system, $\Gamma(t,a,u)$, and the object being imaged, $h(t,a,u)$. Hence image processing methods are needed to reduce the blurring effects in the OCT image. Many different deconvolution methods are proposed to solve this problem. If $g(t,a,u)$ was the convolution result of, $h(t,a,u)$, and the PSF, $\Gamma(t,a,u)$, given by [51],

$$g(t,a,u) = h(t,a,u) \otimes \Gamma(t,a,u), \tag{3.10}$$

then, the deconvolution can be simply done in the Fourier domain by using [52],

$$H(m,v,z) = \frac{G(m,v,z)}{S(m,v,z)}, \tag{3.11}$$

where, $H(m,v,z), G(m,v,z)$ and $S(m,v,z)$ represent the Fourier transform of $h(t,a,u), g(t,a,u)$, and $\Gamma(t,a,u)$ respectively. Generally, the aim of any deconvolution method is to extract the original image (de-blurred image), $h(t,a,u)$, from the measured (degraded image), $g(t,a,u)$. The simplest deconvolution method for image restoration is simple inverse filtering (Eq.3.11). However in the inverse filtering method, the effect of noise is not considered and the result of this deconvolution algorithm is extremely sensitive to noise [53]. Therefore, this algorithm is rarely used in practice. A variety of improved deconvolution algorithms were applied for the deconvolution of OCT images [54]. Depending on the availability of information about the degradation effect, deconvolution methods are classified into two approaches. If the degradation process is known, i.e., an estimate of the PSF $\Gamma(t, a, u)$ is available, then the extraction of $h(t, a, u)$ from $g(t, a, u)$ is called by regular deconvolution [55], [56]. On the other hand, if no information is available about the PSF function, the deconvolution is recognized as blind deconvolution [57], [58]. Most deconvolution algorithms are performed iteratively [59]. Some of these iterative methods include maximum likelihood estimation, maximum a posteriori estimation and expectation-maximization algorithm [59], [60]. In blind deconvolution methods, a good primary estimate of the PSF is helpful for quicker convergence. In OCT image processing, different deconvolution algorithms of both types, regular and blind deconvolution, were proposed. In addition, different studies were pursued to reduce the blurring effect of the convolution in both axial or transversal directions and even in both directions [50], [59].

Axial deconvolution algorithms were applied in [54], [50]. In these studies, the blurring induced by the incident electric field, convolved with the impulse response of an object, is considered to apply the deconvolution algorithm. The primary deconvolution techniques in these studies are: iterative restoration algorithm and minimum least squares error approximation. In a study by Hsu *et al.* [61], he applied an iterative axial deconvolution method to find the actual structure of the imaged sample. The result of this technique was demonstrated by using numerical simulations and also actual OCT images. In another study by Bousi *et al.* [62], he applied a deconvolution method on the Fourier domain OCT (FD-OCT) signals. The results of his study showed an axial resolution improvement of about seven times. In another work by Wang *et al.* [53], he proposed a deconvolution method for the image enhancement of spectral-domain OCT

(SD-OCT). Their method included Wiener filtering for the aim of spectral deconvolution and successive homomorphic filtering for spatial deconvolution, aiming to minimize the blurring effect of the axial PSF. The results of their study, before and after the deconvolution process, were compared and it was demonstrated that their proposed method could increase both Contrast-to-Noise Ratio (CNR) and average SNR in the reconstructed OCT image.

In a study by Ralston *et al.* [59], a deconvolution algorithm was investigated by using the Gaussian beam deconvolution for reducing the effect of transverse blurring in an OCT image. In this study, both regularized and Richardson–Lucy algorithms were tested on simulated data and the results and the limitations of each method were compared and discussed. In another study by Yasuno *et al.* [63], he applied a lateral deconvolution method to cancel the effect of lateral defocusing in Fourier-domain OCT (FD-OCT) images. In this study, some approximations were introduced in order to design a deconvolution filter and the improvement of lateral resolution was estimated.

Liu *et al.* [51] applied a kernel (two-dimensional matrix) to simultaneously de-convolve the PSFs of both axial and transversal directions. In this study, the deconvolution algorithms were performed by using both Wiener and Lucy-Richardson algorithms. The results of this study showed that this deconvolution method could enhance image sharpness in both axial and transversal directions. The results of another study by Schmitt [64] showed that a modified version of the non-linear CLEAN deconvolution algorithm can effectively improve the resolution of OCT images in both lateral and axial directions. In another study by Woolliams *et al.* [65], he used a phantom for measuring the spatial PSF of an OCT system and subsequently used this spatial PSF to perform the spatial deconvolution. In this study, the lateral resolution improved by 3.1 μm compared to an axial resolution enhancement of 4.5μm. In another study by Liu *et al*. [66], he applied an automatic PSF estimation method to de-blur the out-of-focus OCT images. In his study, the Richardson-Lucy deconvolution was applied to de-convolve the noisy and defocused OCT images by using a set of Gaussian PSF with different beam spot sizes.

3.3.2 Speckle noise reduction methods

As it was explained in Section 3.1.2 of this Chapter, speckle noise is one of the most challenging issues and limiting factors that affect the quality of OCT images and it exists in all types of OCT systems. Since the invention of OCT imaging systems, different studies were performed on this subject and several methods were proposed to reduce the effect of speckle on OCT images. A limited number of studies tried to reduce speckle noise in OCT signals before the formation of OCT image while many other methods were applied after the formation of OCT image and are commonly referred to as image post-processing methods [21]. Among these methods, the most popular one are median filtering, Wiener filtering, multi-resolution wavelet analysis and adaptive smoothing. In a study by Pal *et al*. [67] the results of applying several speckle reduction methods on the OCT image were evaluated and compared. These methods were based on the local statistics, median filtering, geometric filtering and also transformed domain homomorphic filtering. In another study by Schmitt *et al*. [68], he studied the origin and statistical properties of speckle in the OCT image and also classified them in different categories for the OCT systems. In addition, in his study, the two concepts of signal-carrying and signal-degrading of speckle were discussed. In another study by Bashansky *et al*. [69], he studied the statistical properties of speckle noise by using a set of OCT measurements and proposed a simple and practical speckle reduction technique to reduce its effect. In another work by Rogowska *et al*. [70], he applied a locally adaptive rotating kernel transformation for the speckle reduction and enhancement of OCT images. In another study by Adler *et al*. [71], he applied a spatially adaptive wavelet filter that was designed in two dimensions to reduce the speckle noise in both TD-OCT and FD-OCT images. His method could separate the edge of an OCT image from the discontinuities that are due to noise. Furthermore, the power of noise was reduced in the wavelet domain and the value of SNR was improved. In a work by Marks *et al*. [72], he applied a regularization method by minimizing I-divergence measure to reduce the speckle effects on the OCT image. In another work, Ozcan *et al*. [22] applied various digital filters to reduce the effect of speckle on the OCT image and also compared their performance. In another study by Puvanathasan *et al*. [73], he proposed a novel speckle reduction technique based on the soft thresholding of wavelet coefficients. His technique showed a superior performance, in terms of image metrics improvement, and in comparison with the adaptive Wiener and adaptive Lee filters. In a study by Wong *et al*. [27], he proposed a novel method based on the log-space general Bayesian estimation for the speckle reduction of OCT images. His method increased the contrast of OCT images and also minimized the presence of artifacts. In addition, the results of his technique had the best performance regardless to the type of features that existed in different layers of an OCT image. This method was also insensitive to irregularly shaped structures that could be observed in the original OCT image.

3.3.3 Dispersion compensation in OCT

The most two important impacts of dispersion on OCT images are the degradation of depth resolution and also reduction in sensitivity. Other effects of dispersion on OCT imaging such as phase shift and change of the mean wavelength are less prominent. Depth resolution of OCT system is usually defined by the Full Width at Half Maximum (FWHM) of an interferogram or the coherence length of the light source. Dispersion adds an additional phase term to the Fourier components of an OCT interferogram, hence it increases its FWHM which consequently reduces the depth resolution in the OCT system. In an interferometer system, the phase of backscattered light that come back from the sample is affected by the dispersion of light in the sample. According to the Fourier shift theorem, an additional phase in the Fourier space is equivalent to a shift in the spatial domain. Therefore, this additional phase due to the dispersion of light in the sample leads to distortion in the OCT image.

In some studies, hardware techniques are used for the compensation of resolution loss due to dispersion [74]. These techniques try to balance dispersion in both sample and reference arms of the interferometer [75]. This compensation is typically done by applying a dispersive material, corresponding to the sample dispersion at the reference arm of the interferometer. Such an arrangement can be matched to different values and orders of sample dispersion [2]. One of the challenges in hardware techniques to compensate for dispersion is the implementation of a dynamic compensation of depth-dependent sample dispersion [75].

Digital dispersion compensation methods can be applied in both time domain and Fourier domain [77]. Numerical methods of dispersion compensation can remove different levels of dispersion in an OCT image through a dynamic process. In a study by Brinkmeyer *et al*. [76], dispersion compensation is performed in the Fourier domain by using a wave-number scale transformation. In another study by Kohlhaas *et al*. [77], a numerical algorithm is applied to dispersion-corrupted data obtained by coherence domain measurements. This algorithm can result in a retrieval of micron-order resolution and in an enhanced dynamic range of OCT measurements. In a work by Boer *et al.* [78], a quadratic phase shift method was applied to eliminate the broadening effect of the group-velocity dispersion on the coherence function of an interferometric signal and in the Fourier domain OCT. In another study by Fercher *et al.* [79], a digital dispersion compensation technique was proposed for TD-OCT, based on the numerical correlation of the depth scan with a depth variant kernel. In another work by Marks *et al*. [16], an autofocus algorithm is proposed for estimating the value of material dispersion in OCT images. This algorithm minimizes the entropy, a contrast-enhancement criterion, of corrected axial depth-scans. In work by Wojtkowski *et al*. [80], a numerical dispersion compensation method was proposed to correct the phase as a function of frequency in FD-OCT. In another study by Banaszek *et al.* [58] a blind numerical method was applied to reduce dispersion effect on the OCT image. This algorithm does not require a priori knowledge about the dispersive properties of the sample. In his work, the dispersion compensation is accomplished by processing the phase information of the interferograms to calculate a generalized auto-convolution function. In a recent study by Lippk *et al.* [81], a numerical dispersion compensation method based on the fractional Fourier transform was proposed for SD-OCT.

3.3.4 Distortion removal of OCT image

Several studies were performed to evaluate different instrumental and sample related artifacts in an OCT image. Furthermore, different processing methods were proposed to reduce the degrading effects of artifacts on the OCT image. In this subsection, some of these methods are briefly reviewed.

In a study by Oh *et al*. [28], a new computational algorithm was proposed that tried to eliminate the degrading effects of sample motion on an SD-OCT image. The results of applying this algorithm on the both simulation and experimental data show that it can also remove the effect of mirror artifact that is caused by random phase fluctuation in spectrally resolved interferograms. In a work by Ho *et al*. [29], a clinical assessment was pursued to investigate the effect of mirror artifact on SD-OCT images. In another study by Ortiz *et al*. [30], a numerical algorithm was developed based on a 3-D ray propagation model with the aim of fan distortion correction in the TD-OCT images. In a study by Ozcan *et al*. [36] , a new processing technique based on a minimum-phase function proved efficient in removing the autocorrelation artifact in FD-OCT images. This method demonstrated an ability to increase the depth of imaging in OCT. In another study by

Sekhar *et al*. [37], a logarithmic transformation was applied to recover the FD-OCT signal which resulted in less autocorrelation artifact in the reconstructed signal. In a study by Zawadzki *et al*. [42], a registration technique based on a cross correlation method was proposed to compensate for motion artifact due to eye and head motion in an OCT image. Also, in the same study a correction method was proposed for reducing distortion due to the geometry of scanning optics. This was performed by incorporating the geometry of the scanning beam into the volume rendering software. In another study by Westphal *et al*. [32], several numerical algorithms were applied to correct three primary unavoidable distortions in an OCT system: nonlinear axial scanning, diverging or converging of lateral scanning and also refraction at smooth boundaries. The first two algorithms were applied in real-time, i.e., prior to the display of an image and the third algorithm was performed as a digital post-processing step.

Chapter 4

Statistical Modeling of Depth-Scan Photocurrent in TD-OCT System

One of the major issues that exist in all types of the OCT system is the existence of noise that can limit the depth of OCT imaging. Noise obscures the small features of an imaged object and makes it more difficult to determine the fine details of imaged object especially at the higher depths of imaging. In medical applications, this could result in misdiagnosis of different diseases. Hence, noise reduction is an important goal in the post-processing stage of all types of OCT systems. Having an accurate understanding of the noise statistics in OCT data can be very useful. In this sense, knowing the statistical properties of noise can be useful to choose optimum post-processing algorithms to reduce the effects of noise on the OCT image.

Different image processing methods were proposed to improve the resolution of OCT images and also to reduce the effect of noise on the OCT image. To the best of our knowledge, most of these methods were deterministic. Using statistical concepts in OCT image processing were mainly limited to the calculation of average SNR in the different OCT configurations [82]-[83], [8] and also to studying the statistics of speckle in OCT images [69] . In a recent study [5], a depth-scan photocurrent in TD-OCT system, using polarized thermal light source, was modeled as a Gaussian random process that is completely determined by its second order statistics (mean and autocorrelation function). This statistical knowledge can be used to design different statistical image processing methods to improve the quality of OCT images. In this Chapter, the statistical model of [5] is reviewed and the dependency of noise statistics on the OCT signal is theoretically demonstrated in a TD-OCT system with the direct or differential light detection.

4.1 Statistical model of depth scan photocurrent in TD-OCT

In Chapter 3, different sources of noise and artifacts in an OCT system are discussed. In addition, the OCT system noise is considered as an additive photocurrent noise, i_{Noise}, that affects the original OCT photocurrent, i_{Sig}, according to the relation of,

$$i = i_{Sig} + i_{Noise}. \tag{4.1}$$

Although OCT system noise plays a considerable role in the degradation of an OCT image, most studies neglect its effect on the OCT image, and focus on speckle reduction instead.

The most typical optical sources in OCT systems are polarized Super-Luminescent Diodes (SLD) which are polarized thermal sources[84]. The derivation of the statistics of OCT photocurrent, presented in this Chapter, is valid for OCT systems with such optical sources. The asymptotic-Joint-Probability-Distribution Function (JPDF) of photocurrent due to a polarized thermal light source, and similarly due to an SLD, could be considered a Gaussian random process [86]. This Gaussian random process is completely determined by its second order statistics (mean and auto-correlation function).

Furthermore, in a TD-OCT system, due to its high value of SNR (typically >80 dB), the JPDF of a depth-scan photocurrent can be approximated by a Gaussian random process.

In the following sections, the second order statistics of a TD-OCT depth-scan photocurrent, derived in [5], and in for both direct and differential light detection schemes is presented in detail.

4.2 TD-OCT with direct optical detection

The function of an optical detector is to convert the optical intensity to photocurrent at its output. In a TD-OCT system, with the assumption that optical detector area is smaller than the coherence area of incident optical intensity $I(t)$ on the detector, the detector can be considered a linear time invariant system, shown in Figure 4.1. We should emphasize that the time t considered to calculate the average intensity $I(t)$ should be longer than the optical period of light source and less than the time of interest.

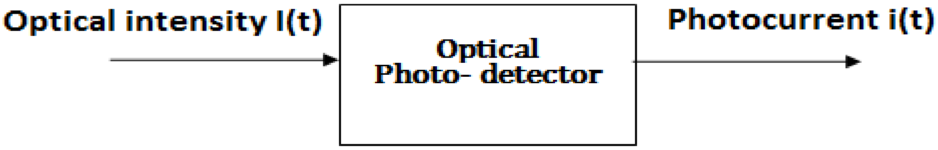

Figure 4.1: Input-output model of an optical photo-detector.

For the linear system of Figure 4.1, the output of the photo-detector, i.e., the OCT photocurrent $i(t)$, is given by [85],

$$i(t) = \int_{-\infty}^{\infty} h_{det}(t-t')dN(t'), \tag{4.2}$$

where $h_{det}(t)$ is the real-valued impulse response function of the detector and $N(t)$ is a Poisson random process that represents the generation of photoelectron and is denoted by [85],

$$N(t) = \int_{-\infty}^{\infty} dN(t') \,, \tag{4.3}$$

and $dN(t')$ is given by,

$$dN(t') = \rho I(t), \tag{4.4}$$

where ρ is a constant of quantum mechanical nature and for the quasi monochromatic light it can be approximated by [85],

$$\rho \cong \eta / h\bar{\nu}, \tag{4.5}$$

where η is the probability of release one photoelectron due to an incident photon, h is the Plank's constant and $\bar{\nu}$ is the central optical frequency. Using Eq. (4.3), we have the following relations of,

$$E[dN(t)] = \rho E[I(t)]dt$$

$$E[dN(t_1)dN(t_2)] = \{ \rho^2 \Gamma_{I_{OCT}}(t_1, t_2) + \rho E[I(t_1)]\delta(t_2 - t_1)\} \, dt_1 dt_2 \,, \tag{4.6}$$

where, $\Gamma_{I_{OCT}}(t_1, t_2)$ denotes the autocorrelation function of incident photocurrent intensity at the detector and is given by [86],

$$\Gamma_{I_{OCT}}(t_1, t_2) = E[I(t_1)I(t_2)]. \tag{4.7}$$

From the properties of a Poisson random process the probability of two simultaneous occurrences is zero, implying that the simultaneous generation of two photoelectrons is not possible. Therefore when $t_1 = t_2$, the second term of

Eq. (4.6) is zero. Furthermore, by using Eq. (4.2), the mean of photocurrent in TD-OCT and with the direct light detection setup is easily denoted by,

$$E(i(t)) = \int_{-\infty}^{\infty} h_{det}(t-t')E[dN(t')], \tag{4.8}$$

and by inserting Eq. (4.6), it can be written as,

$$E[i(t)] = \int_{-\infty}^{\infty} h_{det}(t-t')E[I(t')]dt' \,. \tag{4.9}$$

In addition, the autocorrelation function of TD-OCT photocurrent with the direct light detection could be written as

$$\mathrm{E}[i(t_1)i(t_2)] = \int_{-\infty}^{\infty}\int_{-\infty}^{\infty} h_{det}(t_1-t'_1)h_{det}(t_2-t'_2)\, E[dN_1(t'_1)\, dN_2(t'_2)]\,, \tag{4.10}$$

where we have,

$$E[dN_1(t'_1)dN_2(t'_2)] = \{\rho^2\Gamma(t'_1,t'_2)+\rho E[I(t'_1)]\delta(t'_2-t'_1)\}dt'_1dt'_2. \tag{4.11}$$

4.2.1 Mean of photocurrent in direct light detection configuration

Based on Eq. (4.9), to obtain the mean of photocurrent, the mean of intensity, $E[I(t)]$, should be calculated first. In this section we describe how $E[I(t)]$ can be calculated.

A typical TD-OCT setup with direct light detection is shown in Figure 4.2.

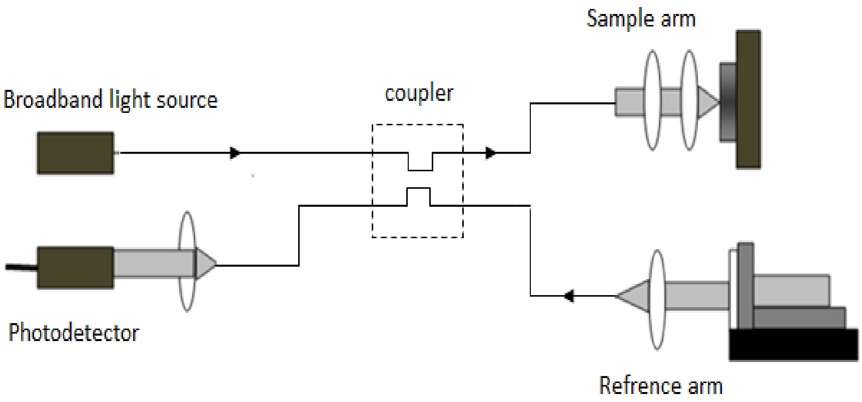

Figure 4.2: A typical time domain OCT setup with direct optical detection.

In the design of an OCT system, the optical path lengths of two interferometer arms are usually adjusted to be equal at the front surface of the object. When the mirror scans and the length of the reference arm increases the depth of imaging increases correspondingly. The speed of the scanning mirror in the reference arm is typically in the range of kHz. Hence, the instantaneous optical intensity at the detector is given by,

$$I_{OCT}(t) = |V_r[t - f(t)]|^2 + \left|\int_0^\infty V_s(t-\tau)R(\tau)d\tau\right|^2 + 2Re\left\{V_r[t-f(t)]\int_0^\infty V_s^*(t-\tau)R(\tau)d\tau\right\}, \tag{4.12}$$

where V_r and V_s are the analytic signals of electric fields at the reference and sample arms, R is the axial reflectance of the object and $(.)^*$ denotes complex conjugation. It should be mentioned that the second term of the RHS of Eq. (4.12) is the sum of reflected fields from all different depths of an object and are weighted by the reflectance of the object R at different depths. Also, the third term of the RHS of Eq. (4.12) represents the interference term between the fields from the reference and sample arms. Since the absolute values of R for most objects of interest are much smaller than unity, the effect of, $\left|\int_0^\infty V_s(t-\tau)R(\tau)d\tau\right|^2$ term can be ignored for the rest of derivation. During an A-scan, $\tau + f(t)$, represents the time delay between the field reflected by the reference mirror and the fields back- reflected from different depths of the object. In this notation τ represents the delay time due to the propagation inside the object and $f(t)$ represents the delay time due to the movement of the mirror. With the assumption that OCT optical intensity is stationary and ergodic, which is a common assumption for continuous wave sources [87], the statistical mean of the photocurrent intensity can be replaced by its time average. By substituting $V_r = aV_{src}$ and $V_s = bV_{src}$ in Eq. (4.12), where V_{src} denotes the analytic signal due to the electric field of the source and a and b are complex constants which are determined specifically for each TD-OCT setup, the mean of photocurrent intensity $E[I_{OCT}(t)]$ in TD-OCT with direct light detection configuration is given by,

$$E[I_{OCT}(t)] \cong < I_{OCT}(t) > \cong < |\alpha V_{src}[t-f(t)]|^2 > +$$
$$2Re\left\{ab^*\langle V_{src}[t-f(t)] \times \int_0^\infty {V_{src}}^*(t-\tau)R(\tau)d\tau\rangle\right\}, \tag{4.13}$$

where, in this equation, $<\cdot>$ denotes the time averaging. In a typical TD- OCT system, the time variations of the fields $V_r(t)$ and $V_s(t)$ are usually of the order of femto-second while the time variations of the reference arm delay $f(t)$ for the fastest TD-OCT setups are of the order of microseconds. Thus, $f(t)$ is approximately considered as constant when it is averaged over the time and the mean of the optical intensity can be written as,

$$E[\, I_{OCT}(t)] = |a|^2 < I_{src} > + < I_{src} > \times\, 2Re\left\{ab^* \int_0^\infty \gamma_{src}[\tau - f(t)]R(\tau)d\tau\right\}, \tag{4.14}$$

where, $< I_{src} >$ and γ_{src} are the average intensity and complex degree of coherence of the used optical source. If reference mirror is linearly scanned with the velocity of v, $f(t)$ can be replaced by αt, where $\alpha = 2\frac{v}{c_0}$ and c_0 is the speed of light in vacuum. Also by using

$$\gamma_{src}(\tau - t) = {\gamma_{src}}^*(t - \tau), \tag{4.15}$$

$E[I_{OCT}(t)]$ can be written in a convolution form as,

$$E[I_{OCT}(t)] = |a|^2 < I_{src} > + < I_{src} > 2Re\left\{ab^* \int_0^\infty {\gamma_{src}}^*(\alpha t - \tau)R(\tau)d\tau\right\}. \tag{4.16}$$

Finally, the mean of the photocurrent,$E[i(t)]$ is obtained first by calculating the mean of intensity $E[I_{OCT}(t)]$ using Eq. (4.16) and then inserting it in Eq. (4.9). This result is given by,

$$E[i(t)] = \rho|a|^2 < I_{src} > \int_{-\infty}^{\infty} h_{det}(t')dt' + \rho < I_{src} > \cdot\, h_{det}(t) \otimes 2Re\{ab^*[\gamma_{src} \otimes R](\alpha\tau)\}. \tag{4.17}$$

4.2.2 Autocorrelation Function of the photocurrent in direct light detection configuration

To obtain the autocorrelation function of the photocurrent in TD-OCT system with direct light detection, first the autocorrelation function of intensity I_{OCT} is obtained. To simplify the derivation, the following relation is used,

$$\Gamma_{I_{OCT}}(t_1, t_2) = E[I_{OCT}(t_1) I_{OCT}(t_2)] =$$

$$E[I_{OCT}^{dc}(t_1) I_{OCT}^{dc}(t_2)] + 2E[I_{OCT}^{dc}(t_1) I_{OCT}^{int}(t_2)] + E[I_{OCT}^{int}(t_1) I_{OCT}^{int}(t_2)], \quad (4.18)$$

where $I_{OCT}^{dc}(t)$ and $I_{OCT}^{int}(t)$ are the DC and interferometric intensity components which are given by,

$$I_{OCT}^{dc}(t) = |aV_{src}[t(1-a)]|^2$$

$$I_{OCT}^{int}(t) = 2Re\left\{ab^* V_{src}[t(1-\alpha)] \int_0^\infty V_{src}^*(t-\tau) R(\tau) d\tau\right\}. \quad (4.19)$$

In addition, as the electric field of polarized thermal light has a complex Gaussian random process [86], the Gaussian moment theorem can be applied [84]. This theorem states that the fourth order correlation function of complex Gaussian random variables V_i is given by [7],

$$E[V_1^* V_2^* V_3 V_4] = E[V_1^* V_3] E[V_2^* V_4] + E[V_1^* V_4] E[V_2^* V_3]. \quad (4.20)$$

With the assumption of $1 - \alpha \cong 1$, the autocorrelation function of the dc term of the intensity (I_{OCT}^{dc}) is obtained using,

$$E[I_{OCT}^{dc}(t_1) I_{OCT}^{dc}(t_2)] = |a|^4 < I_{src} >^2 (1 + |\gamma_{src}(t_2 - t_1)|^2). \quad (4.21)$$

Also, the autocorrelation function of the interference term of the field intensity which is denoted by,

$$E\left[I_{OCT}^{int}(t_1)I_{OCT}^{int}(t_2)\right] = 2 < I_{src} >^2\cdot \tag{4.22}$$

$$Re\left\{\begin{array}{l} (ab^*)^2\left[\begin{array}{c}\int_0^\infty \gamma_{src}{}^*(\alpha t_1-\tau)R(\tau)d\tau \int_0^\infty \gamma_{src}{}^*(\alpha t_2-\tau)R(\tau)d\tau + \\ \int_0^\infty \gamma_{src}(t_2-t_1+\tau)R(\tau)d\tau \int_0^\infty \gamma_{src}(t_1-t_2+\tau)R(\tau)d\tau\end{array}\right] + \\ \\ |a|^2|b|^2\left[\begin{array}{c}\int_0^\infty \gamma_{src}{}^*(\alpha t_1-\tau)R(\tau)d\tau . \int_0^\infty \gamma_{src}(\alpha t_2-\tau)R^*(\tau)d\tau\ + \\ \\ \gamma_{src}(t_1-t_2)\int_0^\infty\int_0^\infty \gamma_{src}(t_2-t_1+\tau_1-\tau_2)R(\tau_1)R^*(\tau_2)d\tau_1 d\tau_2\end{array}\right]\end{array}\right\},$$

and the cross correlation function of the dc intensity component $I_{OCT}^{dc}(t_1)$ and the interferometric intensity component $I_{OCT}^{int}(t_2)$ is given by,

$$2E\left[I_{OCT}^{dc}(t_1)I_{OCT}^{int}(t_2)\right] = 4|a|^2 < I_{src} >^2\times \tag{4.23}$$

$$Re\left\{ab^*\left[\int_0^\infty \gamma_{src}{}^*(\alpha t_2-\tau)R(\tau)d\tau + \gamma_{src}(t_2-t_1)\int_0^\infty \gamma_{src}{}^*(t_2-t_1-\tau)R(\tau)d\tau\right]\right\}.$$

Finally, the autocorrelation function of TD-OCT photocurrent with direct detection configuration is denoted by,

$$E[i_{OCT}(t_1)i_{OCT}(t_2)] =$$

$$\rho^2\int_{-\infty}^{\infty}\int_{-\infty}^{\infty} h_{det}(t_1-t'_1)h_{det}(t_2-t'_2)\times\Gamma_{I_{OCT}}(t'_1,t'_2)dt'_1dt'_2 +$$

$$\rho\int_{-\infty}^{\infty} h_{det}(t_1-t'_1)h_{det}(t_2-t'_1)\,E[I_{OCT}(t'_1)]dt'_1, \tag{4.24}$$

where $E[I_{OCT}(t)]$ and $\Gamma_{I_{OCT}}(t_1,t_2)$ are given by Eq. (4.14) and Eq. (4.18), respectively, and by the relations given by Eq. (4.21) – Eq. (4.23). .

4.3 TD-OCT with differential optical detection

As explained in Chapter 2, this configuration of a TD-OCT technique is employed in order to remove the excess photon noise due to the broad bandwidth of the optical source, thereby increasing the sensitivity and the SNR of the system.. A typical TD-OCT system with the differential optical detection is shown in Figure 4.3.

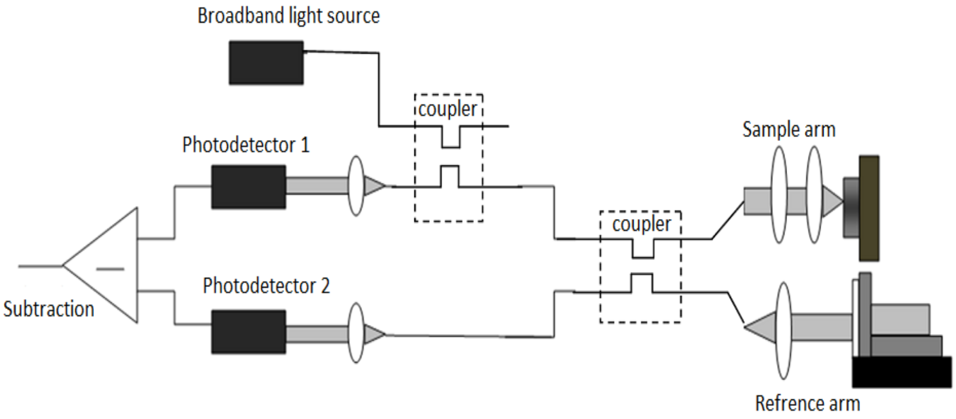

Figure 4.3: A typical TD-OCT setup with differential optical detection.

4.3.1 Mean of photocurrent in differential light detection configuration

In TD-OCT system with a differential light detection scheme, the incident light is equally split into two beams with the intensities $I_1(t)$ and $I_2(t)$ that are directly detected using two identical but independent detectors. The photocurrent of these two detectors $i_1(t)$ and $i_2(t)$ are subtracted to give the final TD-OCT differential photocurrent $i_{diff}(t)$ given by,

$$i_{diff}(t) = i_2(t) - i_1(t). \tag{4.25}$$

This subtraction allows the elimination of the constant background signal and thereby increasing the SNR in comparison with the direct light detection configuration in TD-OCT systems. By using the linear properties of operator $E[\cdot]$, the mean of photocurrent is given by,

$$E[\, i_{diff}(t)] = E[i_2(t) - i_1(t)] = E[i_2(t)] - E[i_1(t)], \tag{4.26}$$

and the autocorrelation function of the differential photocurrent is given by

$$E[\, i_{diff}(t_1)\, i_{diff}(t_2)] =$$

$$E[i_1(t_1)i_1(t_2)] - 2\mathrm{E}\,[i_1(t_1)i_2(t_2)] \;+\; E[i_2(t_1)i_2(t_2)], \tag{4.27}$$

where $E[i_j(t)]$ and $E[i_j(t_1)i_j(t_2)]$ are the mean and autocorrelation function of i_j at each detector and while $\{j = 1,2\}$. The second term in the right hand side of Eq. (4.27) is the cross correlation function of the photocurrents i_1 and i_2 in both detectors which is given by

$$\mathrm{E}\,[i_1(t_1)i_2(t_2)] =$$

$$\int_{-\infty}^{\infty}\int_{-\infty}^{\infty} h_{det}(t_1 - t'_1)h_{det}(t_2 - t'_2) \times\, E[dN_1(t_1')dN_2(t_2')], \tag{4.28}$$

where,

$$E[dN_1(t'_1)dN_2(t'_2)] =$$

$$\{\rho^2\Gamma(t'_1, t'_2) + \rho E[I(t'_1)]\delta(t'_2 - t'_1)\}dt'_1 dt'_2, \tag{4.29}$$

and Γ is the crosscorrelation function between the intensities of I_1 and I_2 at the output of the two detectors. As shown above, the mean of the TD-OCT photocurrent in the first detector, E $[\mathrm{i}_{\mathrm{OCT}_1}(t)]$ is given by

$$E[\mathrm{i}_{\mathrm{OCT}_1}(t)]\,] = \rho|a|^2 < I_{src} > \int_{-\infty}^{\infty} h_{det}(t')dt' +$$

$$\rho < I_{src} >\cdot h_{det}(t)\otimes 2Re\{ab^*[\gamma_{src}\otimes R](\alpha\tau)\}. \qquad (4.30)$$

The mean of the photocurrent in the second detector $\mathrm{E}\,[\mathrm{i}_{\mathrm{OCT}_2}(t)]$ has the same expression as $\mathrm{E}\,[\mathrm{i}_{\mathrm{OCT}_1}(t)]$ while b term is replaced by $-b$ because of a phase shift of 180° that exist between the two interfering optical fields. Hence, the mean of the photocurrent in TD-OCT system with the differential light detection is calculated using Eq. (4.30) and Eq. (4.26) and the result is given by

$$\mathrm{E}\,[\mathrm{i}_{\mathrm{OCT}_{\mathrm{diff}}}(t)] = \rho < I_{src} > h_{det}(t)\otimes 2Re\{ab^*[\gamma_{src}\otimes R](\alpha t)\}. \qquad (4.31)$$

4.3.2 Autocorrelation function of photocurrent in differential light detection configuration

For calculating the autocorrelation function in differential light detection configuration, the starting point is the relation

$$E\left[i_{OCT_1}(t_1)i_{OCT_1}(t_2)\right] =$$

$$\rho^2\int_{-\infty}^{\infty}\int_{-\infty}^{\infty} h_{det}(t_1-t'_1)h_{det}(t_2-t'_2)\times\Gamma_{I_{OCT}}(t'_1,t'_2)dt'_1dt'_2 +$$

$$\rho\int_{-\infty}^{\infty} h_{det}(t_1-t'_1)h_{det}(t_2-t'_1)\,E[I_{OCT}(t'_1)]dt'_1\,, \qquad (4.32)$$

for one detector and by just inserting $\frac{I}{2}$ instead of intensity of I in this relation. Also the autocorrelation function of TD-OCT photocurrent in the second detector $E[i_{OCT_2}(t_1)i_{OCT_2}(t_2)]$ has the same expression just with replacing term b with $-b$. To obtain the cross correlation function of $E[i_{OCT_1}(t_1)i_{OCT_2}(t_2)]$, $\Gamma_{I_{OCT_1},I_{OCT_2}}(t_1,t_2)$, should be calculated first. To simplify calculations, $\Gamma_{I_{OCT_1},I_{OCT_2}}(t_1,t_2)$, is written in the form of

$$\Gamma_{I_{OCT_1},I_{OCT_2}}(t_1,t_2) = E\{[I^{dc}_{OCT_1}(t_1) + I^{int}_{OCT_1}(t_1)][I^{dc}_{OCT_2}(t_2) - I^{int}_{OCT_2}(t_2)]\} =$$

$$E[I^{dc}_{OCT_1}(t_1)I^{dc}_{OCT_2}(t_2)] - E[I^{int}_{OCT_1}(t_1)I^{int}_{OCT_2}(t_2)]. \qquad (4.33)$$

In this expression, $I^{dc}_{OCT_1} = I^{dc}_{OCT_2}$ and $I^{int}_{OCT_1} = I^{int}_{OCT_2}$ and the terms of $E[I^{dc}_{OCT_1}(t_1)I^{dc}_{OCT_2}(t_2)]$ and $E[I^{int}_{OCT_1}(t_1)I^{int}_{OCT_2}(t_2)]$ is calculated by Eq. (4.21) and Eq. (4.22), respectively. Substituting Eq. (4.33) in Eq. (4.11) and Eq. (4.10), the cross correlation function of $E[i_{OCT_1}(t_1)i_{OCT_2}(t_2)]$ is obtained. Finally using Eq. (4.27), the autocorrelation function of photocurrent in a TD-OCT system with the differential light detection is given by,

$$E[i_{OCT_{diff}}(t_1)i_{OCT_{diff}}(t_2)] =$$

$$\rho^2 \int_{-\infty}^{\infty}\int_{-\infty}^{\infty} h_{det}(t_1 - t'_1)h_{det}(t_2 - t'_2) \times \Gamma^{int}_{OCT}(t'_1, t'_2)dt'_1 dt'_2 +$$

$$\rho|a|^2 < I_{src} > \times \int_{-\infty}^{\infty} h_{det}(t_1 - t'_1)h_{det}(t_2 - t'_1)\, dt'_1 . \qquad (4.34)$$

4.4 Joint PDF of TD-OCT photocurrent and effect of thermal electronic fluctuations

Since the SNR of an OCT system is typically high (>80dB), the Joint Probability Distribution Function (JPDF) of the depth scan photocurrent could be approximated as a Gaussian random process with statistical mean and correlation functions given by Eq. (4.17) and Eq. (4.24) for the direct light detection case and Eq. (4.31) and Eq. (4.34) in differential light detection configuration.

As it was mentioned before, the additive noise term in TD-OCT photocurrent consists of shot noise, photon access noise and thermal noise in the detector. The effect of the electronic thermal fluctuations $n_{elect}(t)$ in the optical detector could be considered as a white Gaussian random process [88], with zero mean and autocorrelation function of

$$E[n_{elect}(t_1)n_{elect}(t_2)] = \frac{4K_BTB}{R_L}\delta(t_2 - t_1)], \qquad (4.35)$$

where , K_B is the Boltzmann's constant, B is the electrical Bandwidth of the detector and R_L is the equivalent load resistance at temperature T. Since electronic thermal fluctuations are independent of the shot noise and photon access noise in the OCT photocurrent, the autocorrelation function of these fluctuations, Eq. (4.35), can be added to the autocorrelation function of the OCT photocurrent, Eq. (4.24), yielding a general expression

$$E\left[i_{OCT_{General}}(t_1)i_{OCT_{General}}(t_2)\right] =$$

$$E[i_{OCT}(t_1)i_{OCT}(t_2)] + E[n_{elect}(t_1)n_{elect}(t_2)], \qquad (4.36)$$

for the TD-OCT system with direct light detection.. In a TD-OCT system with the differential light detection, an equivalent resistance R_{eq} (represents equivalent resistance of the two detectors) is used instead of R_L in both Eq. (4.35) and Eq. (4.34).

4.5 Signal dependent noise in TD-OCT

Considering the mathematical expressions of Eq. (4.24) for the direct light detection and Eq. (4.34) for the differential light detection in TD-OCT systems, it can be observed that the autocorrelation function of the depth-scan photocurrent in both TD-OCT configurations are dependent to the Γ_{OCT} term, which itself depends on the axial reflectance of the object R. This is an object dependent variable that typically varies with the depth of OCT imaging. Hence, the statistics of noise clearly changes with the value of OCT signal that typically varies with the depth of OCT imaging. This variation of noise confirms the non-stationary nature of the OCT photocurrent. By considering this non-stationary property of the depth-scan photocurrent, many statistical signal or image processing methods can be developed to process the OCT data. These methods would be more accurate as they consider the depth variant statistics of OCT depth-scans. These statistical processing methods can be used for, e.g., deconvolution and dispersion compensation.

Chapter 5

Empirical Estimation and Verification of Noise Statistics in TD-OCT

The non-stationary statistical model of a depth-scan photocurrent in TD-OCT, developed in [5], was reviewed in Chapter 4. In this model, it is assumed that each depth-scan photocurrent can be considered a Gaussian random process that is completely determined by its second order statistics. In this model, the mean and correlation functions of the depth-scan photocurrent were theoretically derived. It was shown that the depth dependant variation of correlation function is due to its dependency to the axial reflectance of the object. This proves the non-stationary property of a depth-scan photocurrent in TD-OCT systems.

In this Chapter, we describe an empirical study on OCT measurements to verify the non-stationary property of TD-OCT A-scans. In Section 5.1, the TD-OCT setup that was used performs our OCT measurements are explained. In Section 5.2, an empirical method to estimate of the second order statistics (statistical mean and covariance function) of a depth-scan photocurrent is described. By applying this empirical method, the covariance functions of samples of photocurrent taken from vascular rabbit tissue and fishing line are estimated and presented in Section 5.3. The results of these estimates are graphically presented in this section. Furthermore, the dependence of noise on the OCT signal and its variation with different depths of imaging is verified by using these results. In Section 5.4 the construction of an OCT image from a set of measured photocurrents is described. In Section 5.5 some common post processing steps in OCT are introduced. In Section 5.6 a relation between SNR values of a signal and corresponding envelope is described. This relation is useful if one needs to apply an image processing method to an OCT image instead of OCT photocurrent. In this thesis this relation is useful to show the optimality of our designed depth-dependent matched filter of Chapter 6, in maximizing the SNR, when it is directly applied to an OCT image. Finally, in Section 5.7, the non-stationary property of TD-OCT envelopes is demonstrated through empirical estimates of the covariance functions of the envelopes of our OCT measurements.

5.1 TD-OCT setup

To perform our OCT experiments, a TD-OCT setup with the following specifications was used:

- Frequency of scanning is 148 A-scan per second. Hence, the total time of each A-Scan is $\frac{1}{148}$ second.
- Total number of pixels in each A-scan is 3700, therefore the time interval between two pixels is

$$T_{Pixel\ to\ Pixel} = \frac{\frac{1}{148}}{3700} = 5.64\ \mu \text{ seconds.} \tag{5.1}$$

- The bandwidth of photo-detector is 2GHz.
- Total depth of imaging is 4 mm.

- Coherence length of the optical source is $20\ \mu m$.

This TD-OCT setup was used to image a sample of rabbit vascular tissue and also a sample of fishing-line (in tow different directions one time along the length of fishing-line and the other time along the width of fishing-line). During our imaging experiments, each A-scan was measured 20 times. A sample of our TD-OCT images of vascular rabbit tissue is shown in Figure .5.1. We observe that this image consists of 650 A-scans with the imaging depth of 4mm. This image shows a surface layer of vascular rabbit tissue. We also observe that features deep in the tissue are not clear. We note that the OCT images of the fishing line (taken along its length and width directions) are only used as a sample to study the second order statistics of noise and to confirm the non stationary property of noise in TD-OCT. However the OCT images of vascular rabbit tissue are used to study and confirm the non-stationary nature of noise in TD-OCT, in addition to being used to design our proposed depth-dependent matched filter in Chapter 6.

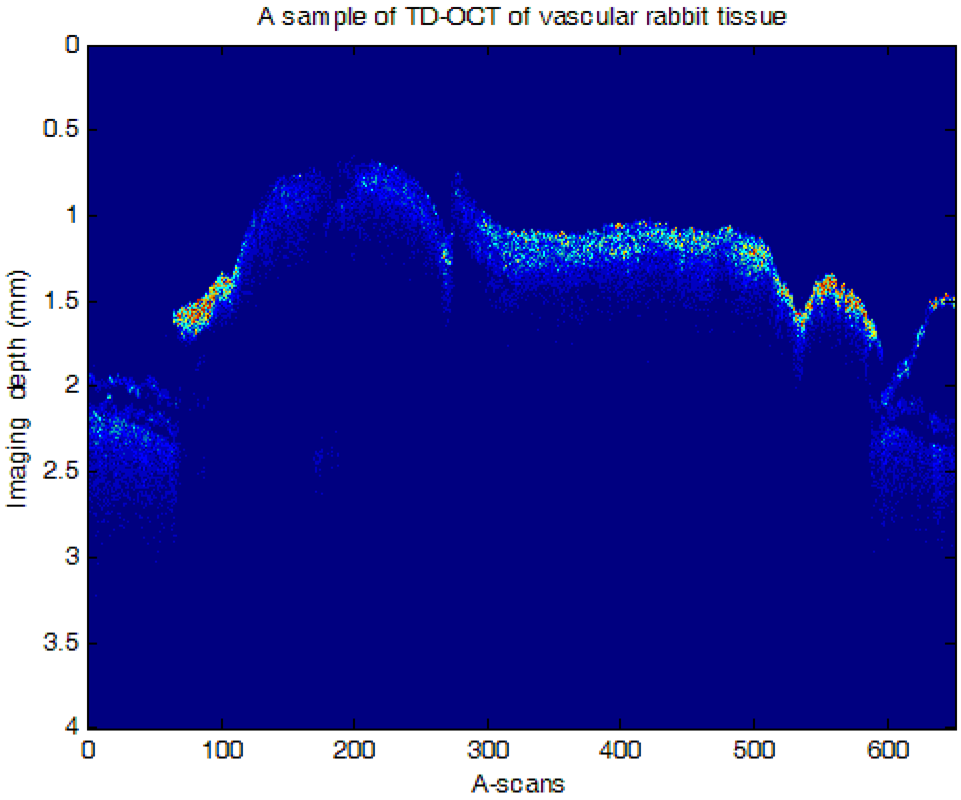

Figure 5.1: A sample of TD-OCT image of vascular rabbit tissue.

Figure 5.2 and Figure 5.3 show other samples of our TD-OCT measurements of a fishing-line that is imaged along its length and along its width directions separately. We note from these Figures that the number of A-scans in these images is 1000 and the depth of imaging is 4 mm.

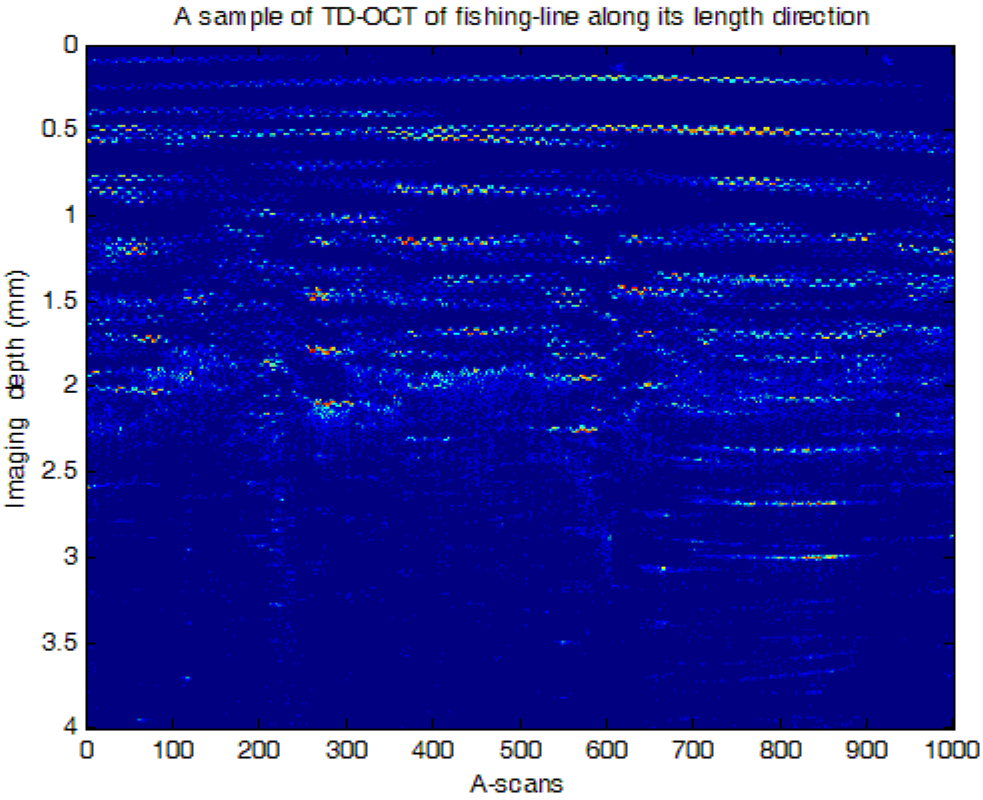

Figure 5.2: A sample of TD-OCT of fishing-line imaged along its length direction.

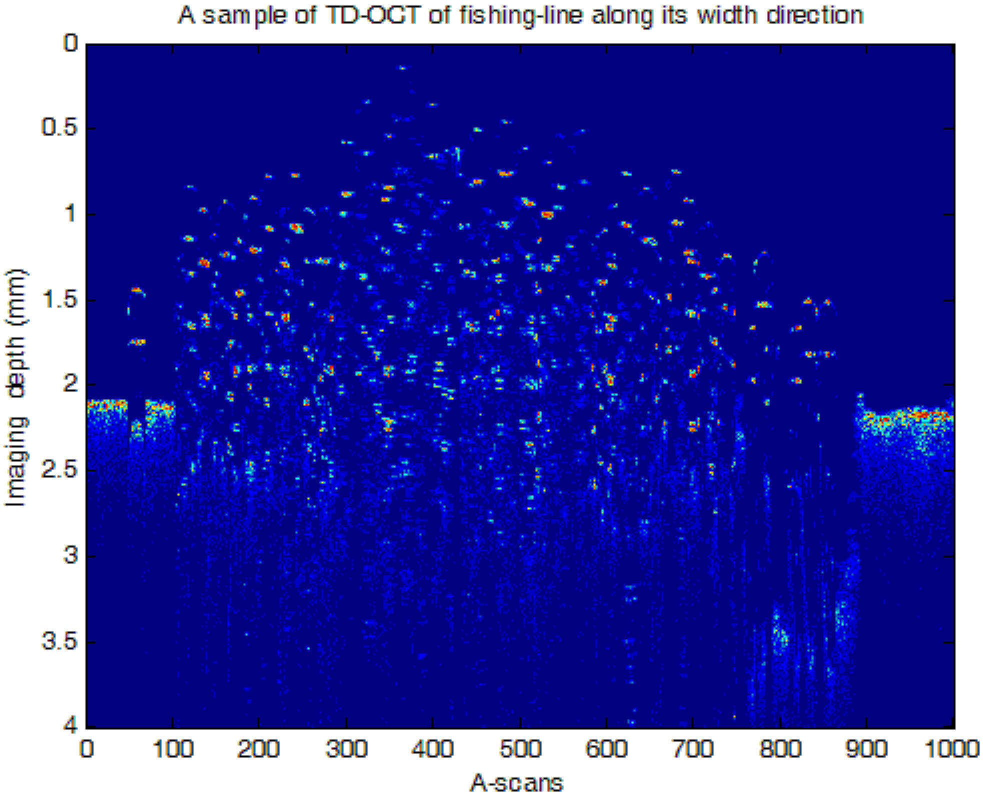

Figure 5.3: A sample of TD-OCT of fishing-line imaged along its width direction.

5.2 Empirical estimation and verification of photocurrent statistics

In this section, we present a description of an empirical estimate of the signal-dependent noise statistics from a set of N repeated images. Let $\boldsymbol{y}$ be a column vector that represents a single depth-scan photocurrent from a set of N repeated depth-scan measurements. An empirical estimate of the mean of a depth-scan $\boldsymbol{y}$ is denoted by,

$$\hat{\boldsymbol{s}} = E_N[\boldsymbol{y}], \tag{5.2}$$

where, $E_N[\cdot]$ denotes ensemble averaging over N different measurements.

Also, the covariance matrix of each single depth-scan can be empirically estimated using,

$$\widehat{\boldsymbol{C}} = E_N[\boldsymbol{y}\boldsymbol{y}^{\boldsymbol{T}}] - E_N[\boldsymbol{y}].\, E_N[\boldsymbol{y}^{\boldsymbol{T}}]. \tag{5.3}$$

where $E_N[\boldsymbol{y}\boldsymbol{y}^{\boldsymbol{T}}]$ is the correlation matrix of the depth-scan photocurrent. We could legitimately represent any a posteriori (after measurement) A-scan as a random process,

$$\boldsymbol{y} = \boldsymbol{s} + \boldsymbol{n}\,, \tag{5.4}$$

where, $\boldsymbol{s}$ is estimated by Eq. (5.2) and $\boldsymbol{n}$ is a noise term of zero mean and estimated covariance function given by Eq. (5.3).

5.3 Results of estimated photocurrent noise covariance matrix

In this section, our photocurrent OCT measurements from vascular rabbit tissue are used to empirically estimate the noise covariance function of a depth-scan photocurrent by using Eq. (5.3). In addition, the non-stationary property of this depth-scan photocurrent is verified at different depths of imaging. We consider the ensemble average of our 20 photocurrent measurements, shown in Figure 5.4(a), of one A-scan of our OCT image. Then we estimate the noise covariance function of this signal by using Eq. (5.3). The diagonal elements of this covariance matrix represent the power of noise that is present in this depth-scan photocurrent. These diagonal elements are plotted in Figure 5.4(b). As we can see from this plot, the power of noise varies with the value of the photocurrent at different imaging depths. The peak value of noise power occurs when the OCT photocurrent has its maximum value. For this example, to verify the non-stationary property of the depth-scan photocurrent, local covariance matrices are calculated for sliding windows at different depths of imaging. A window size of 40 pixels is used, which is approximately equivalent to 0.04 mm in imaging depth for this sample. These local estimates of the covariance function for different depths of imaging are shown in Figure 5.5(a-d).

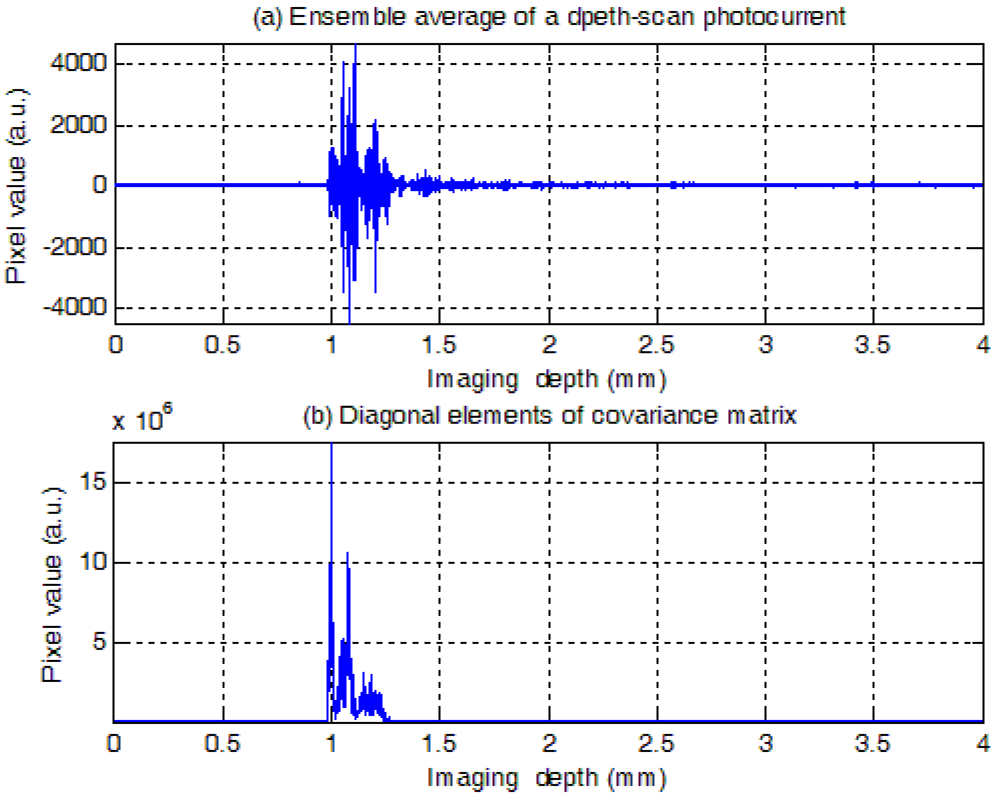

Figure 5.4: Ensemble average of a depth-scan photocurrent of vascular rabbit tissue, (b) diagonal elements of covariance matrix for the depth-scan photocurrent of part (a).

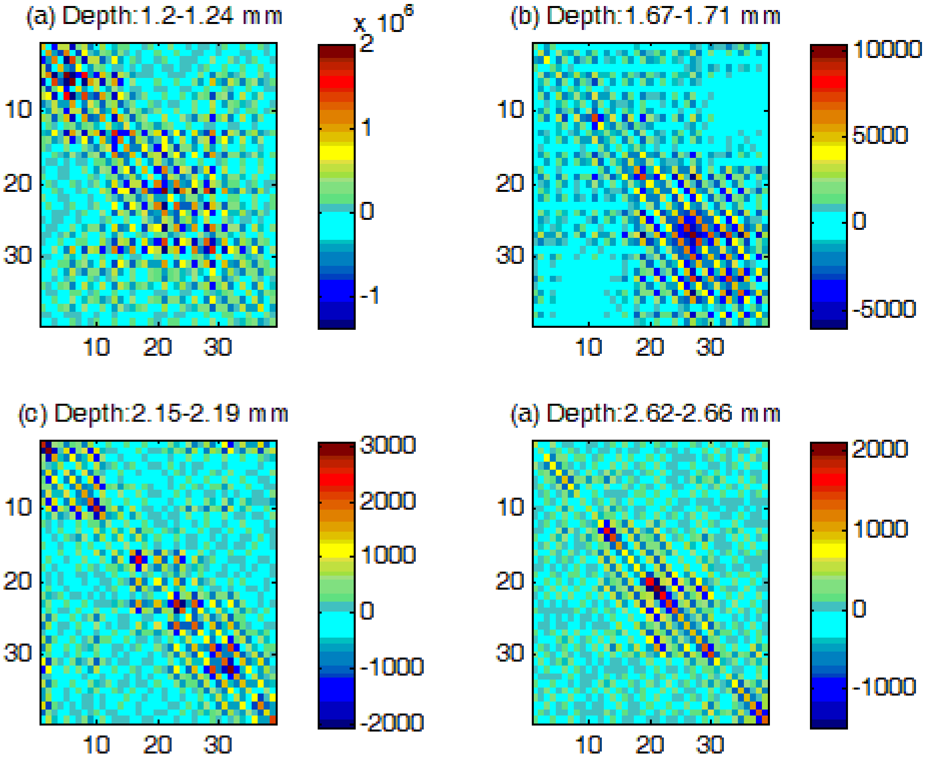

Figure 5.5: Empirical estimates of noise covariance matrix of a depth-scan photocurrent of vascular rabbit tissue at different ranges of imaging depth.

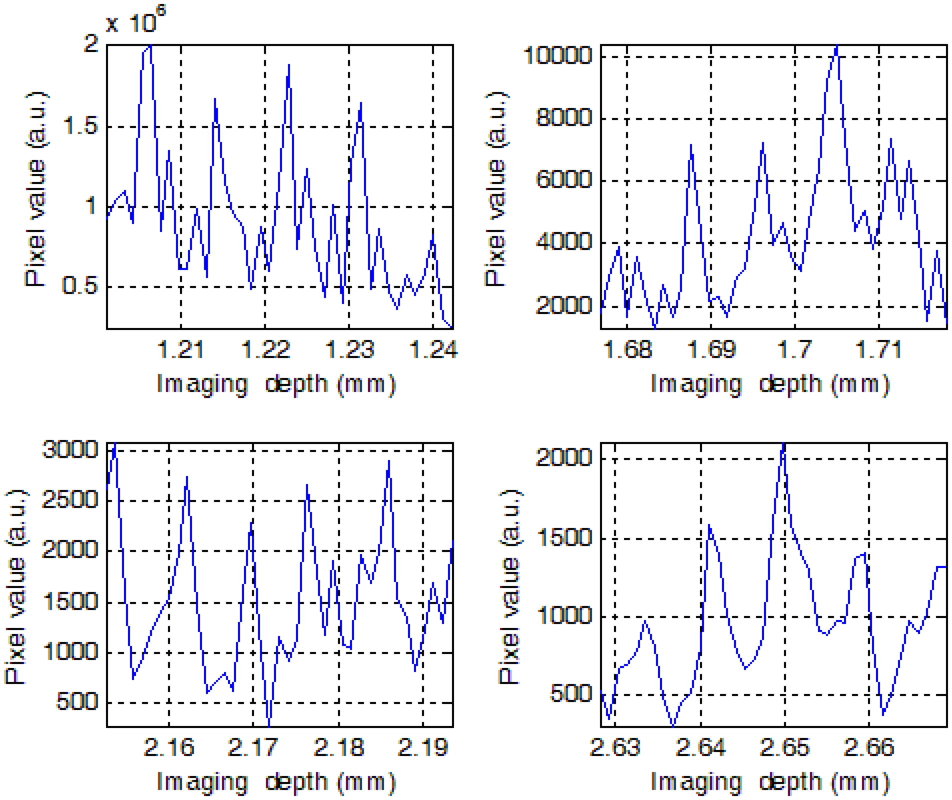

Figure 5.6: Diagonal elements of covariance matrix in different ranges of imaging depth.

On examining the local covariance matrices of Figure 5.5 (a-d) as well as corresponding plots of Figure 5.6 (a-d), we observe that the pattern of the covariance matrix changes with the depth of imaging due to the change in value of the depth-scan signal. This clearly demonstrates the non-stationary nature of the noise in a depth-scan photocurrent in TD-OCT.

As another example, the depth-scan photocurrent shown in Figure 5.7(a) is used to estimate the local covariance matrices of the noise present in sliding windows of size 70 pixels, which is equivalent to 0.07 mm in imaging depth for this sample. Different depths of imaging are considered to estimate the covariance functions. The noise power of this depth-scan is plotted in Figure 5.7(b). As this plot shows, the power of noise varies with the depth of imaging and has its maximum value when the photocurrent has its maximum value.

(a) Ensemble average of a dpeth-scan photocurrent

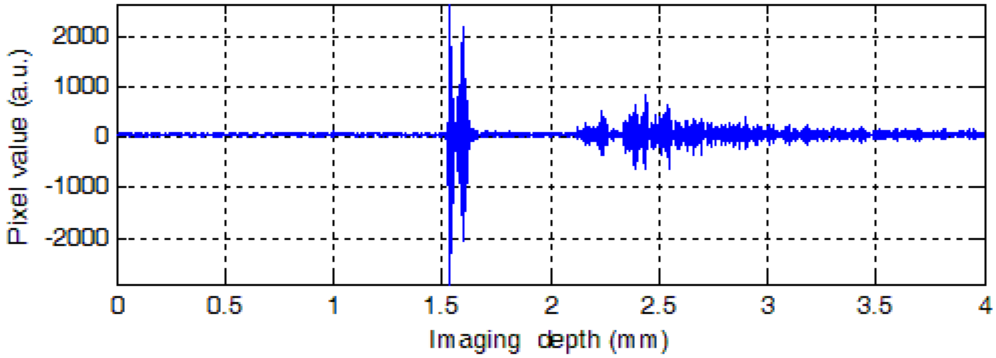

(b) Diagonal elements of covariance matrix

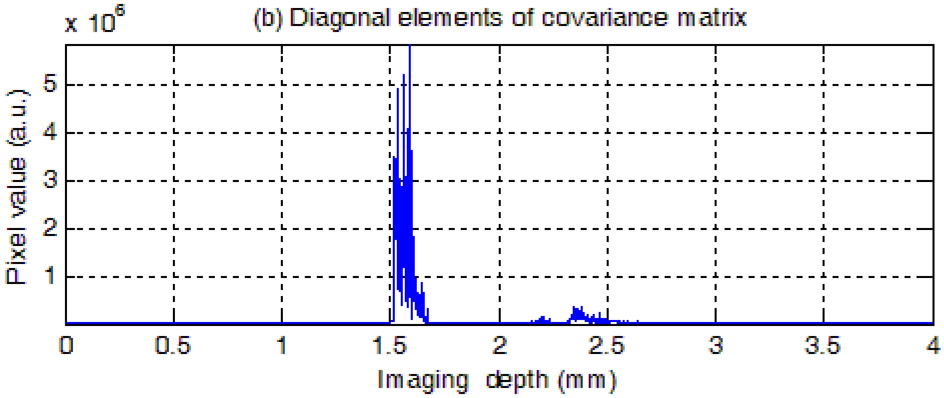

Figure 5.7: (a) An arbitrary depth-scan photocurrent of vascular rabbit tissue, (b) diagonal elements of the covariance matrix for the depth-scan photocurrent of part (a).

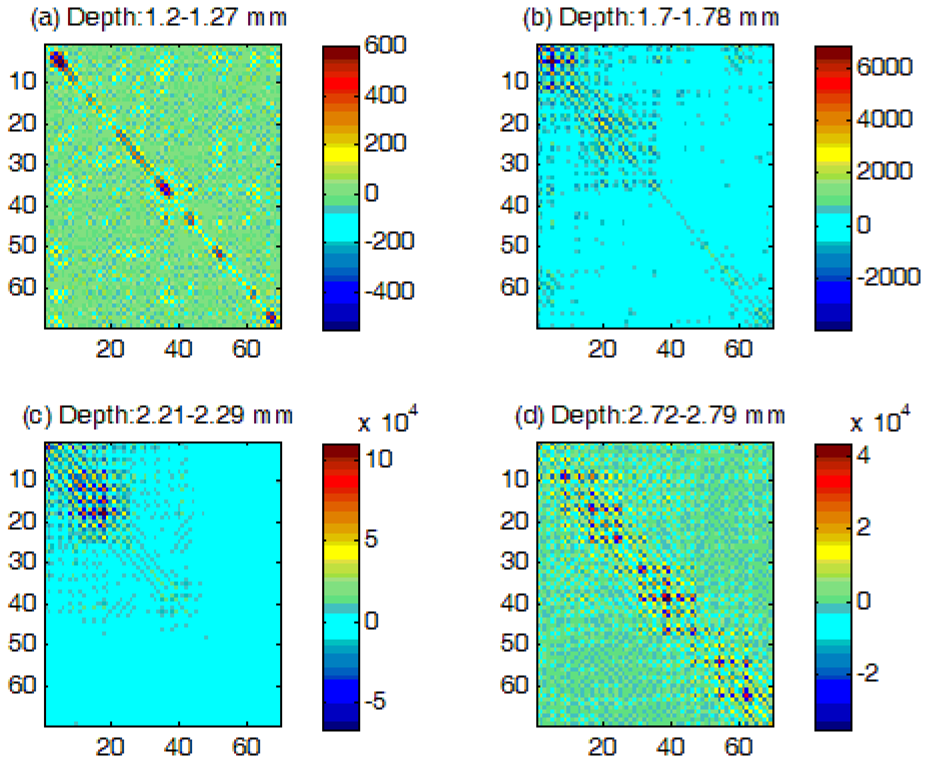

Figure 5.8: Empirical estimates of noise covariance matrix of depth-scan photocurrent of vascular rabbit tissue at different ranges of imaging depth.

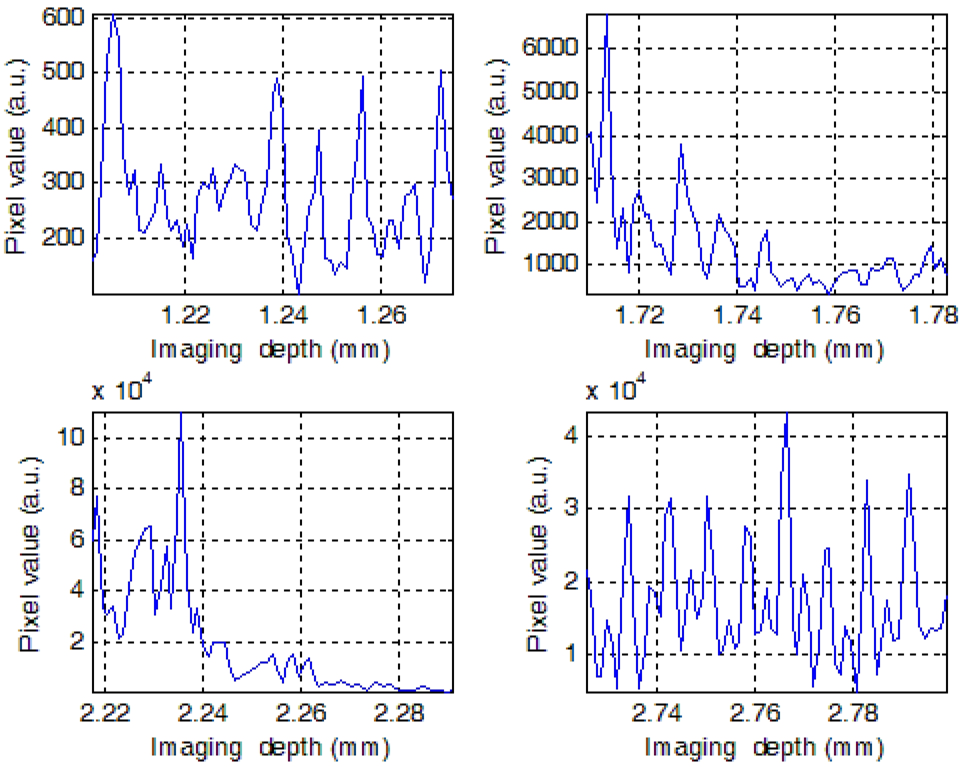

Figure 5.9: Diagonal elements of covariance matrix at different ranges of imaging depth.

The graphical results of Figure 5.8(a-d) and their corresponding plots of Figure 5.9(a-d) also confirm the non-stationary nature of the noise in this depth-scan photocurrent, as the local covariance matrices clearly change within different ranges of imaging depth.

5.4 Constructing an OCT image using depth-scan photocurrents

Each OCT image is constructed using a set of envelopes of depth-scan photocurrents. For this aim, the envelope of each single depth-scan photocurrent is obtained by,

$$\boldsymbol{y}_{Env} = \sqrt{\mathbf{y}^2 + \mathbf{y}_\mathrm{h}{}^2}\,, \tag{5.5}$$

where, $\boldsymbol{y}$ is the depth-scan photocurrent and $\mathbf{y}_\mathrm{h}$ denotes the Hilbert transform of $\mathbf{y}$. Samples of calculated envelopes and corresponding depth-scan photocurrents from vascular rabbit tissue are shown in Figure 5.10 (b, a) and Figure 5.11(b, a).

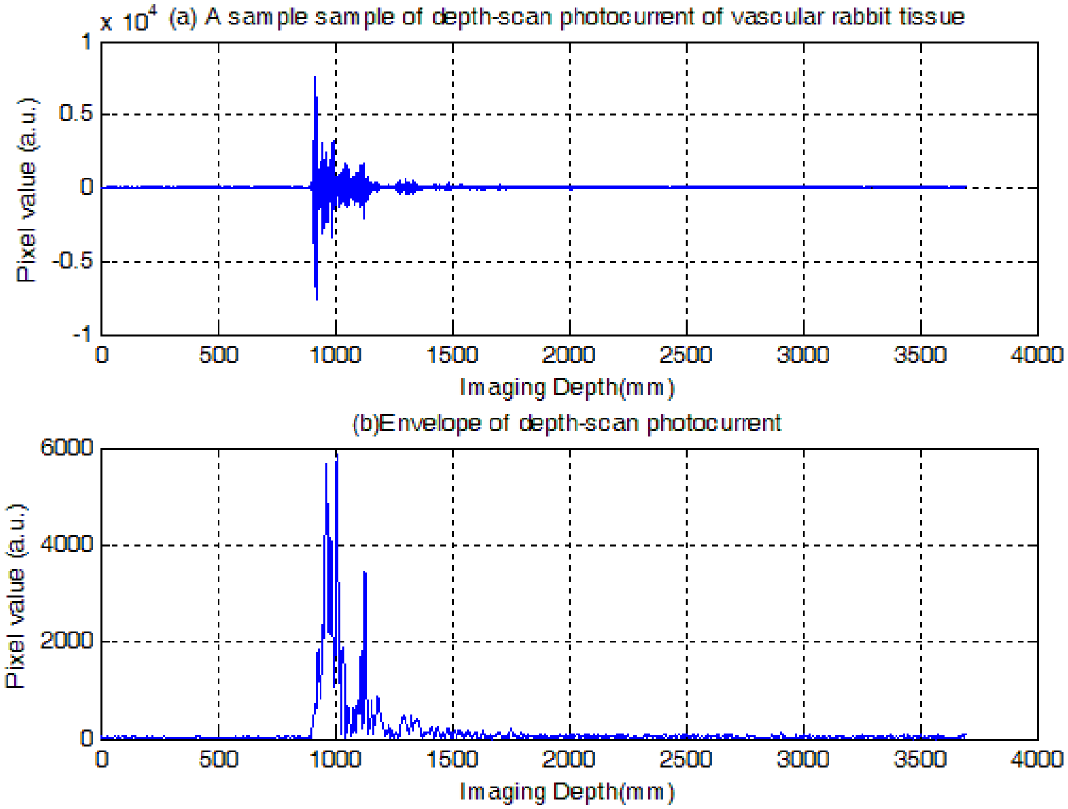

Figure 5.10: (a) A sample of depth-scan photocurrent of vascular rabbit tissue, (b) corresponding depth-scan photocurrent envelope.

(a) A sam ple sam ple of depth-scan photocurrent of vascular rabbit tiss ue

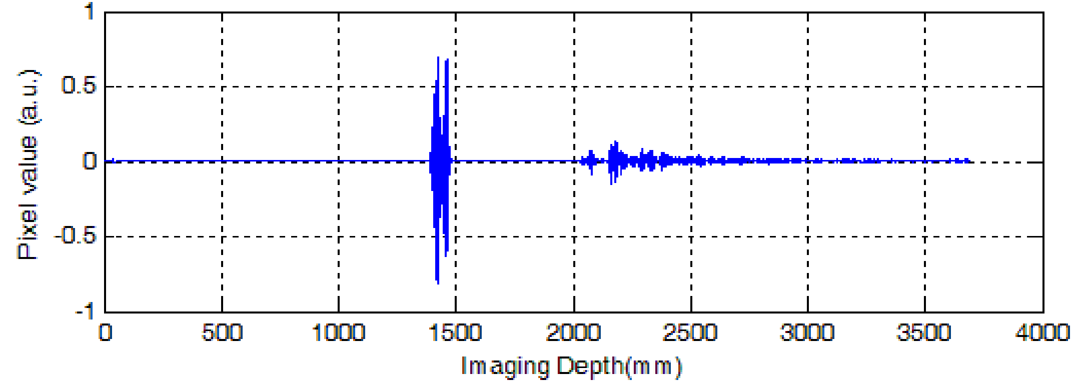

(b)Envelope of depth-scan photocurrent

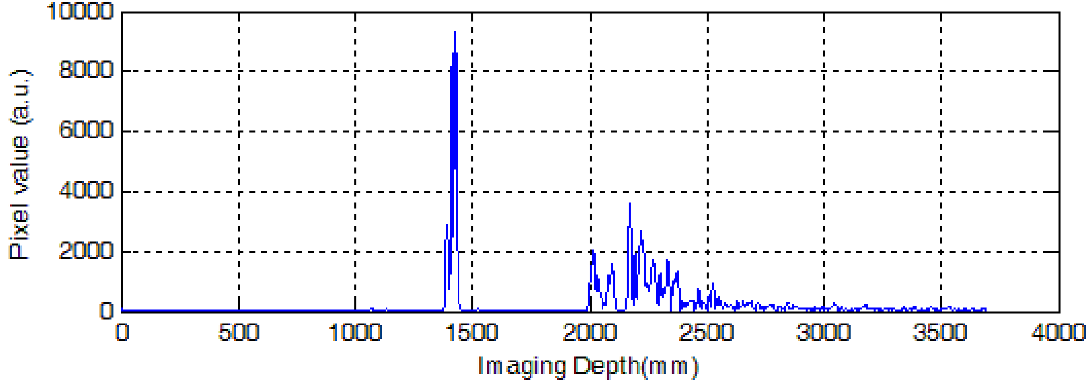

Figure 5.11: (a) A sample of depth-scan photocurrent of vascular rabbit tissue, (b) corresponding depth-scan photocurrent envelope.

The final TD-OCT image which is constructed by using a set of 650 depth-scan photocurrent envelopes is shown in Figure 5.12.

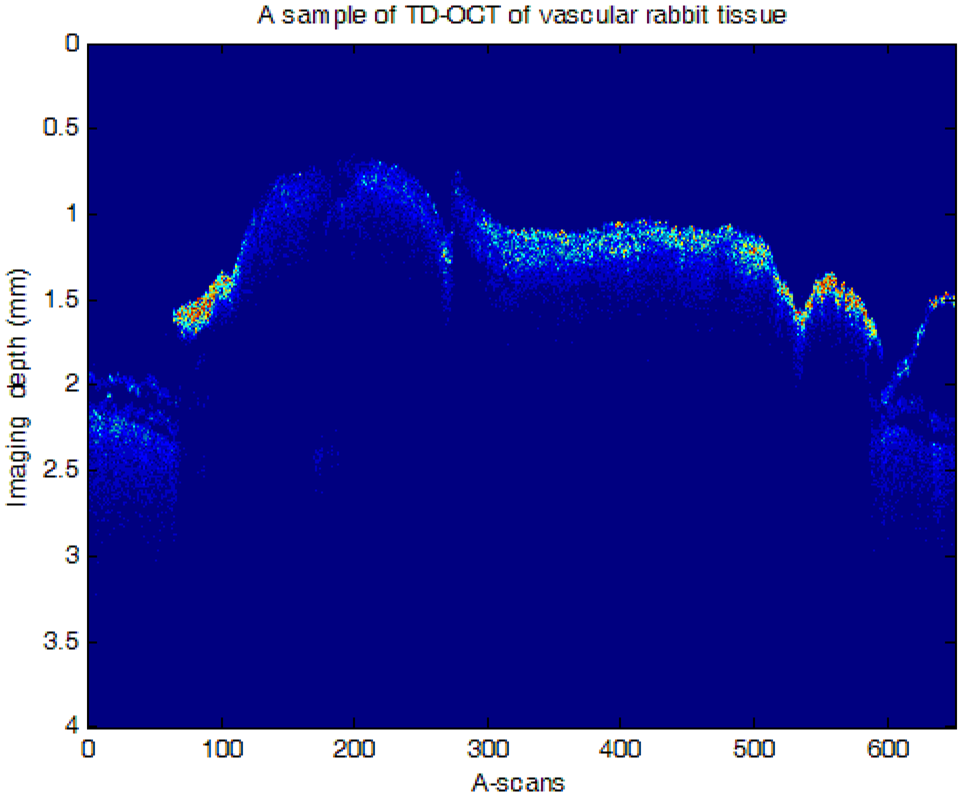

Figure 5.12: (a) A sample of constructed OCT image of rabbit vascular tissue using a set of 650 photocurrent envelopes.

5.5 Post-processing of depth-scan photocurrent in TD-OCT

In all types of OCT systems, analog or digital circuits are applied to process the depth-scan OCT photocurrent which is the output of the optical detector. In TD-OCT systems, the depth-scan photocurrent that is generated at the output of optical detector is first amplified using a suitable amplifier and then filtered to reduce the effect of noise on the depth-scan photocurrent. Finally, this signal is rectified and demodulated to obtain the envelope of the depth-scan photocurrent. Figure 5.13 shows a block diagram of these common post-processing stages in OCT imaging system.

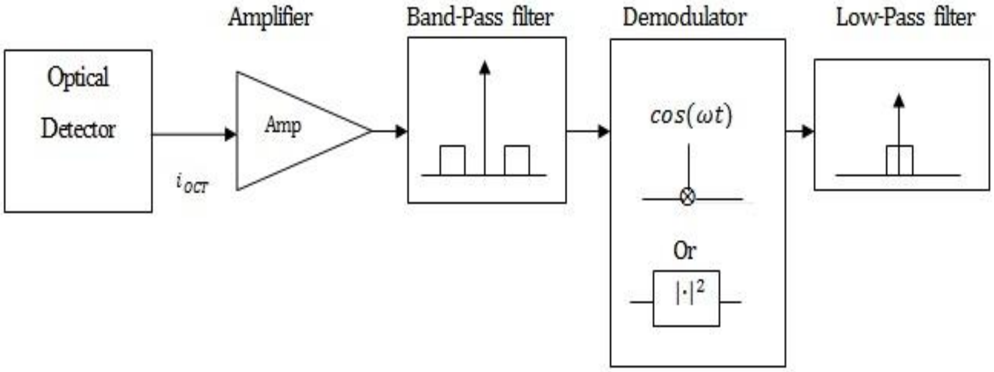

Figure 5.13: Block diagram of common post-processing stage in a TD-OCT system.

In the post-processing stage of OCT data, many image processing algorithms could be directly applied on the OCT images (envelopes of depth-scan OCT photocurrents) instead of applying them on the depth-scan photocurrents. Hence, the optimality of image processing methods that are designed to maximize the signal-to-noise ratio (SNR) of the depth-scan photocurrent should be justified if they are directly applied to the OCT photocurrent envelopes.

5.6 Relation between SNR value in depth-scan photocurrent and its corresponding envelope

One of the quality measures for evaluating the performance of image processing methods that are applied on OCT data is the SNR value. In this thesis, this measure is applied to evaluate the performance of our proposed depth-dependent matched filter of Chapter 6. In addition, having a proper relationship between the SNR value of depth-scan OCT photocurrent and its related envelope can be useful. As, it was demonstrated in

Section 5.5, OCT systems use a demodulator to get the envelope of each single depth-scan OCT photocurrent. In this section, the relationship between SNR values at the input and output of the demodulator (envelope detector) circuit is described. This relation is determined by the detector loss factor that is a common term in communication and radar systems [89] . An electronic configuration that is usually applied to obtain the envelope of a signal is shown in Figure 5.14. In general, this is similar to the electronic configuration that is used for demodulation of AM radio signals [91].

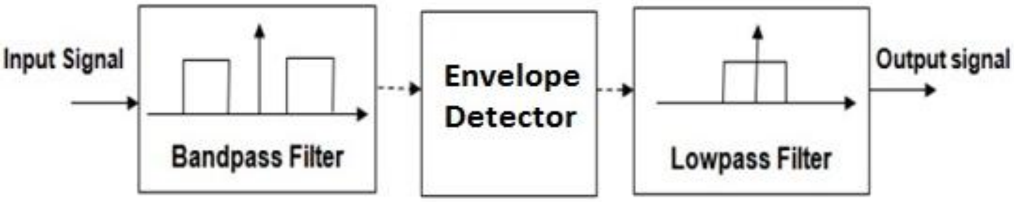

Figure 5.14: Block diagram of an envelope detector.

As shown in Figure 5.14, the envelope detector (demodulator) is preceded by a band-pass filter and is followed by a low-pass filter. When an input signal that is the sum of desired signal and noise is input to the envelope detector, there is always a loss in the SNR at the demodulator output in comparison with the SNR of demodulator input. This is called loss factor and is given by [89],

$$\gamma = \frac{\overline{m^2(t)}}{1+\overline{m^2(t)}} , \tag{5.6}$$

where, m is the AM modulation term. The proof of this relationship from reference [91] is presented in appendix A of this thesis.

Therefore, the SNR values at the input and output of an envelope detector have the following relation

$$SNR_{Env_{Ouput}} = \gamma \times\ SNR_{Env_{input}}. \tag{5.7}$$

We can see form Eq. (5.6), γ is always a positive number and is less than one, $0< \gamma < 1$. Hence, the SNR at the output of envelope detector always is a monotonically decreasing function of the SNR at the input of an envelope detector. This monotonic relationship demonstrates that if we maximize the SNR at the envelope detector input, which in our case is the SNR of the depth-scan photocurrent, then the SNR at the output of the envelope detector will also be maximized, which in our case is the SNR of the depth-scan envelope.

5.7 Empirical estimation and verification of noise statistics for photocurrent envelope

In this section, the second order statistics of depth-scan envelopes are empirically estimated. Then by using these estimates, the dependency of the estimated covariance matrix of the noise in the photocurrent envelope on the depth of imaging is verified. Similar to the depth-scan photocurrent we have

$$\hat{\boldsymbol{s}} = E_N[\boldsymbol{y}_{Env}]$$

$$\widehat{\boldsymbol{C}} = E_N[\boldsymbol{y}_{Env}\boldsymbol{y}_{Env}^{\mathrm{T}}] - E_N[\boldsymbol{y}_{Env}].E_N[\boldsymbol{y}_{Env}^{\mathrm{T}}], \tag{5.8}$$

where $\boldsymbol{y}_{Env}$ is the envelope of a single depth-scan photocurrent, $\boldsymbol{y}$**.** To investigate the variation of envelope covariance matrix with the imaging depth, three different

TD-OCT dataset are used. These datasets are from imaging vascular rabbit tissue, and a fishing line.

In the first example, the TD-OCT envelopes from vascular rabbit tissue are used to investigate the non-stationary property of a depth-scan envelope in TD-OCT. The covariance matrix of a depth-scan envelope is estimated by using Eq. (5.8) and the diagonal elements of that matrix (noise power in this envelope) are plotted in Figure 5.15(b). We note from Figure 5.15(a) and Figure 5.15(b) that the noise power in this depth-scan envelope varies with the imaging depth and has its maximum value at the depth where the peak value of the envelope occurs.

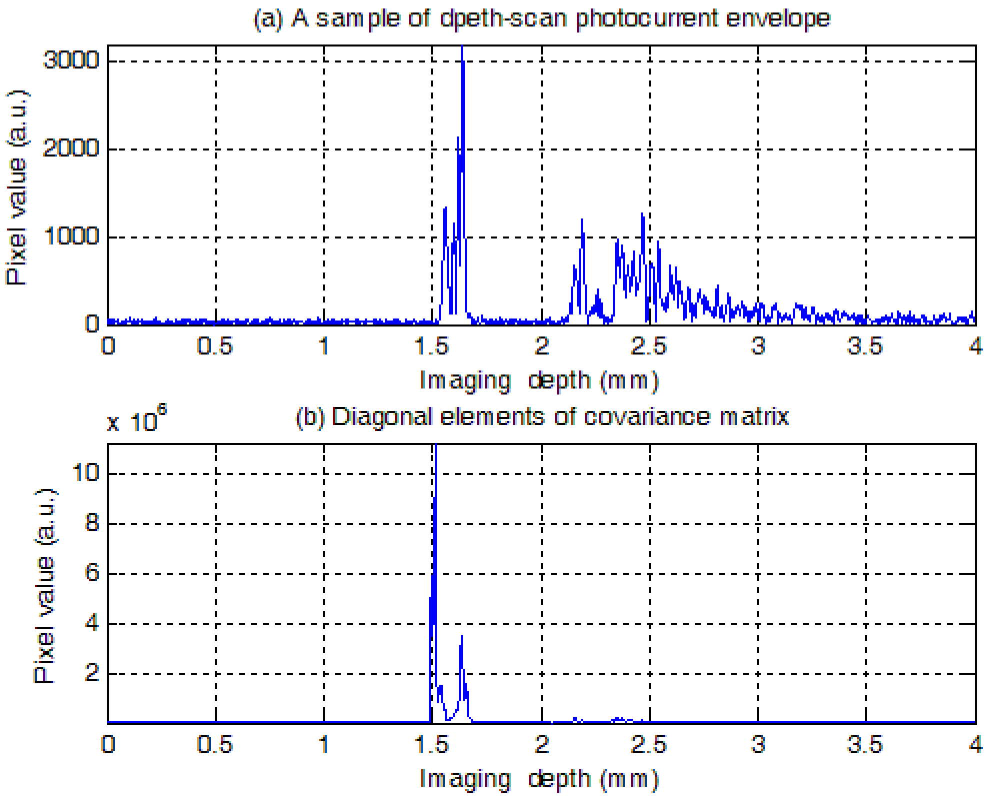

Figure 5.15: (a) A sample of depth-scan photocurrent envelope of vascular rabbit tissue, (b) diagonal elements of covariance matrix for photocurrent envelope of part (a).

In addition, to investigate the non-sattionary nature of this depth-scan envelope, its local covariance matrices are estimated using four windows of size 50 pixels (approximately equivalent to the 0.054 mm for this sample) for different ranges of imaging depth. These local estimates are shown in Figure 5.16 (a-d) and Figure 5.17(a-d). As these figures show, the patterns of these locally estimated covariance matrices are not uniform and they change with the depth of imaging. This empirically confirms the non-stationary nature of the photocurrent envelope in TD-OCT.

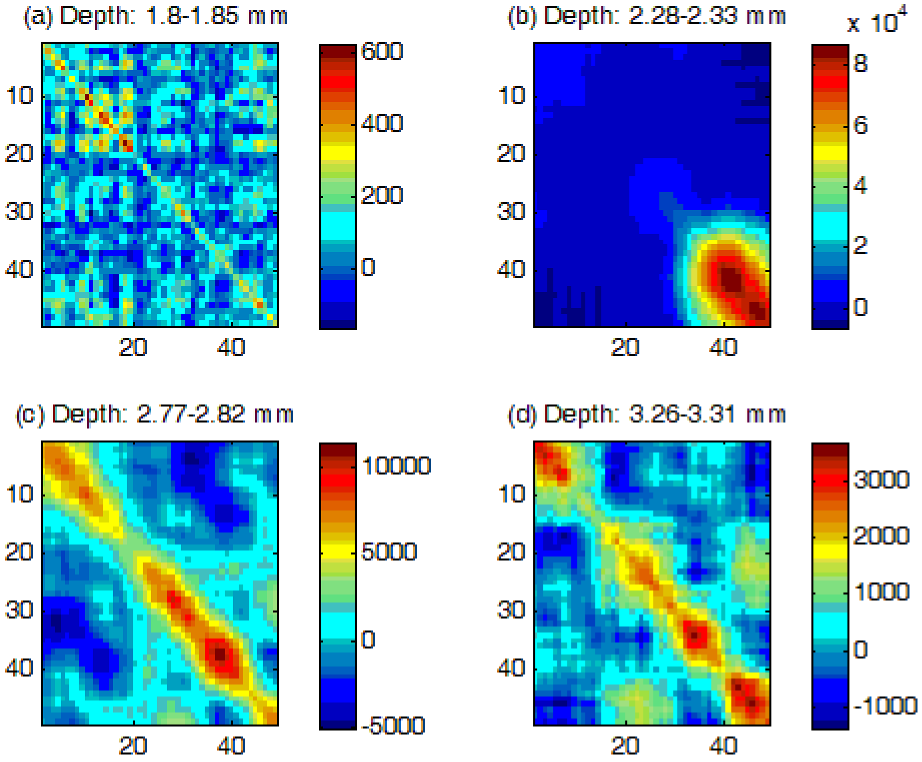

Figure 5.16: Estimates of local covariance matrix of a depth-scan envelope of vascular rabbit tissue at different ranges of imaging depth.

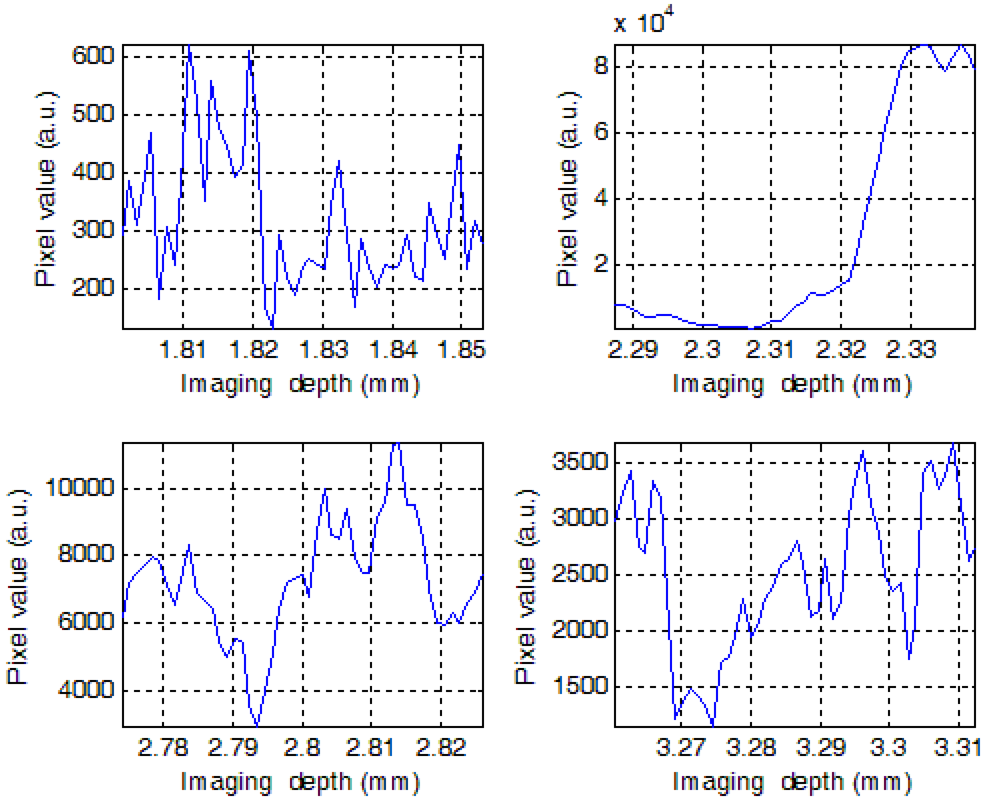

Figure 5.17: Diagonal elements of covariance matrix of a depth-scan envelope of vascular rabbit tissue at different ranges of imaging depth.

Another data set that is used to investigate the non-stationary property of depth-scan photocurrent envelope in TD-OCT is an image of a fishing line that is taken along the length of fishing-line. Figure 5.18(a) shows a depth-scan photocurrent envelope from this OCT data set. The covariance function of this envelope is estimated using Eq. (5.8) and its diagonal elements are plotted in part (b) of this Figure 5.18(b). We observe that these diagonal elements (noise power in envelope) vary with the depth of OCT imaging.

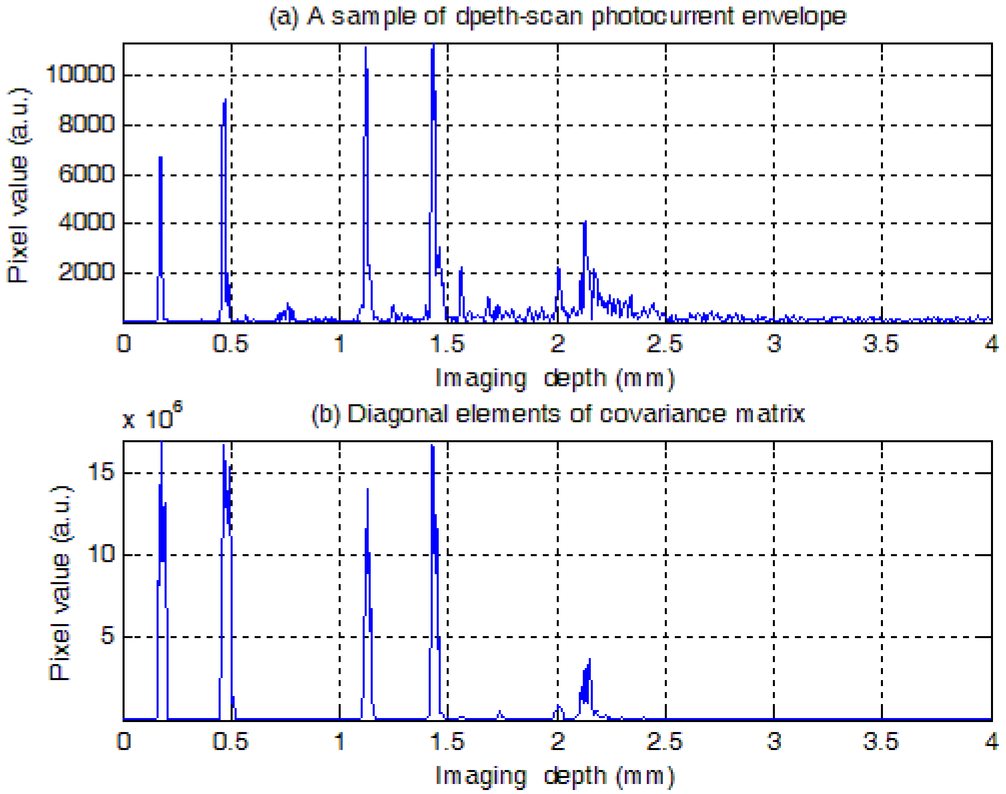

Figure 5.18: (a) A sample of depth-scan photocurrent of a fishing-line imaged along its length, (b) diagonal elements of the covariance matrix of the photocurrent envelope of part (a).

In this example, we also considered four 100 pixel wide windows, equivalent to 0.1 mm, to estimate local covariance matrices of the noise in the depth-scan envelope at different ranges if imaging depth. The estimates are shown in Figure 5.19(a-d) and Figure 5.20(a-d). We observe that the patterns of these local covariance matrices are not uniform and clearly change with the depth of OCT imaging. This confirms the non-stationary nature of the depth-scan envelope of this fishing line sample.

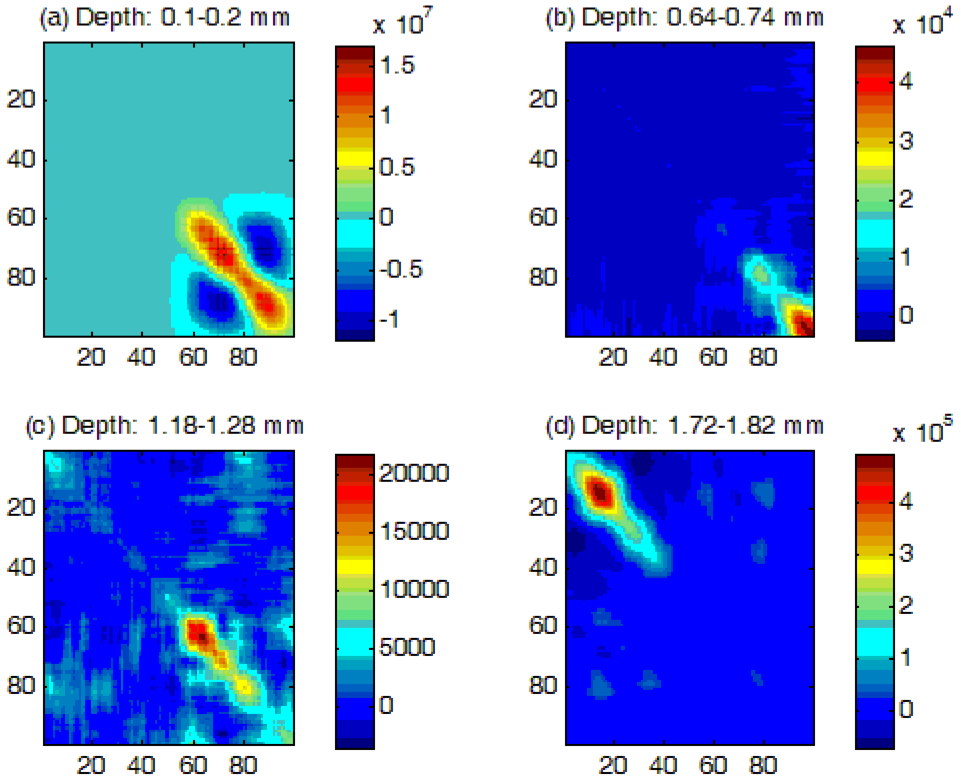

Figure 5.19: Estimates of local covariance matrices of a depth-scan envelope of a fishing line imaged along its length direction and for different ranges of imaging depth.

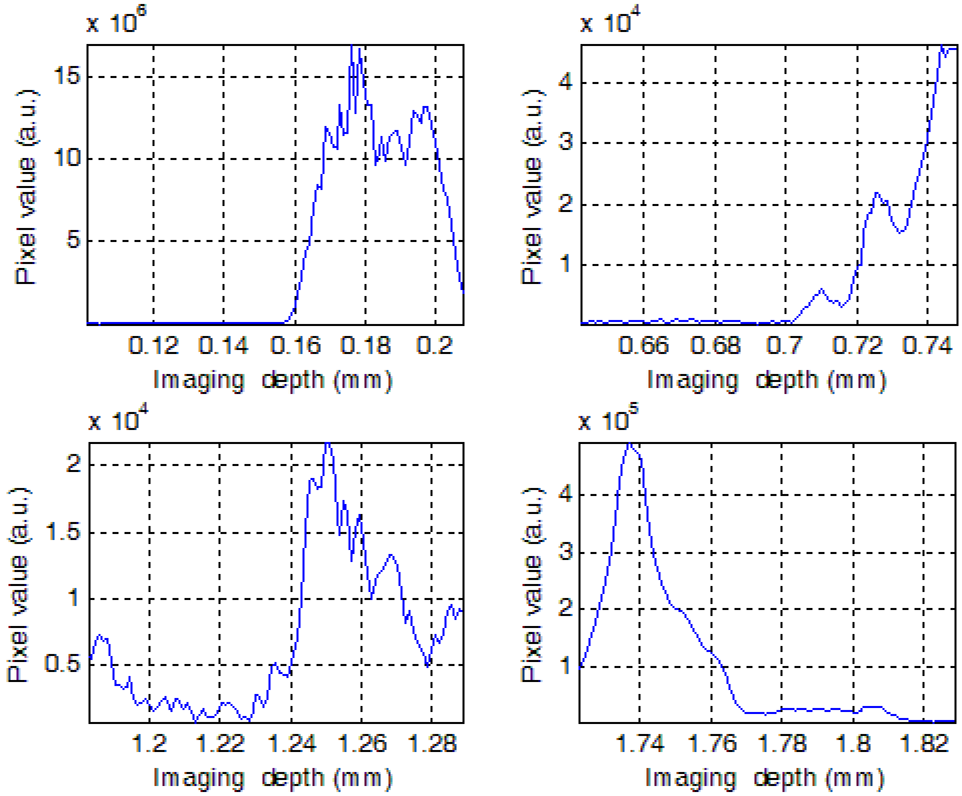

Figure 5.20: Diagonal elements of covariance matrix of a depth-scan envelope of a fishing line imaged along its length direction at different ranges of imaging.

The last data set that is used to investigate the non-stationary nature of a depth-scan photocurrent envelope in TD-OCT is an image of a fishing line that is taken along the width of fishing-line. Figure 5.21(a) shows a depth-scan photocurrent envelope from this data set. Also, the diagonal elements of the estimated covariance matrix (noise power in this depth-scan photocurrent envelope) are plotted in part (b) of this Figure 5.21. We observe that these diagonal elements are changing with imaging depth.

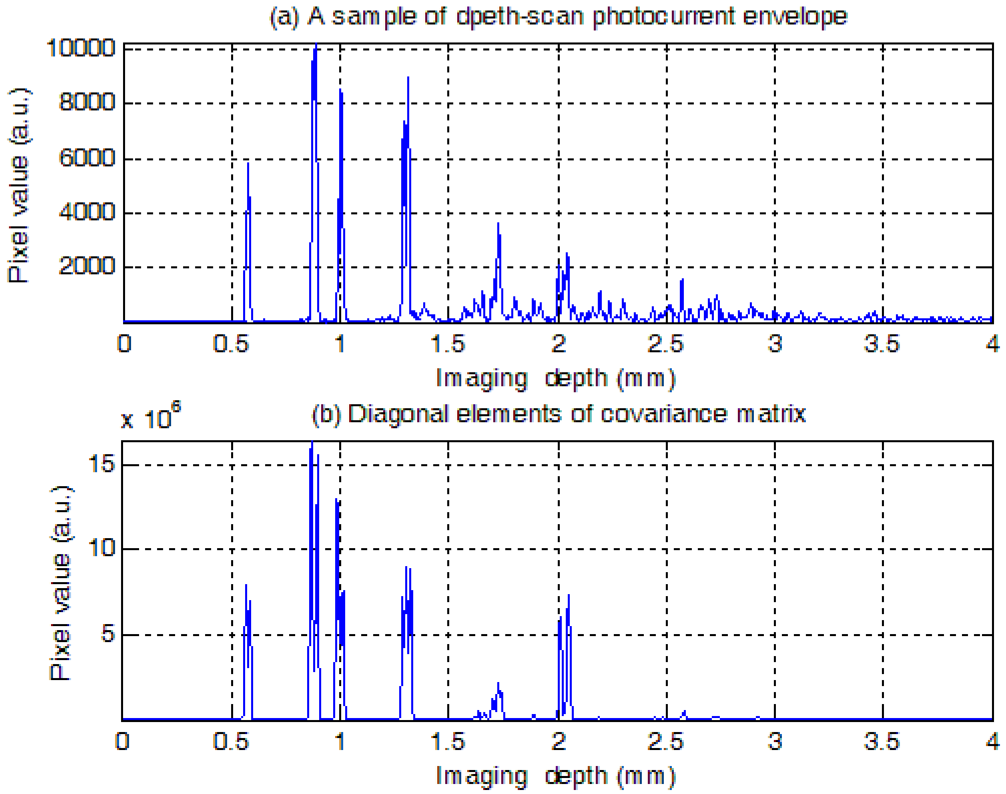

Figure 5.21: A sample of depth-scan photocurrent envelope of a fishing-line imaged along its width direction, (b) diagonal elements of covariance matrix of photocurrent envelope of part (a).

In addition, four windows of size 300 pixels (approximately equivalent to the 0.32 mm) are considered to estimate the local covariance matrices of the noise in this depth-scan envelope at different depths of OCT imaging. These estimates are shown in Figure 5.22(a-d) and Figure 5.23(a-d). The variation of these covariance matrices with depth of imaging is obvious from these figures.

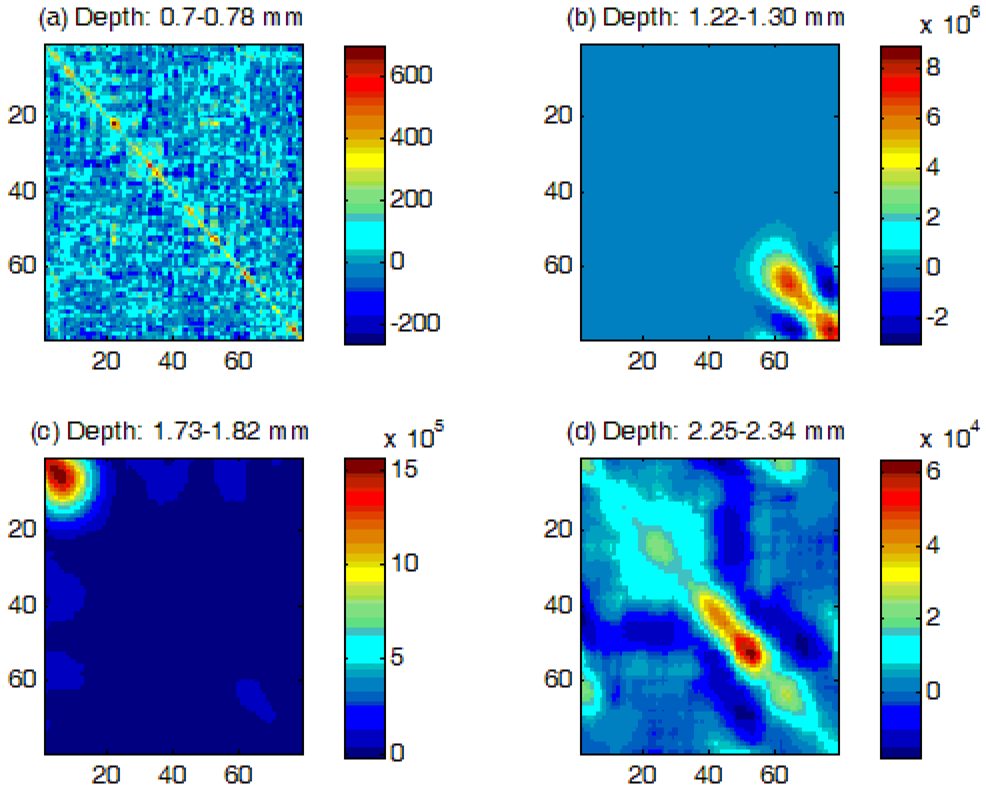

Figure 5.22: Estimates of local covariance matrices of a depth-scan envelope of a fishing line imaged along its width direction and for different ranges of imaging depth.

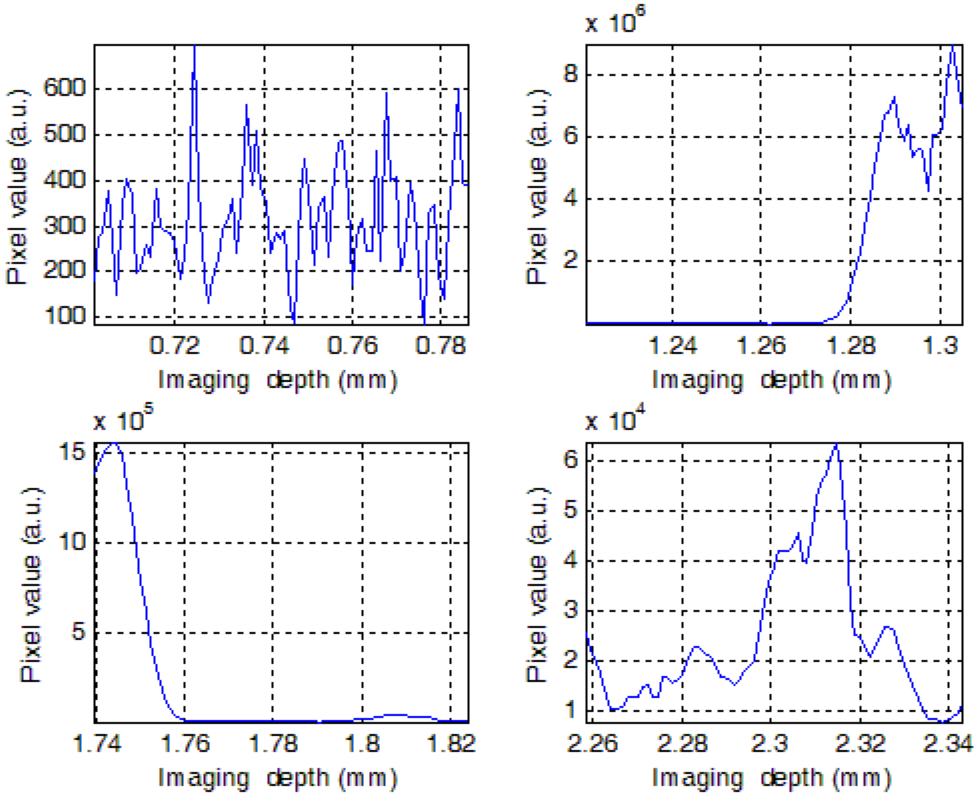

Figure 5.23: Diagonal elements of covariance matrix of a fishing line imaged along its width direction at different ranges of imaging depth.

In conclusion, our results from this Chapter confirm that the covariance matrix of a depth-scan photocurrent envelope in a TD-OCT system is depth-dependent and it changes with the value of the photocurrent envelope. Therefore in TD-OCT systems the depth-scan photocurrent envelopes are non-stationary signals and our approach of using a depth-dependent matched filter to increase the SNR of these signals (Chapter 7) is justified.

Chapter 6

Depth-Dependent Matched Filter

In Chapter 5 of this thesis, we empirically estimated the covariance matrix of the noise in a single depth-scan photocurrent and its corresponding envelope in TD-OCT. We also demonstrated its dependence on the value of the photocurrent and its envelope in different depths of imaging. This depth dependent variation of covariance function confirms the non-stationary nature of the OCT photocurrent and its envelope. Hence, using deterministic signal processing methods is not optimum for image and signal processing of TD-OCT. On the other hand applying statistical image processing methods that consider the statistical properties of OCT depth-scans could be very useful and would result in better performance compared to that of deterministic methods.

In this Chapter, we propose and design a statistical depth-dependent matched filter to maximize the depth of OCT imaging in the TD-OCT systems. This filter applies empirically estimated second order statistics of depth-scan photocurrent or corresponding envelope to maximize the SNR of these signals at the filter output. Also, this filter increases the Contrast-to-Noise Ratio (CNR) of OCT images at its output.

This Chapter begins with an explanation of the theory of matched filters in Section 6.1. Since depth-scan photocurrents and corresponding envelopes are non-stationary signals in TD-OCT, in Section 6.2, we modify the response function of the typical matched filter of Section 6.1 to consider the non-stationary nature of these signals. The result of this modification is our depth-dependent matched filter. As explained in Section 5.6, there is a monotonic relationship between the value of SNR of a depth-scan photocurrent and its corresponding envelope. Hence, we can apply our proposed depth-dependent matched filter of Section 6.2 on the envelopes of depth-scan photocurrents to maximize the SNR at its output. To evaluate the performance of our depth-dependent matched filter, we consider values of both SNR and CNR. The results of applying our proposed depth-dependent matched-filter on TD-OCT images of vascular rabbit tissue and a human tooth are presented and discussed in Section 6.4.

6.1 Theory of matched filter

Matched filters are typically used to detect a known signal that is embedded in noise [90]. Theoretically a matched filter, among all linear filters, maximizes the value of SNR at its output [90]. This filter has a wide range of applications in communications, radar, and biomedical engineering [91],[90]. The impulse response of a matched filter is constructed based on the assumption that the shape of the input signal is known. A block diagram of a matched filter is shown in Figure 6.1

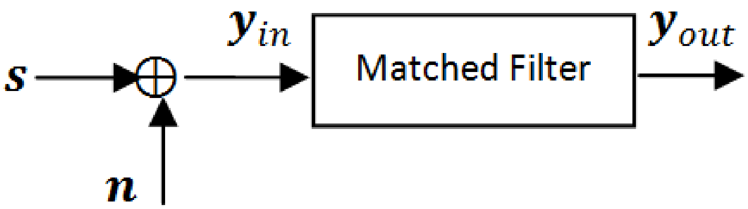

Figure 6.1: A block diagram of a matched filter.

In the following section, we derive the impulse response of the matched filter shown in Figure 6.1. We assume a signal vector $\boldsymbol{y}_{in}$ at the input of matched filter given by a linear model of,

$$\boldsymbol{y}_{in} = \boldsymbol{s} + \boldsymbol{n}, \tag{6.1}$$

where, this equation is the sum of the desired signal vector $\boldsymbol{s}$ and the noise term $\boldsymbol{n}.$ In this equation, noise has zero mean and covariance function of,

$$\boldsymbol{C} = E\left[\boldsymbol{y}_{in}\boldsymbol{y}_{in}^{\mathrm{T}}\right] - E[\boldsymbol{y}_{in}].E\left[\boldsymbol{y}_{\mathrm{in}}^{\mathrm{T}}\right], \tag{6.2}$$

where $E[\cdot]$ denotes the statistical mean and $E[\cdot\,\cdot^{T}]$ denotes the autocorrelation function of assumed signal $(\cdot)$, also $(\cdot)^{T}$ represents the transpose operation. In general the relationship of input and output of the matched filter can be considered as a convolution of the input signal, $\boldsymbol{y}_{in}$, and the impulse response of the matched filter, $\boldsymbol{h}$, that is denoted by,

$$\boldsymbol{y}_{out}[n] = \sum_{k=-\infty}^{\infty} \boldsymbol{h}[n-k]\boldsymbol{y}_{in}[k]. \tag{6.3}$$

In vector form, we can write the convolution of Eq. (6.3) in terms of an inner product between the input vector of the filter, $\boldsymbol{y}_{in}$, and the impulse response vector of filter, $\boldsymbol{h},$ as denoted by,

$$\boldsymbol{y}_{out} = \boldsymbol{h}^{H}\boldsymbol{y}_{in} = \boldsymbol{h}^{H}\boldsymbol{s} + \boldsymbol{h}^{H}\boldsymbol{n}. \tag{6.4}$$

We seek a linear filter with the impulse response, $\boldsymbol{h}$, that maximizes the SNR of the output $\boldsymbol{y}_{out}$, where the output signal is the inner product of the filter impulse response $\boldsymbol{h}$ and the input signal $\boldsymbol{y}_{in}$ as denoted by Eq. (6.4). To obtain this impulse response, the SNR is defined as an objective function in the form of,

$$SNR = \frac{|\boldsymbol{y_s}|^2}{E\{|\boldsymbol{y_n}|^2\}} = \frac{|\boldsymbol{h}^H\boldsymbol{s}|^2}{E\{|\boldsymbol{h}^H\boldsymbol{n}|^2\}}. \tag{6.5}$$

This relation defines the ratio of the output power due to the desired signal $\boldsymbol{s}$ which is denoted $|\boldsymbol{y_s}|^2$ to the power of the output due to the noise term $\boldsymbol{n}$ which is denoted $E\{|\boldsymbol{y_n}|^2\}$. Expanding the expressions in the nominator and denominator of Eq. (6.5), we obtain,

$$|\boldsymbol{h}^H\boldsymbol{s}|^2 = \boldsymbol{h}^H\boldsymbol{s}\boldsymbol{s}^H\boldsymbol{h}$$

$$E\{|\boldsymbol{h}^H\boldsymbol{n}|^2\} = \mathrm{E}\{(\boldsymbol{h}^H\boldsymbol{n})(\boldsymbol{h}^H\boldsymbol{n})^H\} = \boldsymbol{h}^H E\{\boldsymbol{n}\boldsymbol{n}^H\}\boldsymbol{h} = \boldsymbol{h}^H\boldsymbol{C}\boldsymbol{h}. \tag{6.6}$$

where $\boldsymbol{C} = E\{\boldsymbol{n}\boldsymbol{n}^H\}$ is the covariance matrix of noise. Using these relations, the SNR function becomes,

$$SNR = \frac{|\boldsymbol{h}^H\boldsymbol{s}|^2}{\boldsymbol{h}^H\boldsymbol{C}\boldsymbol{h}}. \tag{6.7}$$

To determine the impulse response of matched filter, $\boldsymbol{h}$, such that it maximizes the SNR of filter output, $\boldsymbol{y}_{out}$, we maximize $|\boldsymbol{h}^H\boldsymbol{s}|^2 = \boldsymbol{h}^H\boldsymbol{s}\boldsymbol{s}^H\boldsymbol{h}$ term subject to the constraint of $\boldsymbol{h}^H\boldsymbol{C}\boldsymbol{h} = 1$. For this purpose, we formulate the problem using a Lagrange multiplier of,

$$\mathcal{L}(\boldsymbol{h}, \lambda) = \boldsymbol{h}^H\boldsymbol{s}\boldsymbol{s}^H\boldsymbol{h} + \lambda(1 - \boldsymbol{h}^H\boldsymbol{C}\boldsymbol{h}) = 0. \tag{6.8}$$

To maximize this expression, we obtain the gradient of $\mathcal{L}(\boldsymbol{h}, \lambda)$ and set it to zero,

$$\nabla_{h^*}[\mathcal{L}(\boldsymbol{h}, \lambda)] = 2\boldsymbol{s}\boldsymbol{s}^H\boldsymbol{h} - 2\lambda\boldsymbol{C}\boldsymbol{h} = 0 \Longrightarrow$$

$$\boldsymbol{s}\boldsymbol{s}^H\boldsymbol{h} = \lambda\boldsymbol{C}\boldsymbol{h}, \tag{6.9}$$

to find the filter response $\boldsymbol{h}$. By manipulating in Eq. (6.9), we recognize that it an eigen-value problem that can be written as

$$\boldsymbol{h}^H(\boldsymbol{s}\boldsymbol{s}^H)\boldsymbol{h} = \lambda\ \boldsymbol{h}^H\boldsymbol{C}\boldsymbol{h}\,, \tag{6.10}$$

where, λ denoted the eigen-values [92]. As $\boldsymbol{s}\boldsymbol{s}^H$ is of unit rank, it has only one nonzero eigen-value given by,

$$\lambda = \boldsymbol{s}^H\boldsymbol{C}^{-1}\boldsymbol{s}\,, \tag{6.11}$$

where, C^{-1} is the inverse of covariance matrix of the noise. The eigen-vector corresponding to the eigen-value λ is our required matched filter,

$$\boldsymbol{h} = \frac{1}{\sqrt{\boldsymbol{s}^H\boldsymbol{C}^{-1}\boldsymbol{s}}}\boldsymbol{C}^{-1}\boldsymbol{s}. \tag{6.12}$$

We can geometrically interpret this filter as an example of Principal Component Analysis (PCA), where by projecting a depth-scan signal on a principle direction, given by $\boldsymbol{h}$, the maximum value of SNR at the output of matched filter is obtained.

6.2 Depth-dependent matched filter for single depth-scan envelope

In Chapter 5, it was demonstrated and verified that each depth-scan envelope could be modeled as a non-stationary random process $\hat{\boldsymbol{y}}_{in}$ which is the sum of the estimate of the ensemble average, $\hat{\boldsymbol{s}},$ given by,

$$\hat{\boldsymbol{s}} = E_N[\boldsymbol{y}_{Env}] \tag{6.13}$$

and a non-stationary noise process, n, with zero mean and estimated covariance function,

$$\widehat{\boldsymbol{C}} = E_N[\boldsymbol{y}_{Env}\boldsymbol{y}_{Env}^{\mathrm{T}}] - E_N[\boldsymbol{y}_{Env}].E_N[\boldsymbol{y}_{Env}^{\mathrm{T}}]. \tag{6.14}$$

where $\boldsymbol{y}_{Env}$ represents one depth-scan photocurrent-envelope obtained by Eq. (5.5). Therefore each depth-scan envelope,$\hat{\boldsymbol{y}}_{in}$, in TD-OCT can be modeled as,

$$\hat{y}_{in} = \hat{\boldsymbol{s}} + \boldsymbol{n} = E_N[\boldsymbol{y}_{Env}] + \boldsymbol{n}. \tag{6.15}$$

One important issue in the post-preprocessing stage of all types of OCT systems is to design a suitable filter with the aim of increasing the SNR of the depth-scan envelope at the filter output. In the previous section, the impulse response of an ideal matched filter that maximizes the SNR of input signal at its output (Eq. (6.12)) was derived. In addition, in Chapter 5, the local covariance matrices of depth-scan photocurrent and its envelope were empirically estimated. These estimates were calculated by considering the OCT photocurrent or its envelope in specific windows representing different depths of imaging. Using these local estimates, it was verified that the covariance of the depth-scan photocurrent and its envelope varies with OCT imaging depth. Hence, it is essential to implement the matched filter of Section 6.1 (Eq. (6.12)) using local statistics of the depth-scan photocurrent or envelope. To account for the depth-dependent noise, we design the depth-dependent matched filters $\widehat{\boldsymbol{h}}_w$ using a sliding window of width w pixels. In the calculation process, each time, this window is centered at pixel *m* and the inner product is evaluated over the interval k which is defined by,

$$k = [m - \lceil w/2 \rceil \;,\; m + \lceil w/2 \rceil], \tag{6.16}$$

where $\lceil \cdot \rceil$ denotes the ceiling function. Hence, the output of depth-dependent matched filter is given by,

$$\widehat{\boldsymbol{h}}_w^H \boldsymbol{y}_w = \widehat{\boldsymbol{h}}_w^H \widehat{\boldsymbol{s}}_w + \widehat{\boldsymbol{h}}_w^H \boldsymbol{n}_w. \tag{6.17}$$

Therefore for every window, *w*, the impulse response of the matched filter, $\widehat{\boldsymbol{h}}_w$, is given by,

$$\widehat{\boldsymbol{h}}_w = \frac{1}{\sqrt{\widehat{\boldsymbol{s}}_w^H \widehat{\boldsymbol{C}}_w^{-1} \widehat{\boldsymbol{s}}_w}} \widehat{\boldsymbol{C}}_w^{-1} \widehat{\boldsymbol{s}}_w \,, \tag{6.18}$$

where $\widehat{\boldsymbol{C}}_w^{-1}$ is the inverse of estimated noise covariance matrix in a sliding window with size w. We observe that the filter $\widehat{\boldsymbol{h}}_w$ is updated depending on the varying noise covariance matrix $\widehat{\boldsymbol{C}}_w^{-1}$. We slide the window over the whole length of depth-scan envelope one pixel at a time, such that the SNR is maximized for each pixel.

To improve the numerical implementation of our filter, we set all pixels with intensity less than 1% of the maximum value of depth-scan envelope intensity to zero. In practice, before obtaining the filter $\widehat{\boldsymbol{h}}_w$, we need to modify the estimated covariance matrices, $\widehat{\boldsymbol{C}}_w$. Since the locally estimated covariance matrices, $\widehat{\boldsymbol{C}}_w$, are not always semi-positive-definite (it means they could have negative eigen-values), we need a modification method [93] to convert them to semi-positive definite matrices, $\widehat{\boldsymbol{C}'}_w$.This is done by applying the eigen-decomposition method (using the Eig function in MATLAB) on each locally estimated covariance matrix, $\widehat{\boldsymbol{C}}_w$, given by,

$$[\boldsymbol{Q}\ \boldsymbol{D}] = Eig(\widehat{\boldsymbol{C}}_w)\ , \tag{6.19}$$

where $\boldsymbol{Q}$ represents the matrix of eigen-vectors and the diagonal elements of matrix $\boldsymbol{D}$ represent the eigen-values of $\widehat{\boldsymbol{C}}_w$. To convert the covariance matrix, $\widehat{\boldsymbol{C}}_w$ to a semi-positive-definite matrix, all elements of matrix $\boldsymbol{D}$ are replaced by their absolute values as denoted by,

$$\boldsymbol{D}_1 = abs(\boldsymbol{D}), \tag{6.20}$$

and the modified estimated covariance matrix, $\widehat{\boldsymbol{C}'}_w$, is constructed using [93],

$$\widehat{\boldsymbol{C}'}_w = \boldsymbol{Q}\boldsymbol{D}_{\boldsymbol{1}}\boldsymbol{Q}'. \tag{6.21}$$

In addition, to obtain the impulse response of our matched filter, $\widehat{\boldsymbol{h}}_w$, we need to obtain the inverse of modified estimated noise covariance matrices, $\widehat{\boldsymbol{C}'}_w^{-1}$. In the case when the modified estimated noise covariance matrix, $\widehat{\boldsymbol{C}'}_w$, is not full rank, $\widehat{\boldsymbol{C}'}_w^{-1}$ would not exist. In this case, we replace the modified estimated covariance matrix, $\widehat{\boldsymbol{C}'}_w^{-1}$, with the identity matrix and obtain the filter $\widehat{\boldsymbol{h}}_w$ using,

$$\widehat{\boldsymbol{h}}_w = \frac{I^{-1}\hat{\boldsymbol{s}}_w}{\sqrt{\hat{\boldsymbol{s}}_w^H I^{-1}\hat{\boldsymbol{s}}_w}}\,, \tag{6.22}$$

where I^{-1} is the inverse of the identity matrix I.

Due to the application of our depth-dependent matched filter on an OCT image (depth-scan envelopes), a difference in scale usually occurs between the filtered OCT image, Im_f, and the original OCT image, Im_o, before filtering. To ensure that the filtered and original image have the same range of intensity values, we scale the original image using a scaling factor (scl). This scaling factor is defined as the ratio of the maximum value of filtered image to the maximum value of original image,

$$scl = \frac{max(Im_f)}{max(Im_o)}. \tag{6.23}$$

The scaled original image, Im_{o_scl} is obtained using,

$$Im_{o\_scl} = Im_o * scl. \tag{6.24}$$

6.3 SNR analysis method and CNR calculation

The performance of our proposed depth-dependent matched filter is quantitatively evaluated by examining the SNR and CNR values at its output. The SNR at the input of the filter is calculated using,

$$SNR_{dB}[m] = 10.\log_{10}\frac{\left|\widehat{\boldsymbol{S}}[m]\right|^2}{[\widehat{\boldsymbol{C}}]_{mm}}, \tag{6.25}$$

where $\left|\widehat{\boldsymbol{S}}[m]\right|^2$, represents the power of estimated ensemble average of the depth-scan envelope,$\boldsymbol{y}_{Env}$, at a specific pixel m, and $[\widehat{\boldsymbol{C}}]_{mm}$ are the diagonal elements of the estimated noise covariance matrix, $\widehat{\boldsymbol{C}}$, that represent the power of the noise. In addition, the SNR at the output of the filter is calculated using,

$$SNR_{dB}[m] = 10.\log_{10}\frac{|\boldsymbol{y}_{out}[m]|^2}{[\widehat{\boldsymbol{C}}]_{mm}}, \tag{6.26}$$

where $|\boldsymbol{y}_{out}[m]|^2$ represents the power of the output of our filter, $\boldsymbol{y}_{out}$**,** at a specific pixel m, and $[\widehat{\boldsymbol{C}}]_{mm}$ are the diagonal elements of the estimated noise covariance matrix, $\widehat{\boldsymbol{C}}$, of the noise in the output of the filter. To obtain the contrast at each pixel of the ensemble average depth-scan envelope, we obtained the variance, $\sigma^2_{w'}[m]$, of the pixels inside a sliding window, w', of size 3 pixels that is shifted one pixel at a time. The variance of the averaged depth-scan envelope at a specific pixel m, is calculated using,

$$\sigma^2_{w'}[m] = E[\widehat{\boldsymbol{S}}_{w'}{}^{\boldsymbol{2}}] - (E[\widehat{\boldsymbol{S}}_{w'}])^2, \tag{6.27}$$

where, $\widehat{\boldsymbol{S}}_{w'}$ represents the values of $\widehat{\boldsymbol{S}}$ inside the windows w'. The variance of a filtered depth-scan envelope at a specific pixel m, is calculated using,

$$\sigma'^2_{\boldsymbol{w}'}[m] = E[\boldsymbol{y}_{out_{w'}}{}^{\boldsymbol{2}}] - (E[\boldsymbol{y}_{out_{w'}}])^2, \tag{6.28}$$

where $\boldsymbol{y}_{out_{w'}}$, represents the values of $\boldsymbol{y}_{out}$, inside the window, w'. The CNR of the ensemble average of the depth-scan envelope at a specific pixel, m is obtained using,

$$CNR[m] = \frac{\sigma_{\boldsymbol{w}'}^2[m]}{[\widehat{\boldsymbol{C}}]_{mm}}. \tag{6.29}$$

In this equation $\sigma_{\boldsymbol{w}'}^2[m]$ is obtained by Eq. (6.27) and $[\widehat{\boldsymbol{C}}]_{mm}$ are the diagonal elements of the estimated noise covariance matrix $\widehat{\boldsymbol{C}}$ that represent the power of noise for averaged depth-scan envelope.

The CNR of a filtered depth-scan envelope is obtained using,

$$CNR'[m] = \frac{\sigma'^2_{\boldsymbol{w}'}[m]}{[\widehat{\boldsymbol{C}''}]_{mm}}. \tag{6.30}$$

In this equation $\sigma'^2_{\boldsymbol{w}'}[m]$ is obtained by Eq. (6.28) and $[\widehat{\boldsymbol{C}''}]_{mm}$ are the diagonal elements of the estimated noise covariance matrix $\widehat{\boldsymbol{C}''}$ for the filtered depth-scan envelope that represent the power of noise.

6.4 Results of applying depth-dependent matched filter on OCT images

To test the performance of our filter, we apply it to a set of TD-OCT images of vascular rabbit tissue and a human tooth. We empirically estimated the second order statistics (statistical mean and covariance matrix) of each depth-scan envelope,$\boldsymbol{y}_{Env}$, using Eq. (5.8). We note that by increasing the number of OCT depth-scan images, the empirical estimates will be more accurate. By inserting these empirical estimates in Eq. (6.18), we obtained the impulse response of our depth-dependent matched filter. We implemented it for different window sizes,w to check the effect of window size (filter length) on its performance. The window size, w, should be chosen such that the noise in the depth-scan envelope is approximately stationary , i.e., the estimated noise covariance matrix shouldn't have considerable variation in that interval. We tried different window sizes ranging from 3 pixels to 19 pixels. For each choice of window size, we compared our results to a simple averaging operation that was performed on these images.

In this section, we show the results of simple averaging method of 20 TD-OCT images of rabbit vascular tissue and compare them with results from our proposed depth-dependent matched filter (window sizes of 3-19 pixels). The ensemble average of these 20 OCT images is shown by Figure 6.2(a). We note that features of this sample are not clear in the averaged OCT image of Figure 6.2(a). Hence regular averaging is not a suitable method to increase the depth of OCT imaging. The ensemble average of an arbitrary depth-scan envelope from 20 OCT images and its noise power are shown in Figure 6.2(b) and Figure

6.2(c), respectively. From these plots, we note that, the noise power in the averaged depth-scan envelope depend on the average depth-scan envelope which varies with different depths of imaging. We also observe that the maximum value of the averaged depth-scan envelope noise power corresponds to the maximum value of the averaged depth-scan envelope. To evaluate the performance our proposed filter, we obtained both SNR value, Eq. (6.25), and CNR value, Eq. (6.27) and Eq. (6.29), for the averaged depth-scan envelope of Figure 6.2(b). These SNR and CNR values are shown in Figure 6.2(d) and Figure 6.2(f) respectively. The contrast at each pixel of averaged depth-scan envelope was calculated using Eq. (6.27) and is shown in Figure 6.2(e).

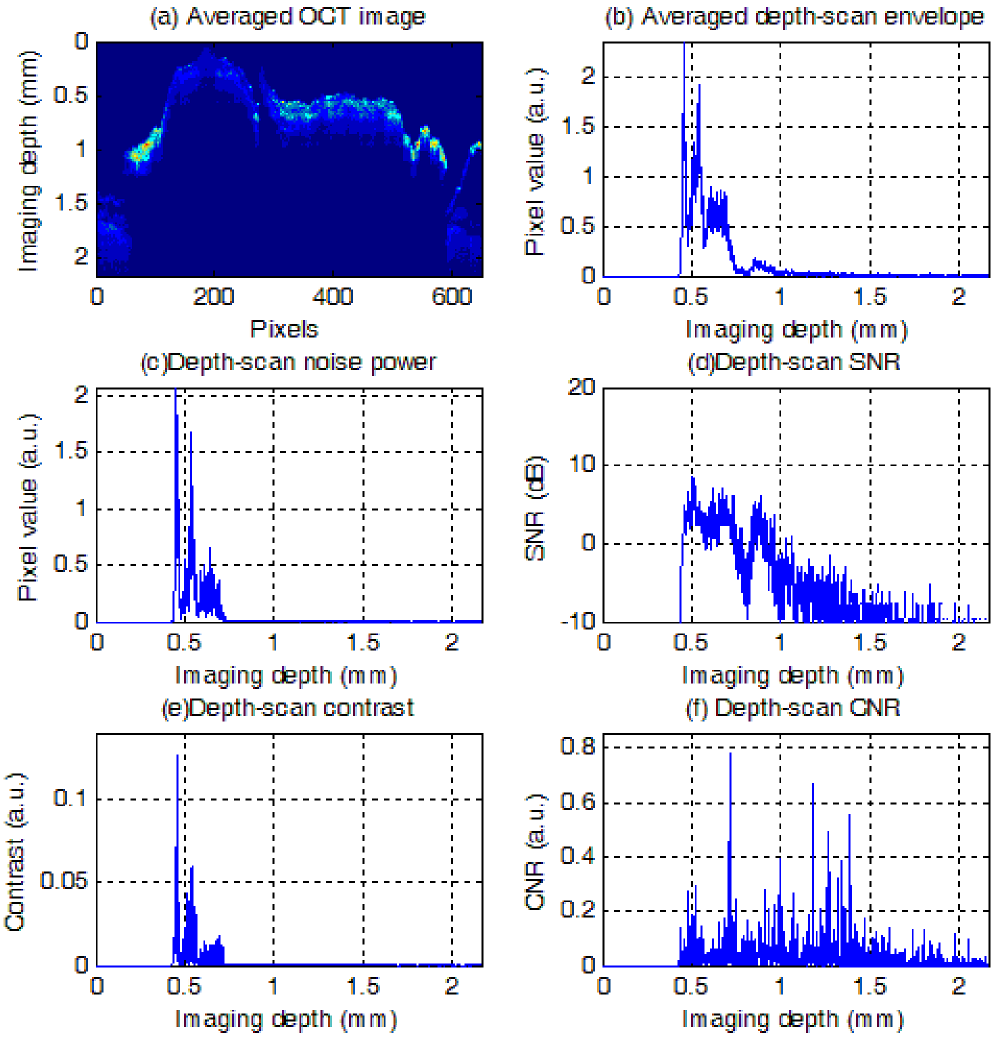

Figure 6.2: (a) Averaged OCT image; (b) averaged depth-scan envelope of vascular rabbit tissue; (c) noise power; (d) SNR; (e) contrast;(f) CNR values of averaged depth-scan envelope of part (b).

The results of applying our depth-dependent matched filter with different window sizes ranging from 3 pixels to 19 pixels are shown in Figures 6.3(a-f)-6.11(a-f).

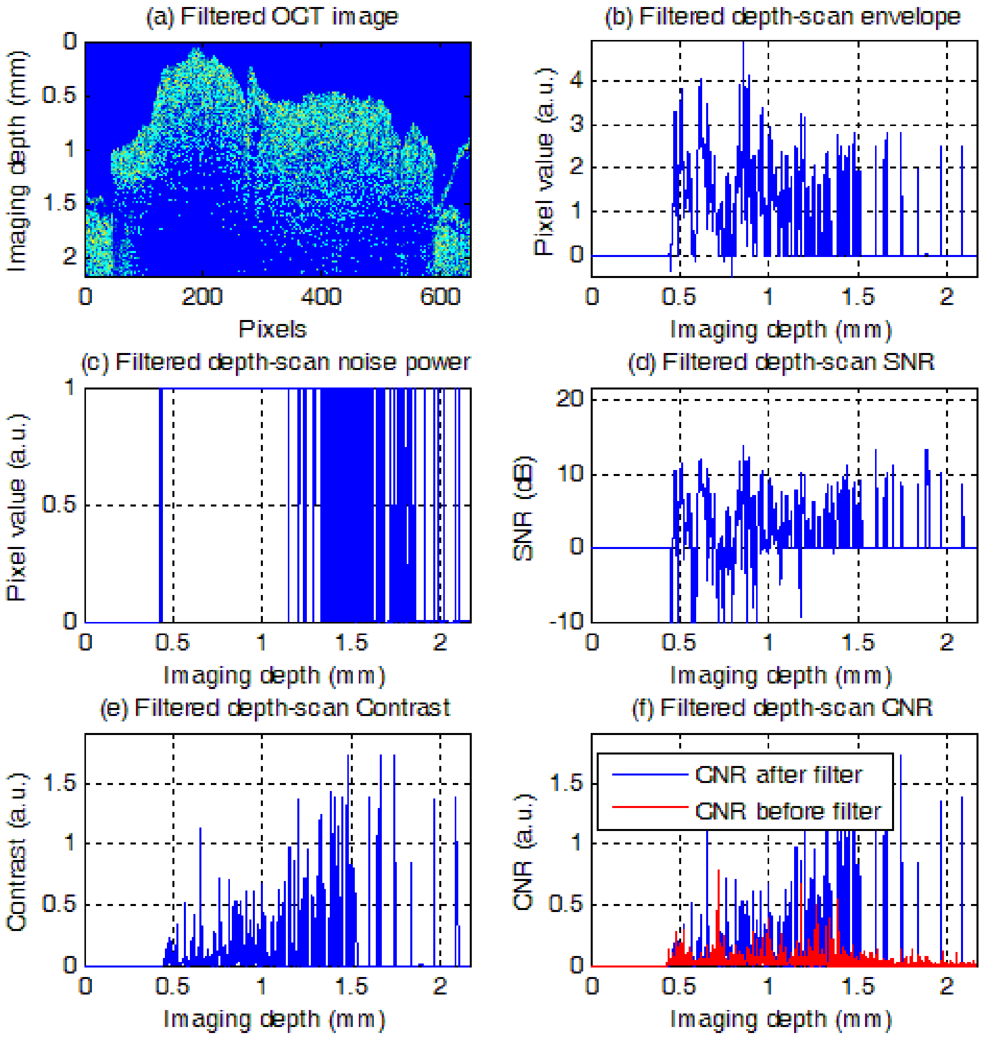

Figure 6.3: (a) Filtered OCT image; (b) filtered depth-scan envelope of vascular rabbit tissue (window size 3 pixels); (c) noise power; (d) SNR; (e) contrast; (f) CNR values of filtered depth-scan envelope of part (b).

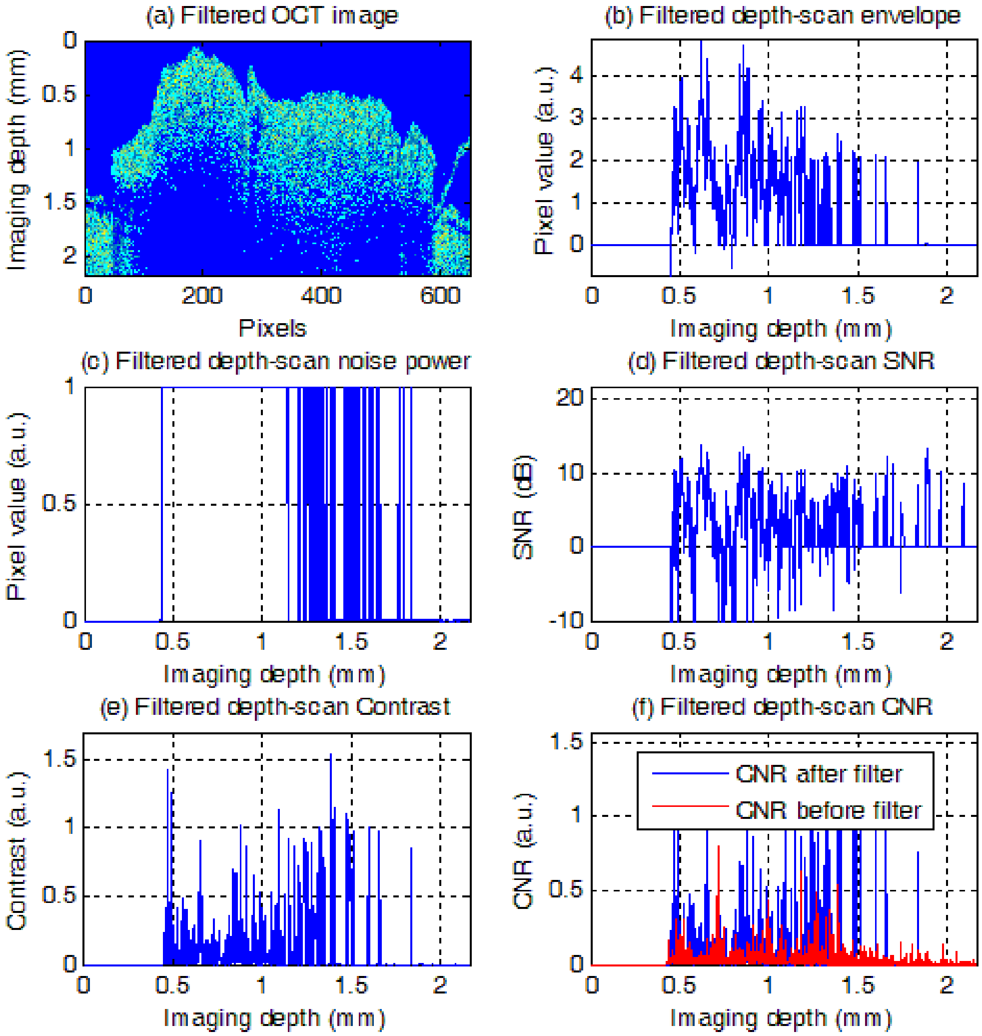

Figure 6.4: (a) Filtered OCT image; (b) filtered depth-scan envelope of vascular rabbit tissue (window size 5 pixels); (c) noise power; (d) SNR; (e) contrast; (f) CNR values of filtered depth-scan envelope of part (b).

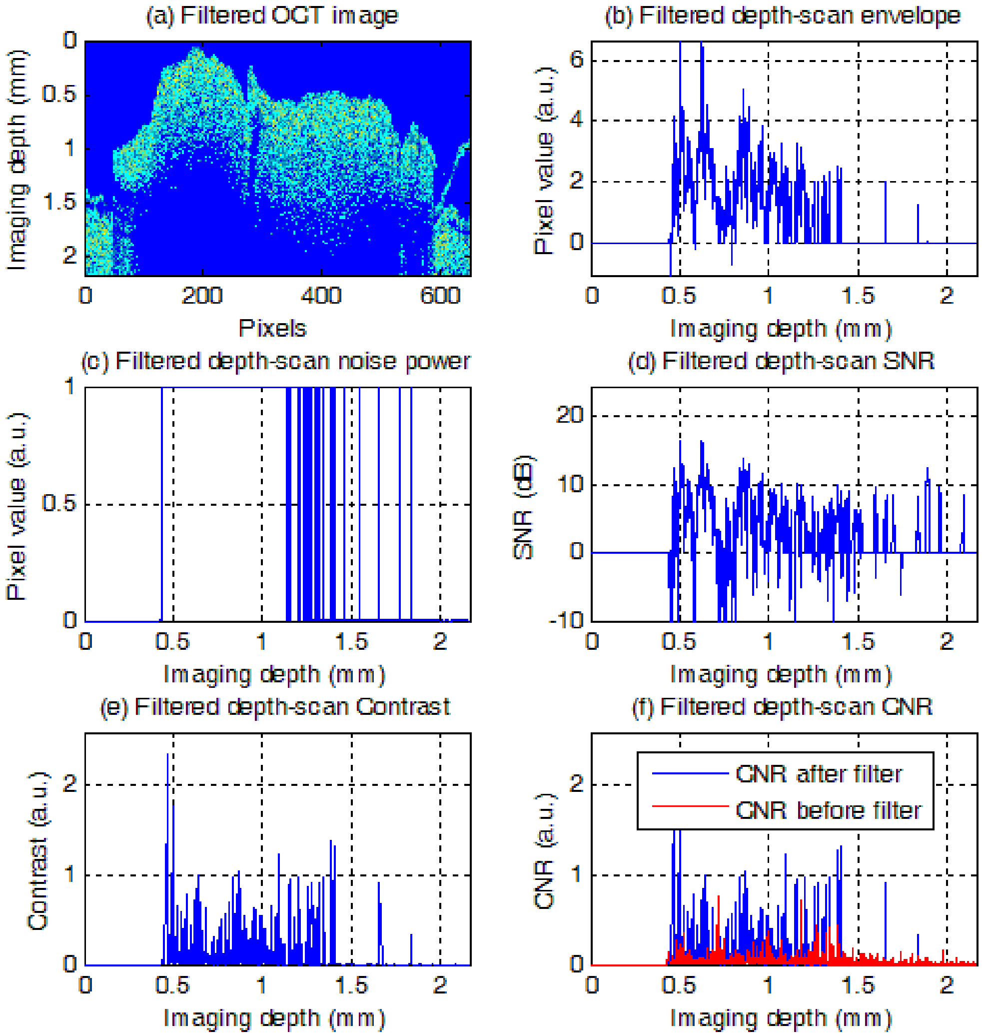

Figure 6.5: (a) Filtered OCT image; (b) filtered depth-scan envelope of vascular rabbit tissue (window size 7 pixels); (c) noise power; (d) SNR; (e) contrast; (f) CNR values of filtered depth-scan envelope of part (b).

.

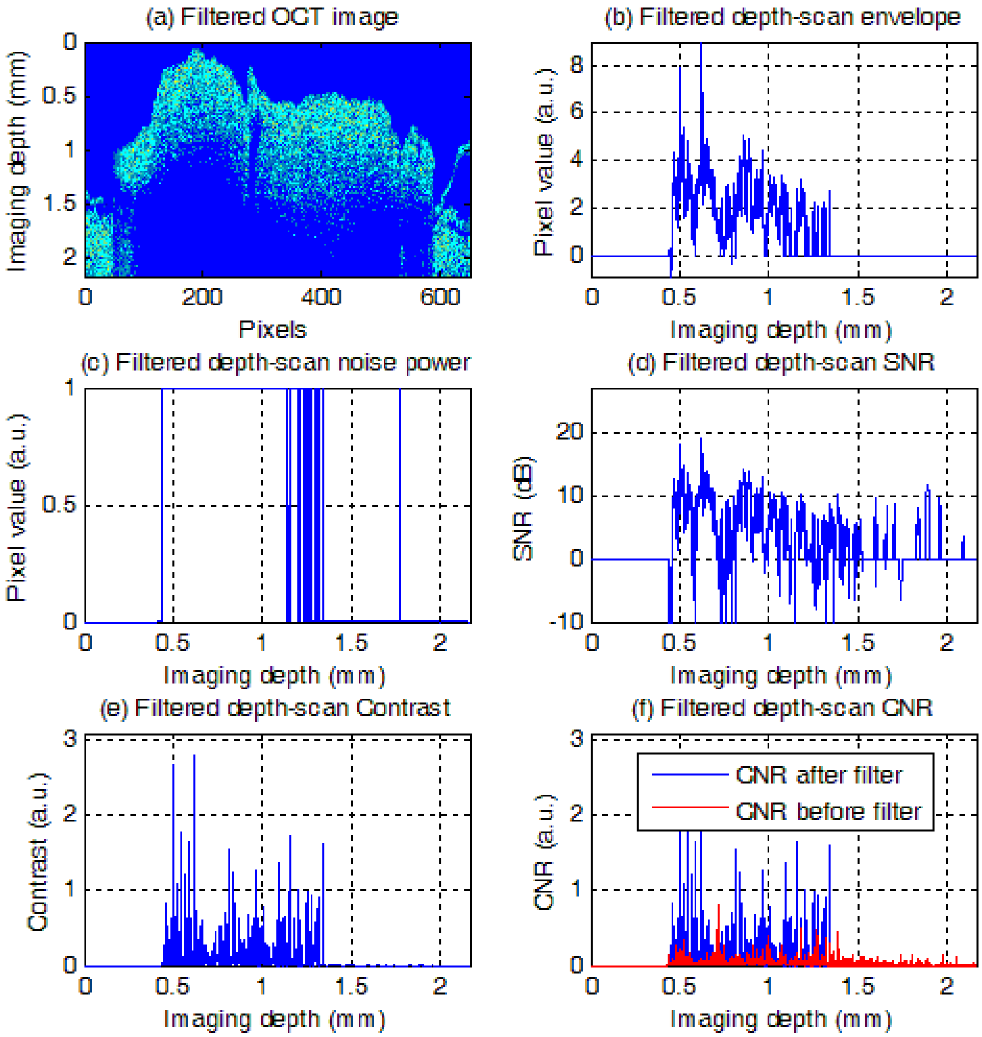

Figure 6.6: (a) Filtered OCT image; (b) filtered depth-scan envelope of vascular rabbit tissue (window size 9 pixels); (c) noise power; (d) SNR; (e) contrast; (f) CNR values of filtered depth-scan envelope of part (b).

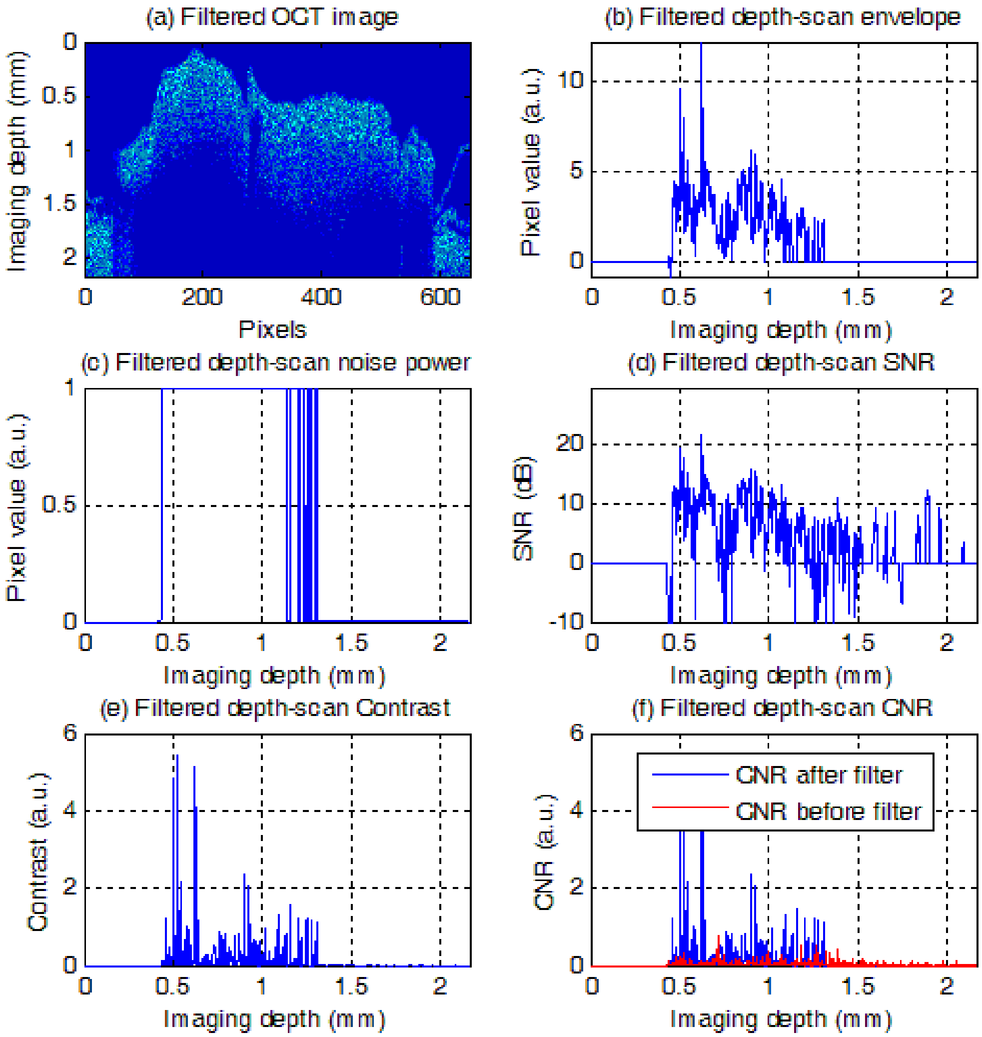

Figure 6.7: (a) Filtered OCT image; (b) filtered depth-scan envelope of vascular rabbit tissue (window size 11 pixels); (c) noise power; (d) SNR; (e) contrast; (f) CNR values of filtered depth-scan envelope of part (b).

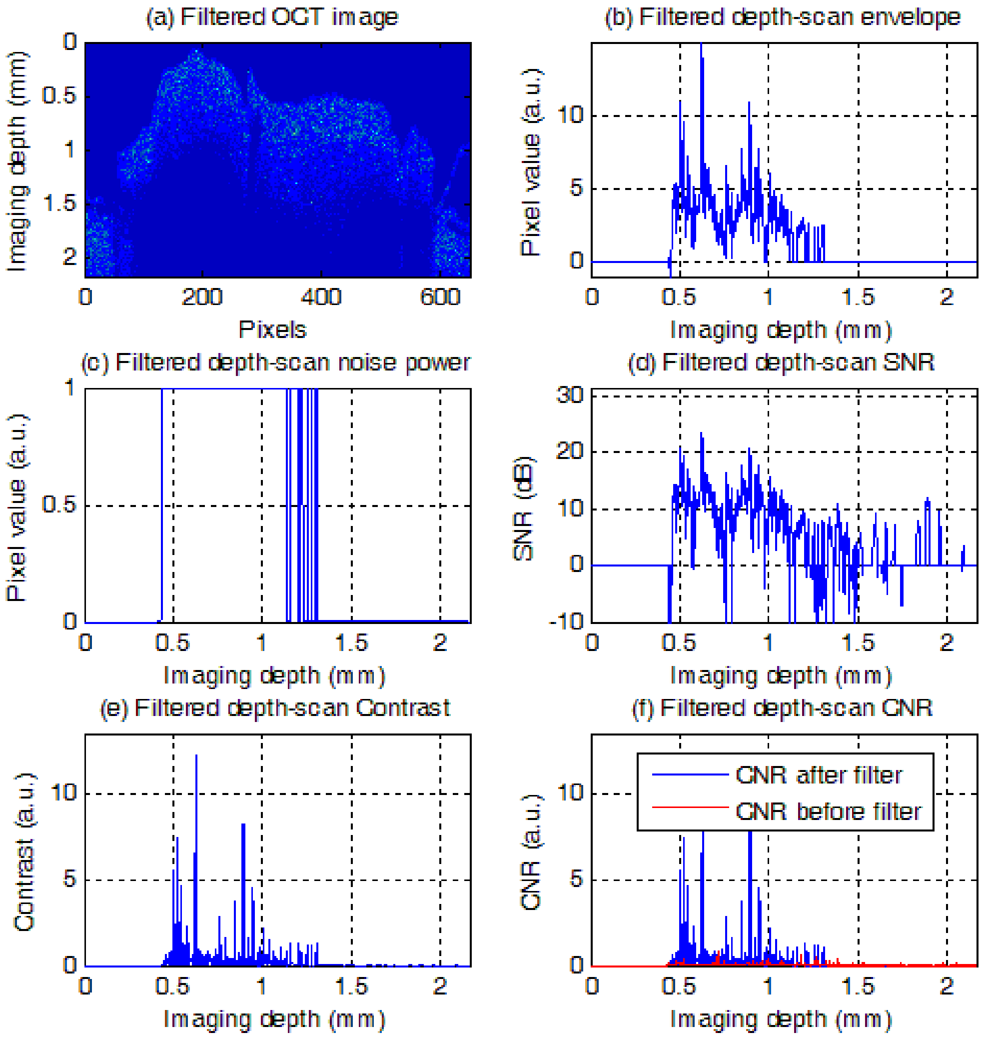

Figure 6.8: (a) Filtered OCT image; (b) filtered depth-scan envelope of vascular rabbit tissue (window size 13 pixels); (c) noise power; (d) SNR; (e) contrast; (f) CNR values of filtered depth-scan envelope of part (b).

.

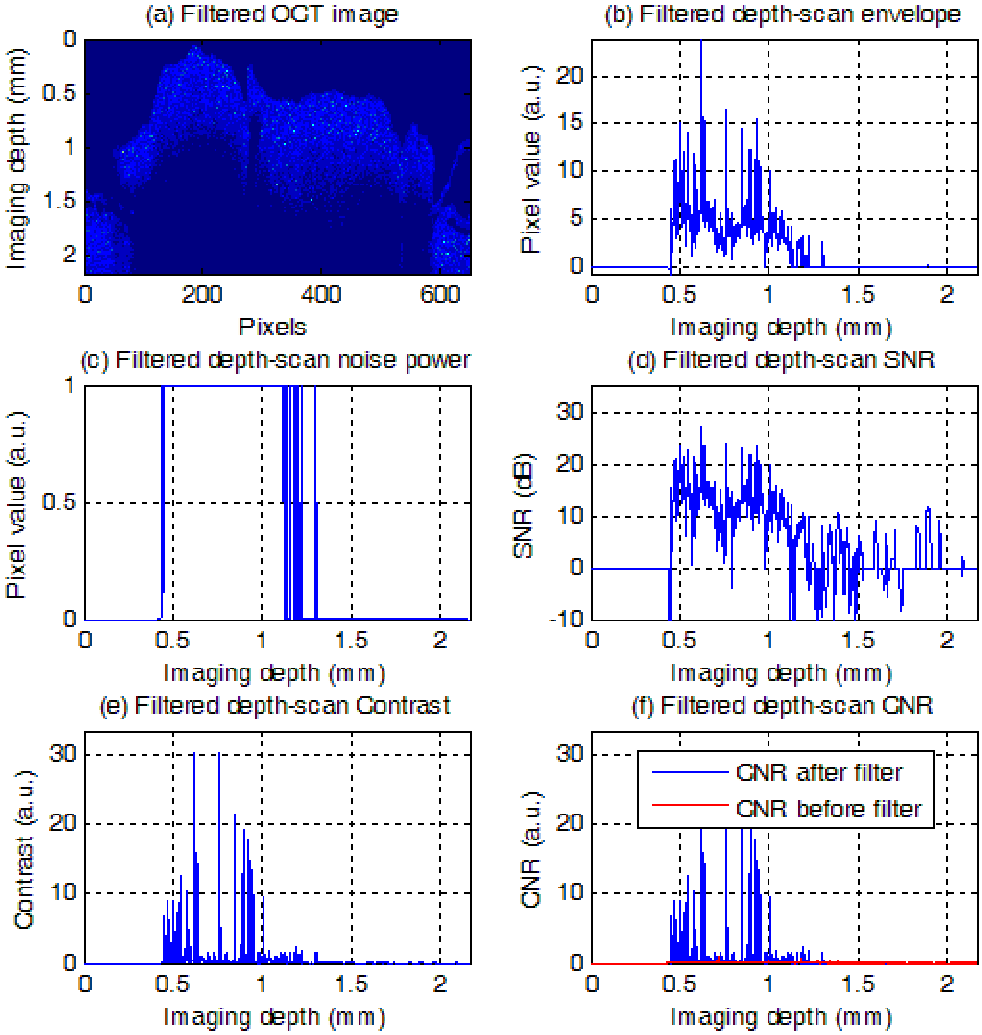

Figure 6.9: (a) Filtered OCT image; (b) filtered depth-scan envelope of vascular rabbit tissue (window size 15 pixels); (c) noise power; (d) SNR; (e) contrast; (f) CNR values of filtered depth-scan envelope of part (b).

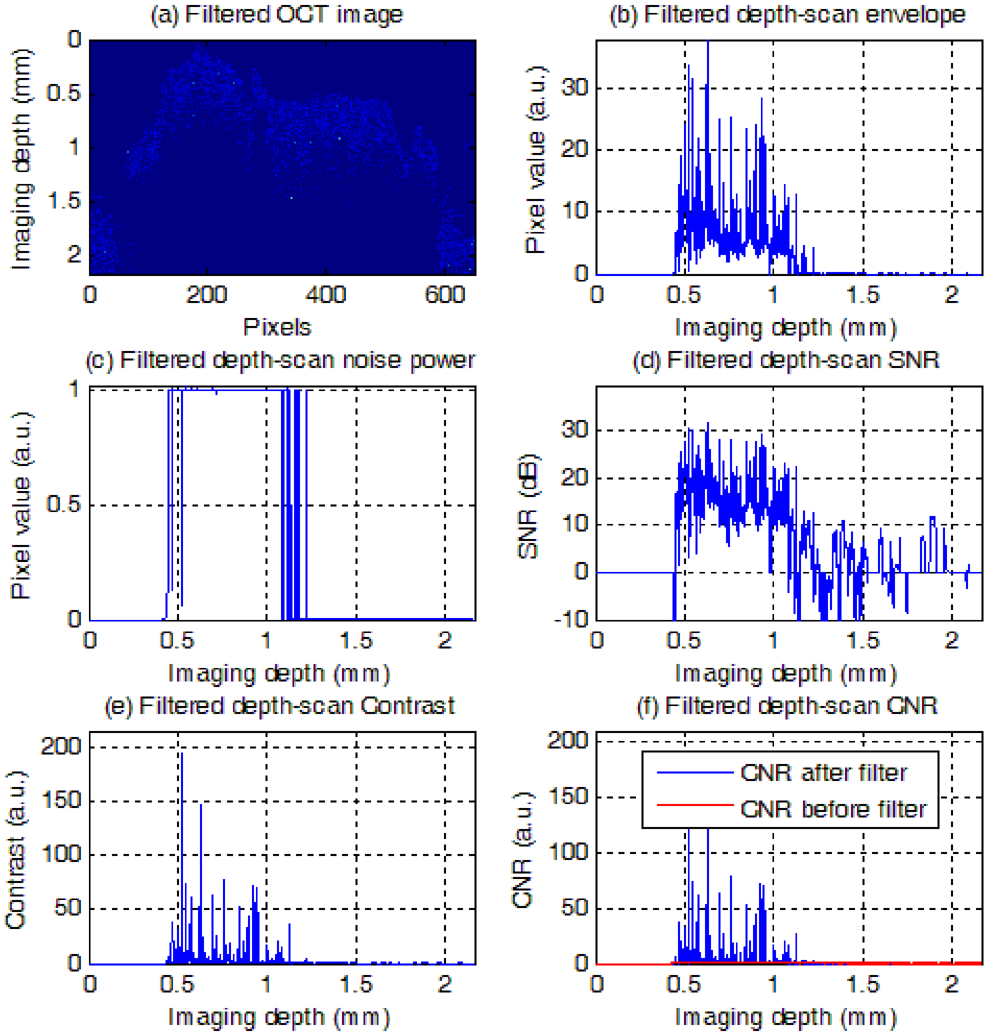

Figure 6.10: (a) Filtered OCT image; (b) filtered depth-scan envelope of vascular rabbit tissue (window size 17 pixels); (c) noise power; (d) SNR; (e) contrast; (f) CNR values of filtered depth-scan envelope of part (b).

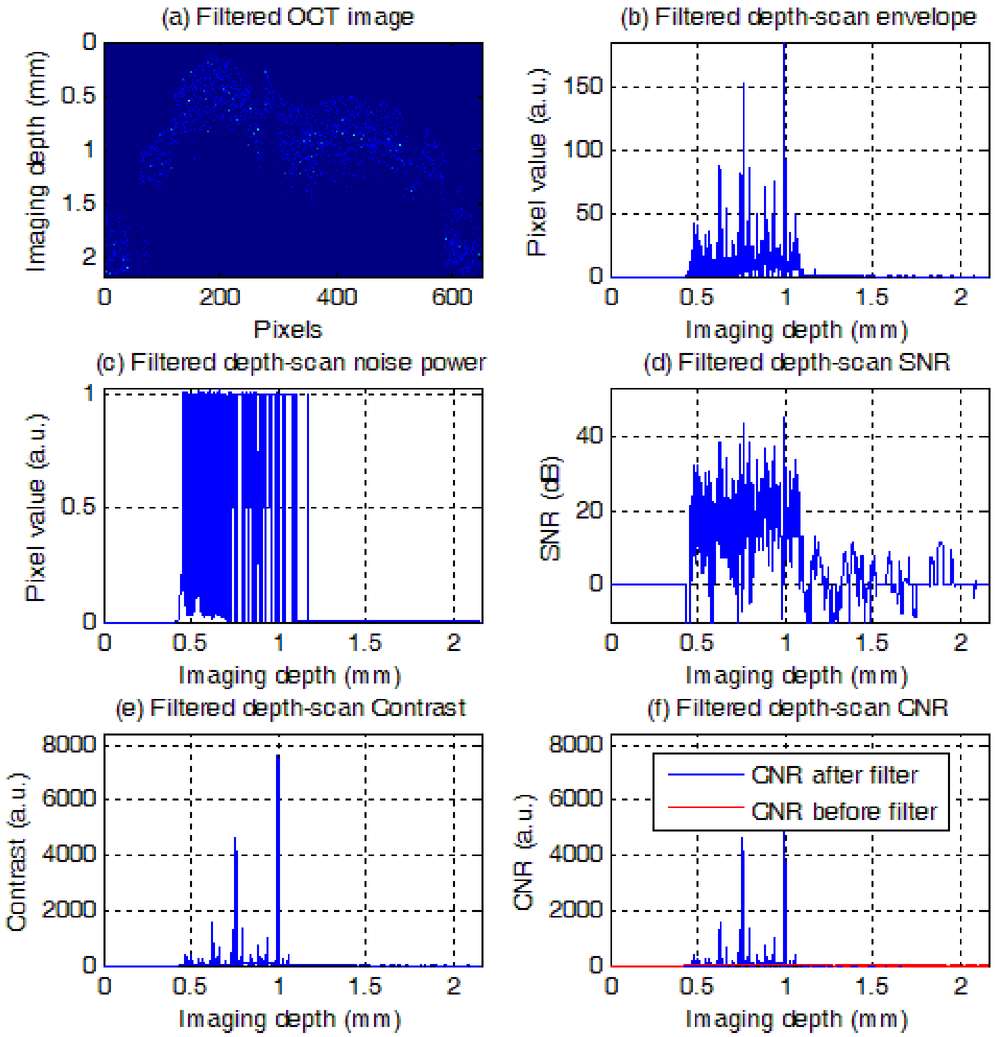

Figure 6.11: (a) Filtered OCT image; (b) filtered depth-scan envelope of vascular rabbit tissue (window size 19 pixels); (c) noise power; (d) SNR; (e) contrast; (f) CNR values of filtered depth-scan envelope of part (b).

To compare the SNR plots of Figures 6.3(d)-6.11(d), with each other and also to compare them with the SNR plot of Figure 6.2(d) and to decide on the best window size based on the SNR values, a quantitative analysis is performed on these SNR plots. The mean and the variance values of each of these SNR plots are calculated. In addition the Quality Measure (QM) value $QM_{SNR_{\hat{\boldsymbol{s}}}}$ for the SNR plot of Figure 6.2(d) is obtained using,

$$QM_{SNR_{\hat{\boldsymbol{s}}}} = \frac{[mean(SNR_{\hat{\boldsymbol{s}}})]^2}{var(SNR_{\hat{\boldsymbol{s}}})}, \tag{6.31}$$

where $SNR_{\hat{\boldsymbol{s}}}$, are the SNR values of the ensemble averaged depth-scan envelope, $\hat{\boldsymbol{s}}$. Also, the QM values of the SNR plots of Figure 6.3(d)-6.11(d) are obtained using,

$$QM_{SNR_{\boldsymbol{y}_{out}}} = \frac{[mean(SNR_{\boldsymbol{y}_{out}})]^2}{var(SNR_{\boldsymbol{y}_{out}})}\,. \tag{6.32}$$

where $SNR_{\boldsymbol{y}_{out}}$, are the SNR values of the filtered depth scan envelope, $\boldsymbol{y}_{out}$. These values are reported in Table 1 and are shown on Figure 6.12.

Table 6. 1: Mean; variance and QM values of SNR plots of averaged depth-scan envelope and filtered depth-scan envelopes of vascular rabbit tissue.

	Window size (pixels)	Mean of SNR	Variance of SNR	QM_{SNR}
Averaged depth-scan envelope	No window	-3.0946	28.7882	0.3327
Filtered depth scan envelope	3	1.3381	17.5582	0.1020
Filtered depth scan envelope	5	1.6373	17.5352	0.1529
Filtered depth scan envelope	7	2.0535	20.0025	0.2108
Filtered depth scan envelope	9	2.4945	25.8286	0.2409
Filtered depth scan envelope	11	3.0227	28.8056	0.3172
Filtered depth scan envelope	13	3.5886	35.9659	0.3581
Filtered depth scan envelope	15	4.3363	48.1199	0.3908
Filtered depth scan envelope	17	5.2091	71.9787	0.3770
Filtered depth scan envelope	19	5.3610	103.8787	0.2767

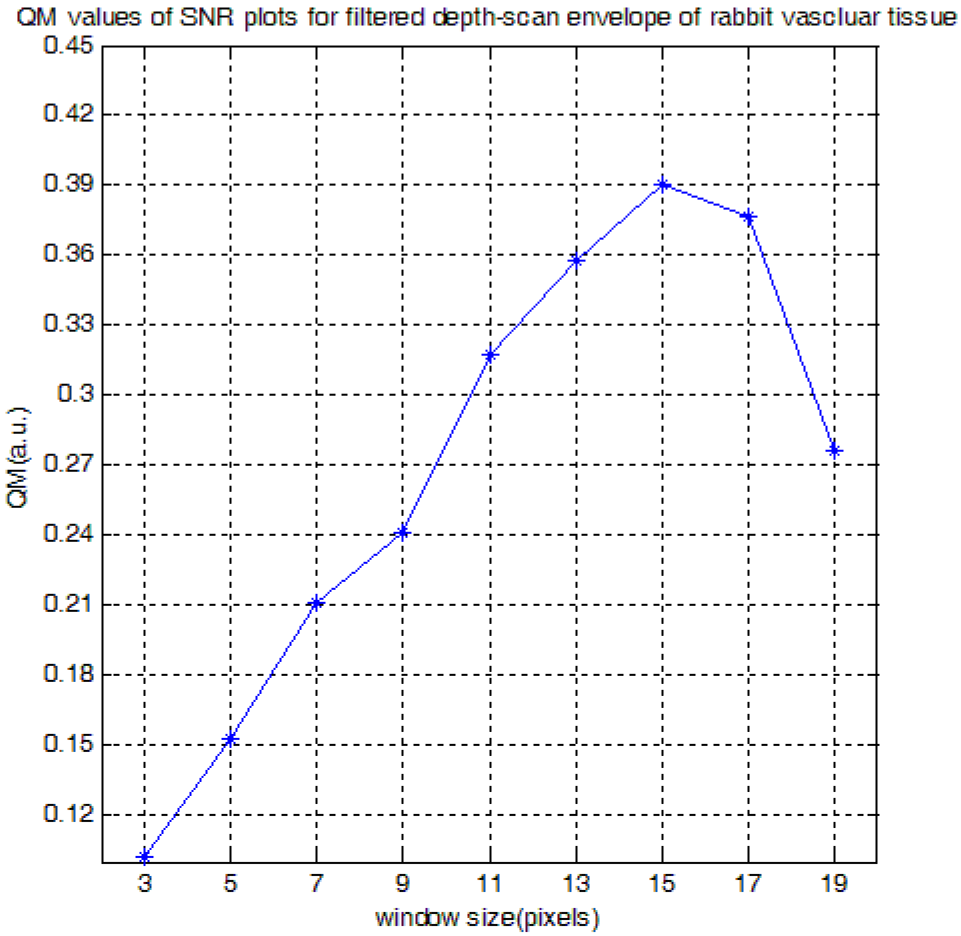

Figure 6.12: QM values of SNR plots of filtered depth-scan envelope of vascular rabbit tissue with different window sizes (3-19 pixels).

In addition, to compare the CNR plots of Figures 6.3(f)-6.11(f), with each other and to decide on the best window size based on the CNR values, a quantitative analysis is performed on these CNR plots. The mean and the variance values of each of these CNR plots are calculated. In addition the QM values $QM_{CNR_{\hat{s}}}$ for the CNR plot of Figure 6.2(f) are obtained using,

$$QM_{CNR_{\hat{s}}} = \frac{[mean(CNR_{\hat{s}})]^2}{var(CNR_{\hat{s}})}, \tag{6.33}$$

where $CNR_{\hat{s}}$, are the CNR values of the ensemble averaged depth-scan envelope, $\hat{\boldsymbol{s}}$. Also, the QM values of the CNR plots of Figures 6.3(f)-6.11(f) are obtained using

$$QM_{CNR_{y_{out}}} = \frac{[mean(CNR_{y_{out}})]^2}{\sigma(CNR_{y_{out}})} . \tag{6.34}$$

where $CNR_{\boldsymbol{y}_{out}}$ are the CNR values of filtered depth-scan envelope, $\boldsymbol{y}_{out}$. These values are reported in Table 2 and are shown on Figure 6.13.

Table 6. 2: Mean; variance and QM values of CNR plots of averaged depth-scan envelope and filtered depth- scan envelopes of vascular rabbit tissue.

	Window size (pixels)	Mean of CNR	Variance of CNR	QM_{CNR}
Averaged depth-scan envelope	No window	0.0405	0.0034	0.4836
Filtered depth scan envelope	3	0.1816	0.0971	0.3396
Filtered depth scan envelope	5	0.1696	0.0656	0.4381
Filtered depth scan envelope	7	0.1713	0.0707	0.4151
Filtered depth scan envelope	9	0.1846	0.0962	0.3542
Filtered depth scan envelope	11	0.2436	0.3096	0.1917
Filtered depth scan envelope	13	0.4397	1.2500	0.1547
Filtered depth scan envelope	15	1.3632	11.6807	0.1591
Filtered depth scan envelope	17	6.5834	244.0594	0.1776
Filtered depth scan envelope	19	133.9521	2.5274e+005	0.0710

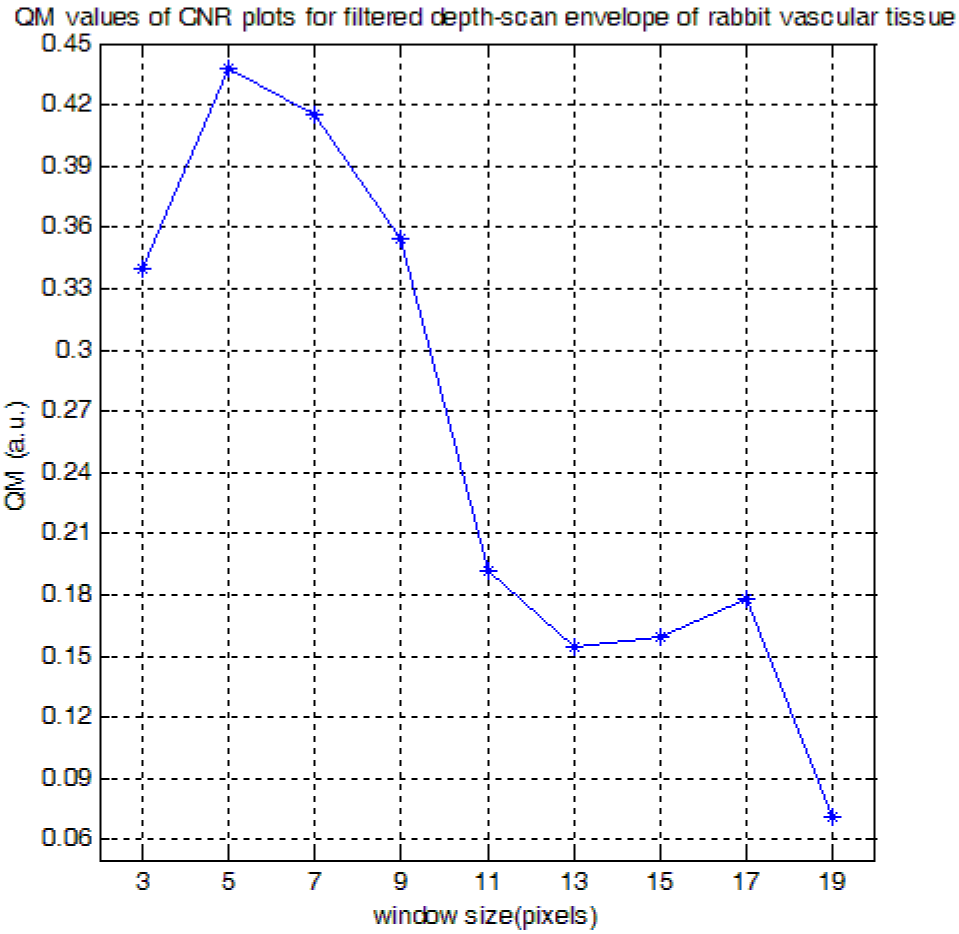

Figure 6.13: QM values of CNR plots of filtered depth-scan envelopes of vascular rabbit tissue for different window sizes (3-19 pixels).

6.4.1 Discussion of imaging results for rabbit vascular tissue

The filtered-OCT images of vascular rabbit tissue are shown by Figures 6.3(a)-6.11(a). One filtered depth-scan envelope and its noise power are shown in Figures 6.3(b)-6.11(b) and Figures 6.3(c)-6.11(c), respectively. We observe that the power of the noise, Figures 6.3(c)-6.11(c), is limited to unity as per the design constraint of our filter, $\boldsymbol{h}^H\boldsymbol{C}\boldsymbol{h} = 1$.On comparing the filtered depth-scan envelopes of Figures 6.3(b)-6.9(b) to the averaged depth-scan envelope of Figure 6.2(b), we note that by increasing the size of filter from 6 - 15 pixels, the values of the filtered depth-scan envelopes are extended to the higher depths of imaging.. We recall that the assumption of stationary noise will become less valid as the window size gets larger. The contrast at each pixel of the filtered depth-scan is obtained using Eq. (6.28) and is shown for different window sizes in Figures 6.3(e)-6.11(e). The SNR values of the filtered depth-scan envelopes at each pixel are obtained using Eq. (6.26). These SNR values are shown in Figures 6.3(d)-6.11(d). By comparing these SNR plots with the SNR plot of the averaged depth-scan envelope, Figure 6.2(d), we note that the SNR values are increased overall after matched filtering. To have a quantitative comparison between the SNR plots of Figures 6.3(d)-6.11(d) and to decide on the best window size regarding the SNR values, the $QM_{SNR_{y_{out}}}$ values are obtained using Eq. (6.32) and shown on Figure 6.12. From this figure, we note that the maximum value of $QM_{SNR_{y_{out}}}$ is obtained for the depth-dependent matched filter of window size 15 pixels. In addition, the CNR values at each pixel of the filtered depth-scan envelopes are obtained using Eq. (6.28) and Eq. (6.30). The CNR values for the averaged depth-scan envelope (red plot) and the filtered depth-scan envelope (blue plot) are shown in Figures 6.3(f)-6.11(f). A comparison of these CNR plots (red plot and blue plot) demonstrates that the CNR values of a filtered depth-scan envelope are overall higher than the CNR of an averaged depth-scan envelope. To have a quantitative comparison between the CNR plots of Figures 6.3(f)-6.11(f) and to decide on the best window size regarding the CNR values, the $QM_{CNR_{y_{out}}}$ values are obtained using Eq. (6.34) and are shown on Figure 6.13. From this figure, we note that the maximum value of $QM_{CNR_{y_{out}}}$ is obtained using the depth-dependent matched filter of window size 5 pixels. In addition by considering the results of our filter, we note that the filtered image of Figure 6.4(a) visually has a good contrast. Therefore, we conclude that *for this sample* a window size of 5 pixels is the best window size.

As another example, we show the results of simple averaging method of 40 TD-OCT images of a human tooth and compare them with results from our proposed depth-dependent matched filter (window sizes of 3-19 pixels). The ensemble average of these 40 OCT images is shown by Figure 6.14(a). We note that features of this sample are not clear in the averaged OCT image of Figure 6.14(a). Hence regular averaging is not a suitable method to increase the depth of OCT imaging. The ensemble average of an arbitrary depth-scan envelope from 40 OCT images and its noise power are shown in Figure 6.14(b) and Figure 6.14(c), respectively. From these plots, we note that, the noise power in the averaged depth-scan envelope depend on the average depth-scan envelope which varies with different depths of imaging. We also observe that the maximum value of the averaged depth-scan envelope noise power corresponds to the maximum value of the averaged depth-scan envelope. To evaluate the performance our proposed filter, we obtained both SNR value, Eq. (6.25), and CNR value, Eq. (6.27) and Eq. (6.29), for the averaged depth-scan envelope of Figure 6.14(b). These SNR and CNR values are shown in Figure 6.14(d) and Figure 6.14(f) respectively. The contrast at each pixel of averaged depth-scan envelope was calculated using Eq. (6.27) and is shown in Figure 6.12(e).

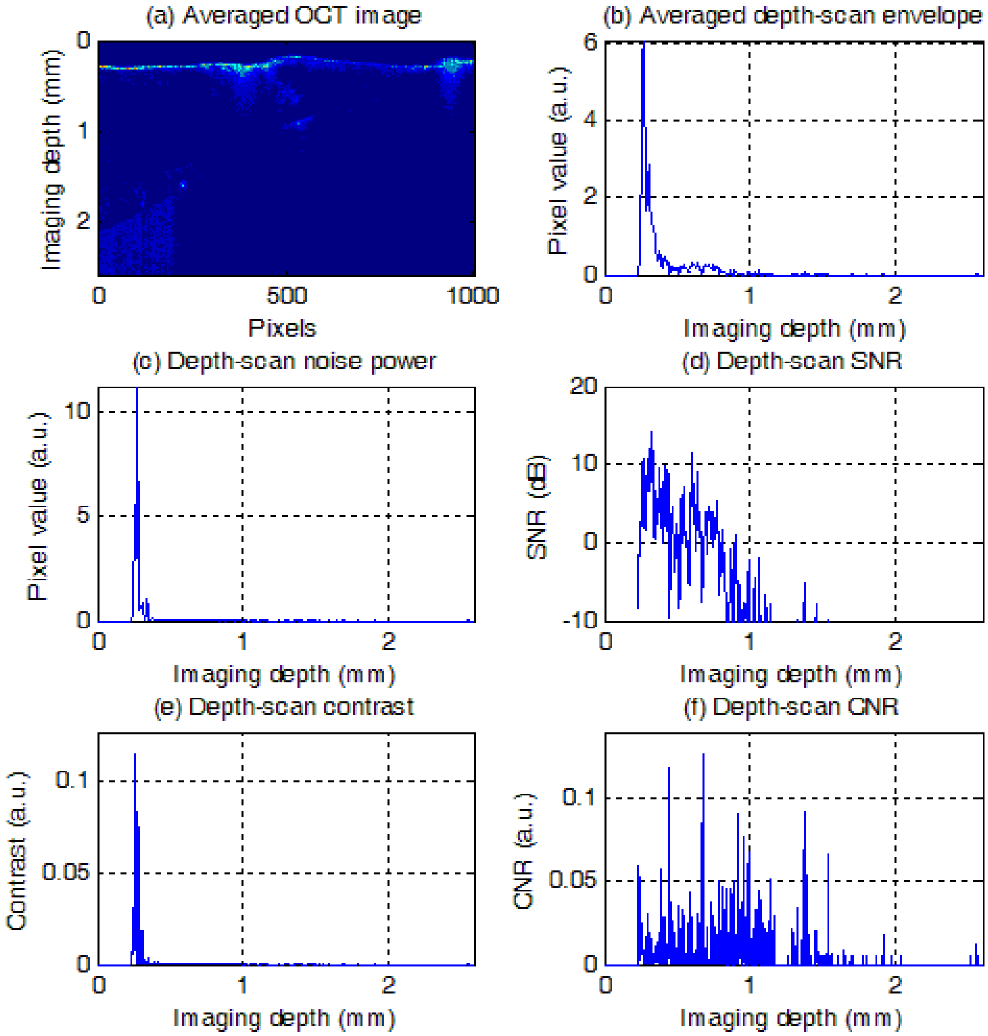

Fig 6.14: (a) Averaged OCT image; (b) averaged depth-scan envelope of a human tooth; (c) noise power; (d) SNR; (e) contrast; (f) CNR values of averaged depth-scan envelope of part (b).

The results of applying our depth-dependent matched filter with different window sizes ranging from 3 pixels to 19 pixels are shown in Figures 6.15(a-f)-6.23(a-f).

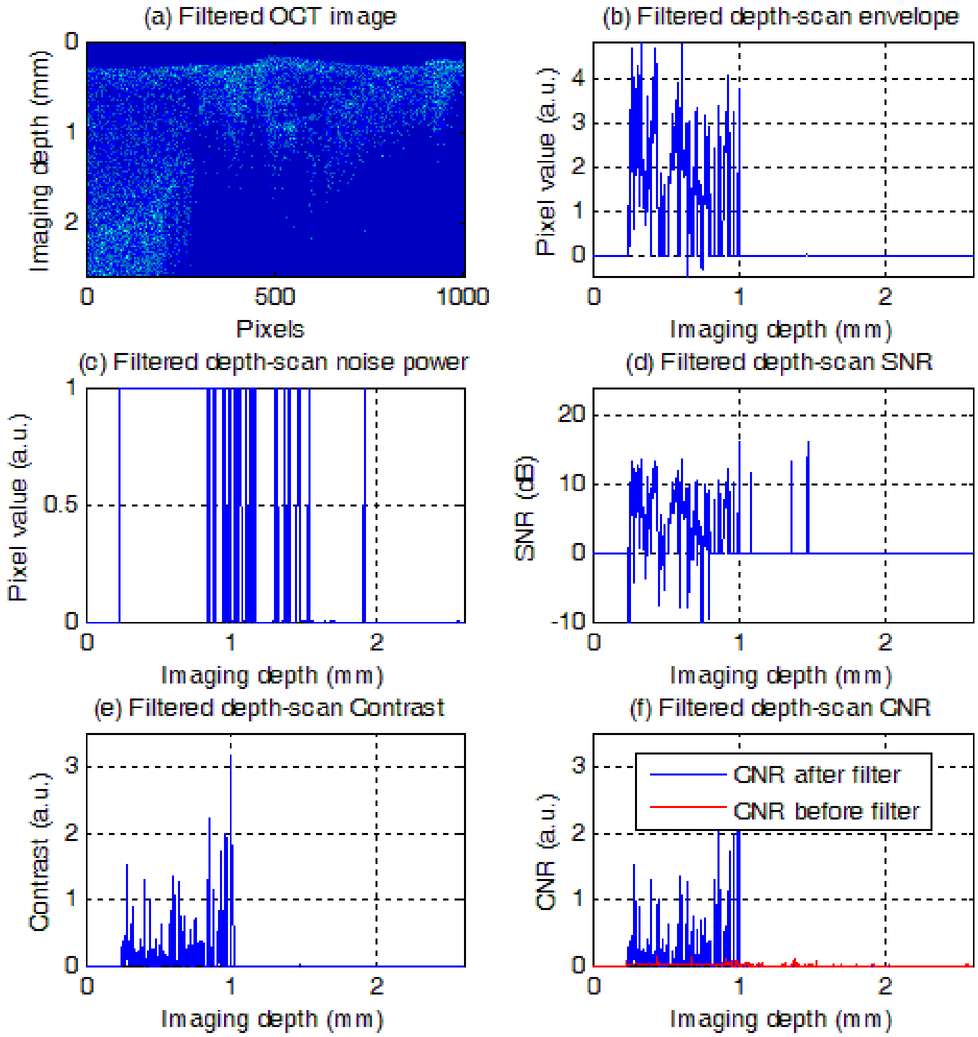

Figure 6.15: (a) Filtered OCT image; (b) filtered depth-scan envelope of a human tooth (window size 3 pixels); (c) noise power; (d) SNR; (e) contrast; (f) CNR values of filtered depth-scan envelope of part (b).

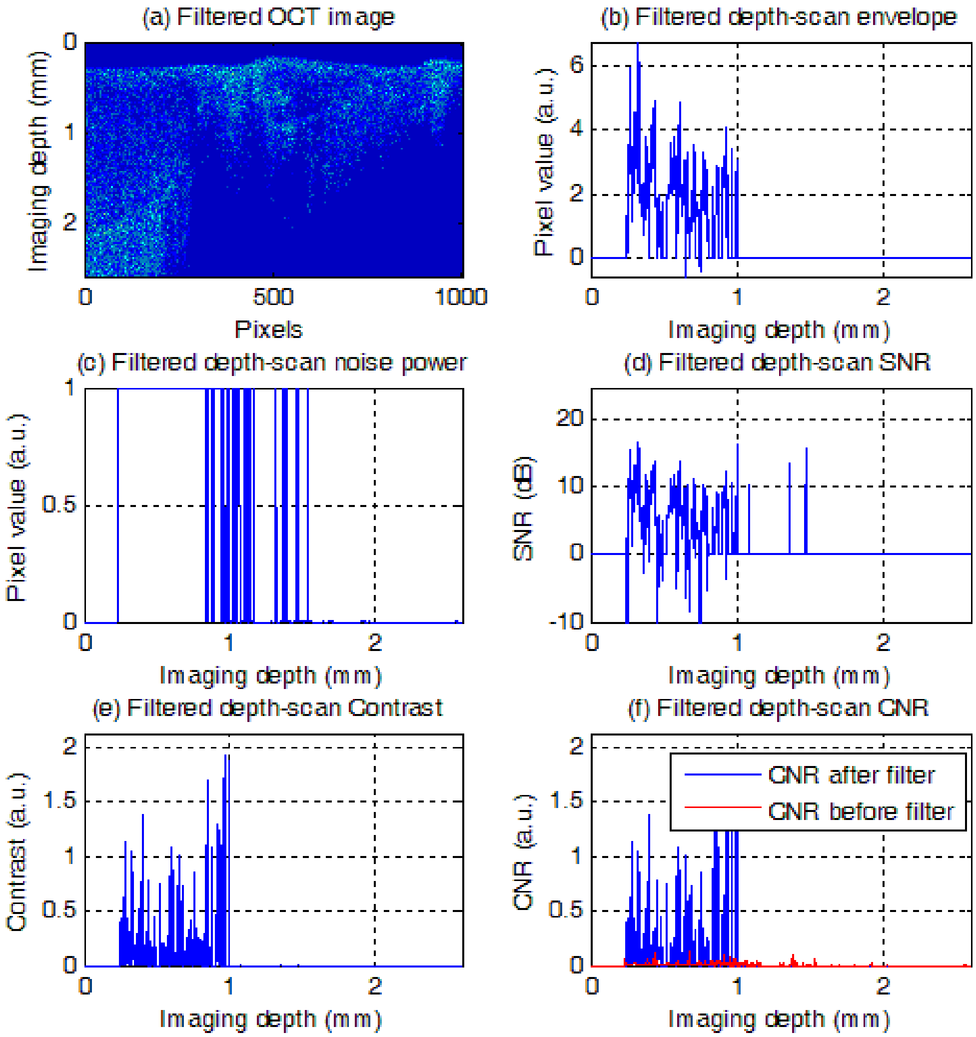

Figure 6.16: (a) Filtered OCT image; (b) filtered depth-scan envelope of a human tooth (window size 5 pixels); (c) noise power; (d) SNR; (e) contrast; (f) CNR values of filtered depth-scan envelope of part (b).

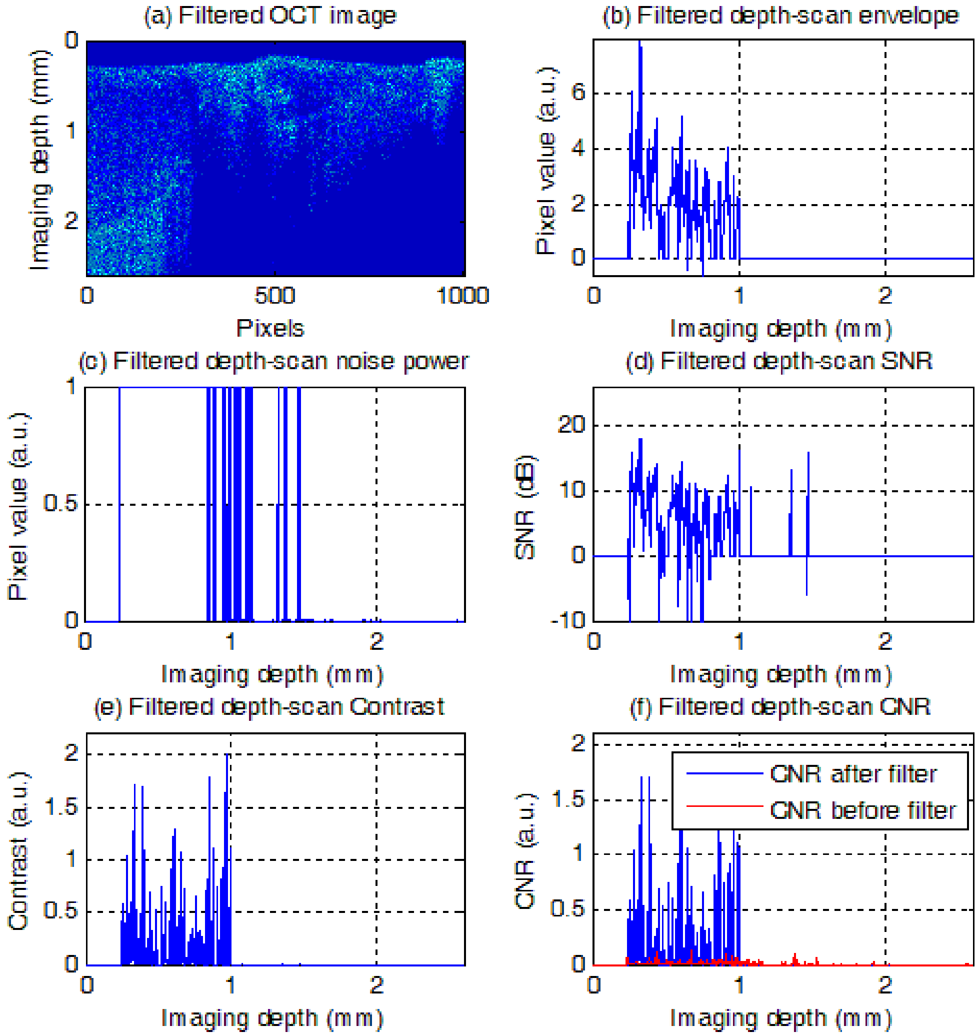

Figure 6.17: (a) Filtered OCT image; (b) filtered depth-scan envelope of a human tooth (window size 7 pixels); (c) noise power; (d) SNR; (e) contrast; (f) CNR values of filtered depth-scan envelope of part (b).

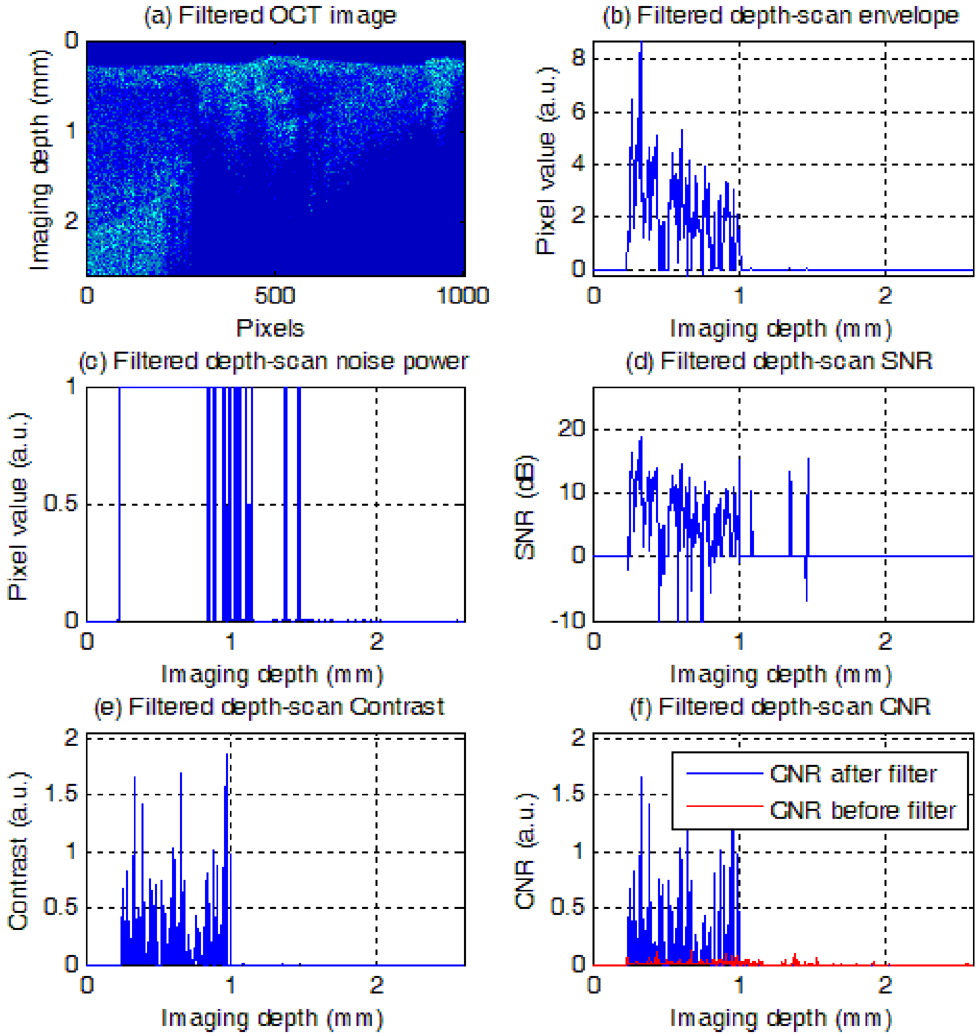

Figure 6.18: (a) Filtered OCT image; (b) filtered depth-scan envelope of a human tooth (window size 9 pixels); (c) noise power; (d) SNR; (e) contrast; (f) CNR values of filtered depth-scan envelope of part (b).

.

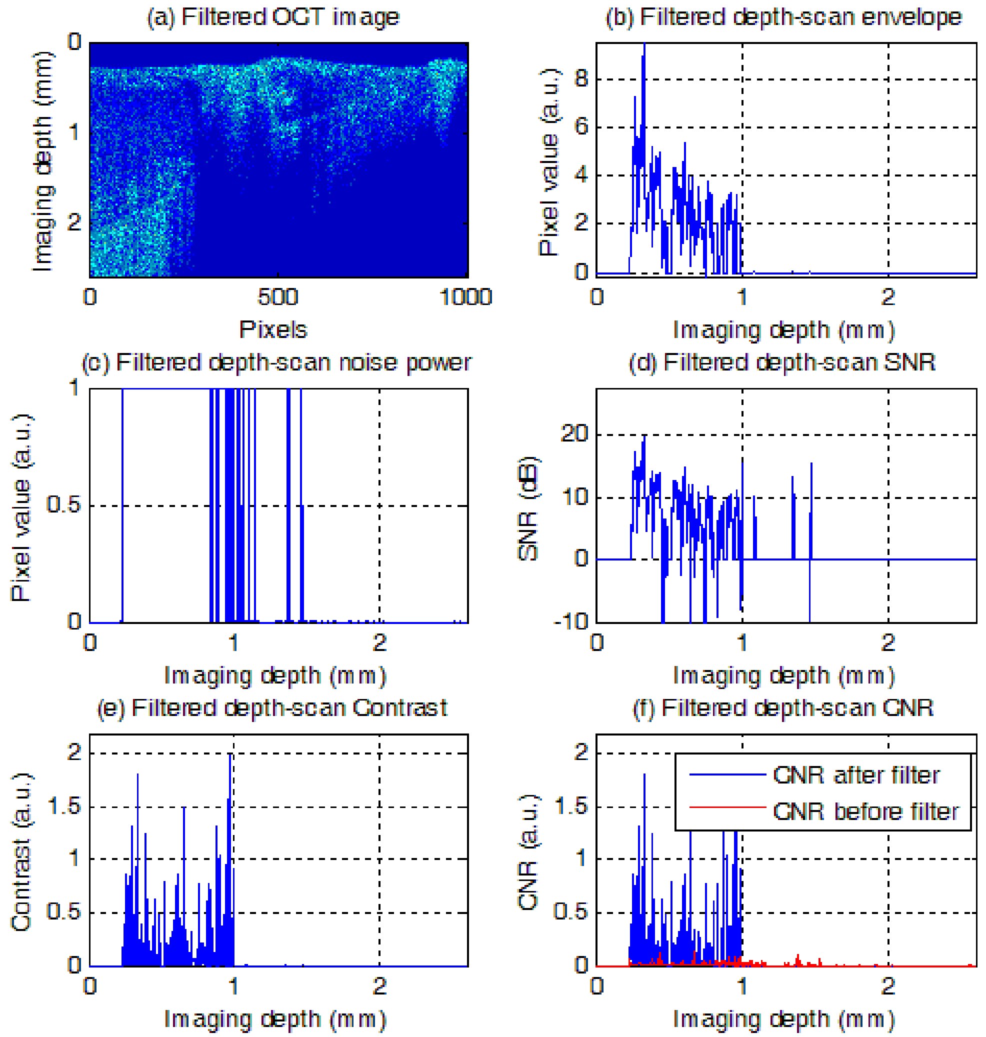

Figure 6.19: (a) Filtered OCT image; (b) filtered depth-scan envelope of a human tooth (window size 11 pixels); (c) noise power; (d) SNR; (e) contrast; (f) CNR values of filtered depth-scan envelope of part (b).

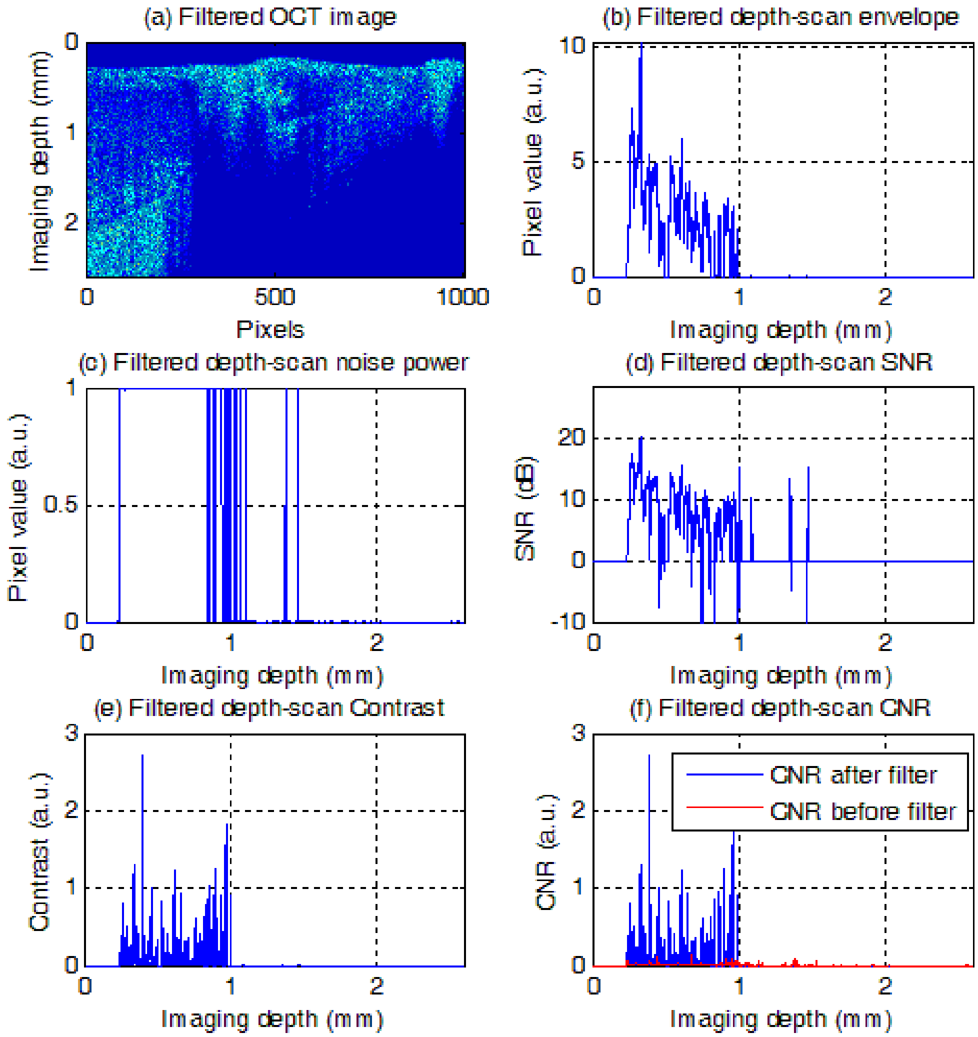

Figure 6.20: (a) Filtered OCT image; (b) filtered depth-scan envelope of a human tooth (window size 13 pixels); (c) noise power; (d) SNR; (e) contrast; (f) CNR values of filtered depth-scan envelope of part (b).

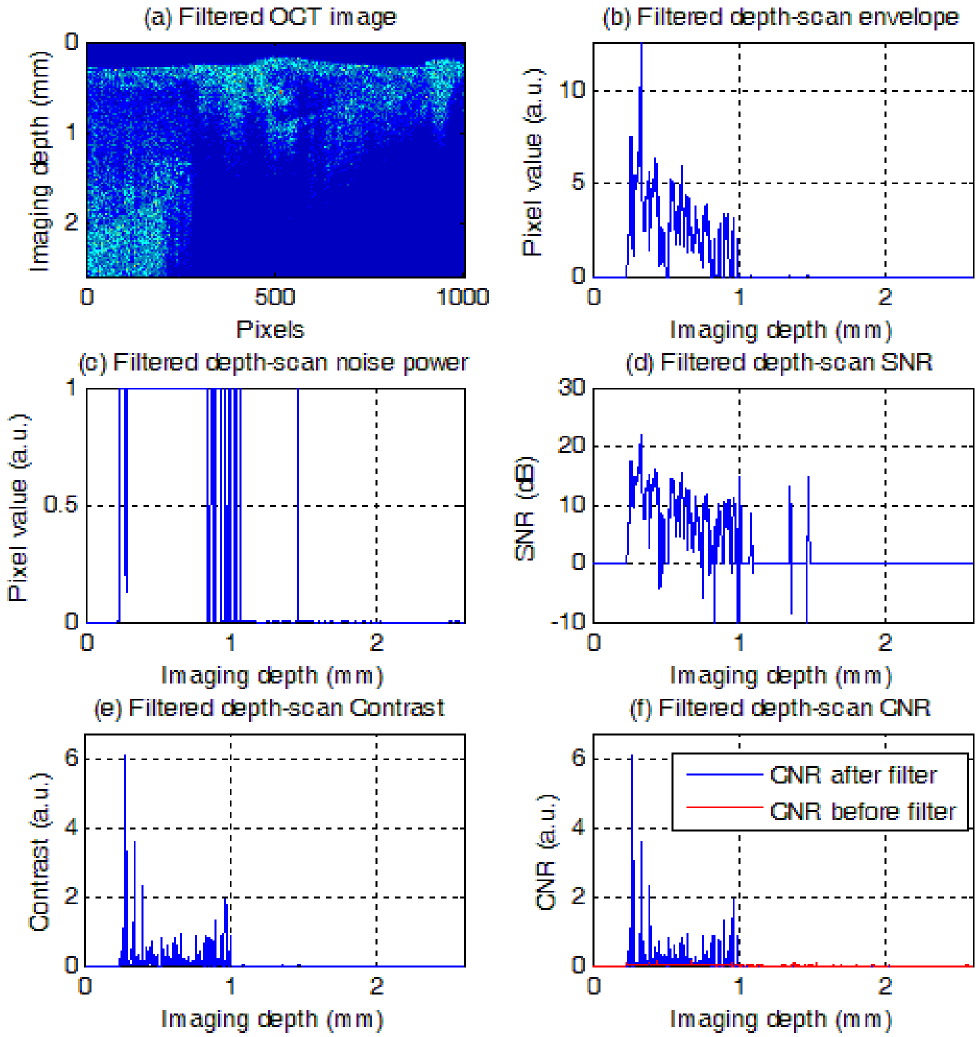

Figure 6.21: (a) Filtered OCT image; (b) filtered depth-scan envelope of a human tooth (window size 15 pixels); (c) noise power; (d) SNR; (e) contrast; (f) CNR values of filtered depth-scan envelope of part (b).

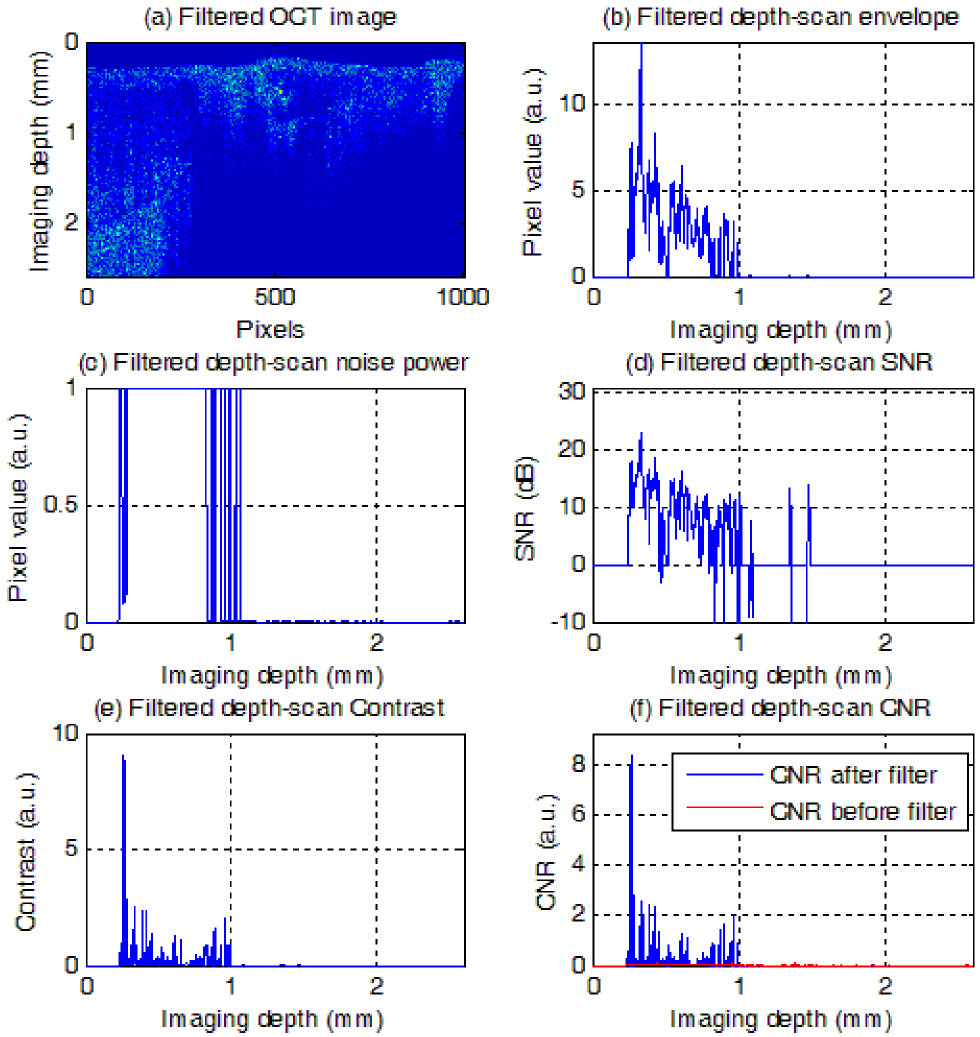

Figure 6.22: (a) Filtered OCT image; (b) filtered depth-scan envelope of a human tooth (window size 17 pixels); (c) noise power; (d) SNR; (e) contrast; (f) CNR values of filtered depth-scan envelope of part (b).

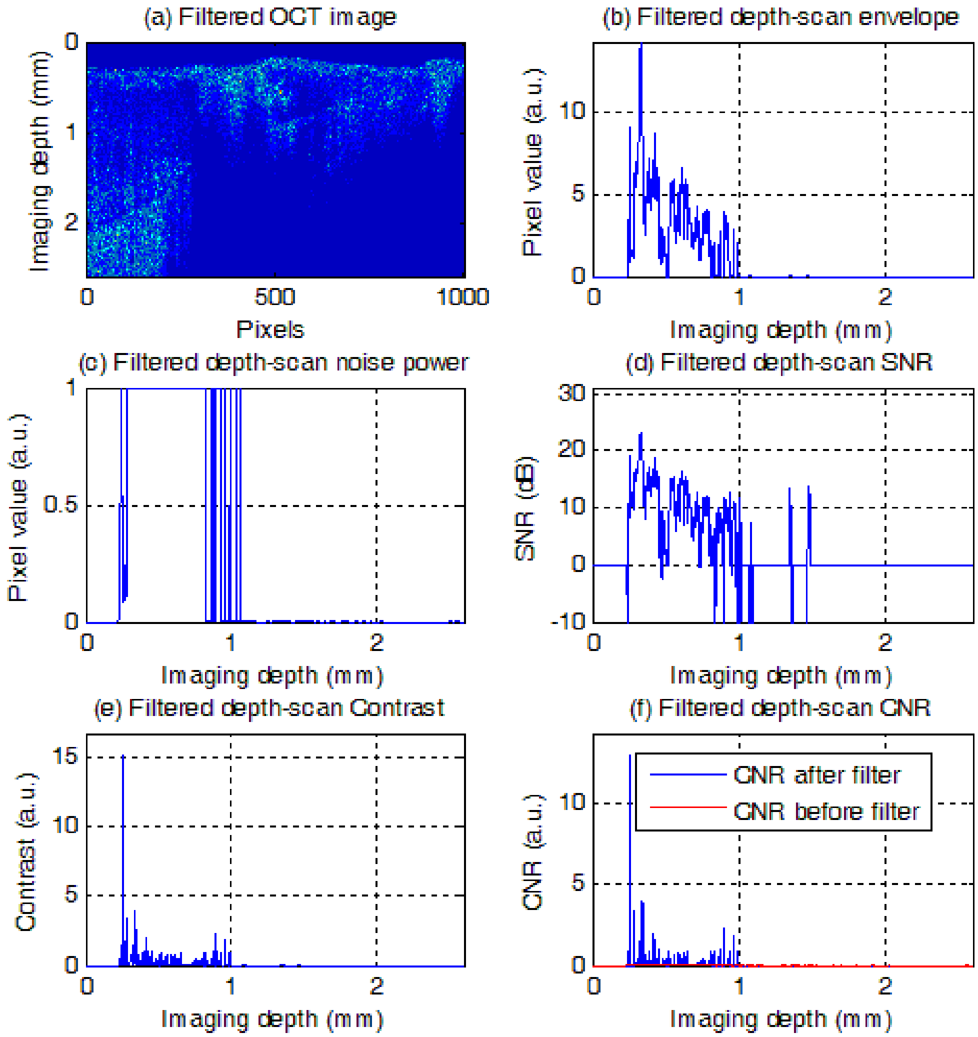

Figure 6.23: (a) Filtered OCT image; (b) filtered depth-scan envelope of a human tooth (window size 19 pixels); (c) noise power; (d) SNR; (e) contrast; (f) CNR values of filtered depth-scan envelope of part (b).

To compare the SNR plots of Figures 6.15(d)-6.23(d) and also to compare them with the SNR plot of Figure 6.14(d) and to decide on about the best window size based on the SNR values, a quantitative analysis is performed on these SNR plots. The mean and the variance values of each of these SNR plots are calculated and reported in Table 3. In addition the values of $QM_{SNR_{\hat{s}}}$ and $QM_{SNR_{y_{out}}}$ are obtained using Eq. (6.31) and Eq. (6.32) respectively. These values are reported in Table 3 and are shown on Figure 6.24.

Table 6. 3: Mean; variance and QM values of SNR plots of averaged depth-scan envelope and filtered depth- scan envelopes of a human tooth.

	Window size (pixels)	Mean of SNR	Variance of SNR	QM_{SNR}
Averaged depth-scan envelope	No window	-1.1081	26.0428	0.0471
Filtered depth scan envelope	3	1.3165	11.6305	0.1490
Filtered depth scan envelope	5	1.4856	13.7575	0.1604
Filtered depth scan envelope	7	1.6450	17.0571	0.1587
Filtered depth scan envelope	9	1.8596	18.4190	0.1877
Filtered depth scan envelope	11	2.0758	19.6915	0.2188
Filtered depth scan envelope	13	2.2972	21.9390	0.2405
Filtered depth scan envelope	15	2.4798	24.3847	0.2522
Filtered depth scan envelope	17	2.6276	27.9315	0.2472
Filtered depth scan envelope	19	2.7095	33.3323	0.2203

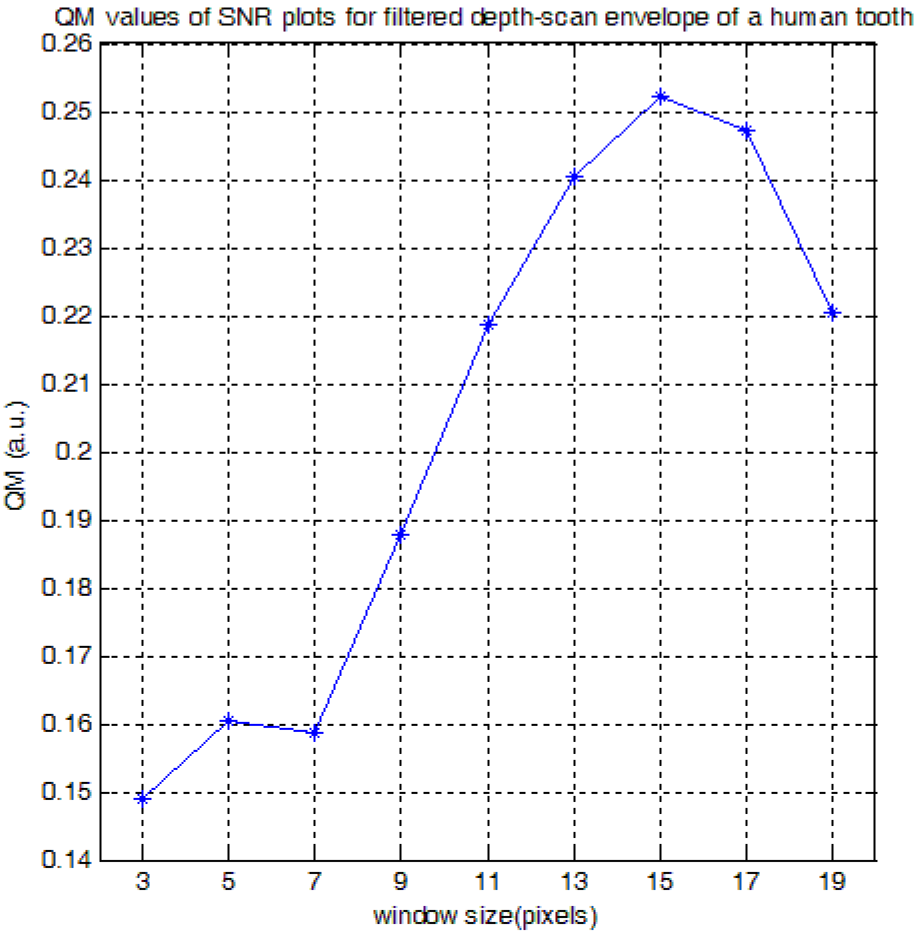

Figure 6.24: QM values of SNR plots of filtered depth-scan envelopes of a human tooth for different window sizes (3-19 pixels).

In addition, to compare the CNR plots of Figures 6.15(f)-6.23(f) and to decide on the best window size based on the CNR values, a quantitative analysis is performed on these CNR plots. The mean and the variance values of each of these CNR plots are calculated. In addition the values of $QM_{CNR_{\hat{s}}}$ and $QM_{CNR_{y_{out}}}$ are obtained using Eq. (6.33) and Eq. (6.34) respectively. These values are reported in Table 4 and are shown on Figure 6.25.

Table 6. 4: Mean; variance and QM values of CNR plots of averaged depth-scan envelope and filtered depth- scan envelopes of a human tooth.

	Window size (pixels)	Mean of CNR	Variance of CNR	QM_{CNR}
Averaged depth-scan envelope	No window	0.0107	1.9175e-004	0.5989
Filtered depth scan envelope	3	0.2043	0.1473	0.2833
Filtered depth scan envelope	5	0.1714	0.0861	0.3413
Filtered depth scan envelope	7	0.1659	0.0835	0.3296
Filtered depth scan envelope	9	0.1484	0.0680	0.3239
Filtered depth scan envelope	11	0.1447	0.0681	0.3077
Filtered depth scan envelope	13	0.1387	0.0794	0.2422
Filtered depth scan envelope	15	0.1775	0.1927	0.1635
Filtered depth scan envelope	17	0.2306	0.4916	0.1082
Filtered depth scan envelope	19	0.2065	0.4492	0.0949

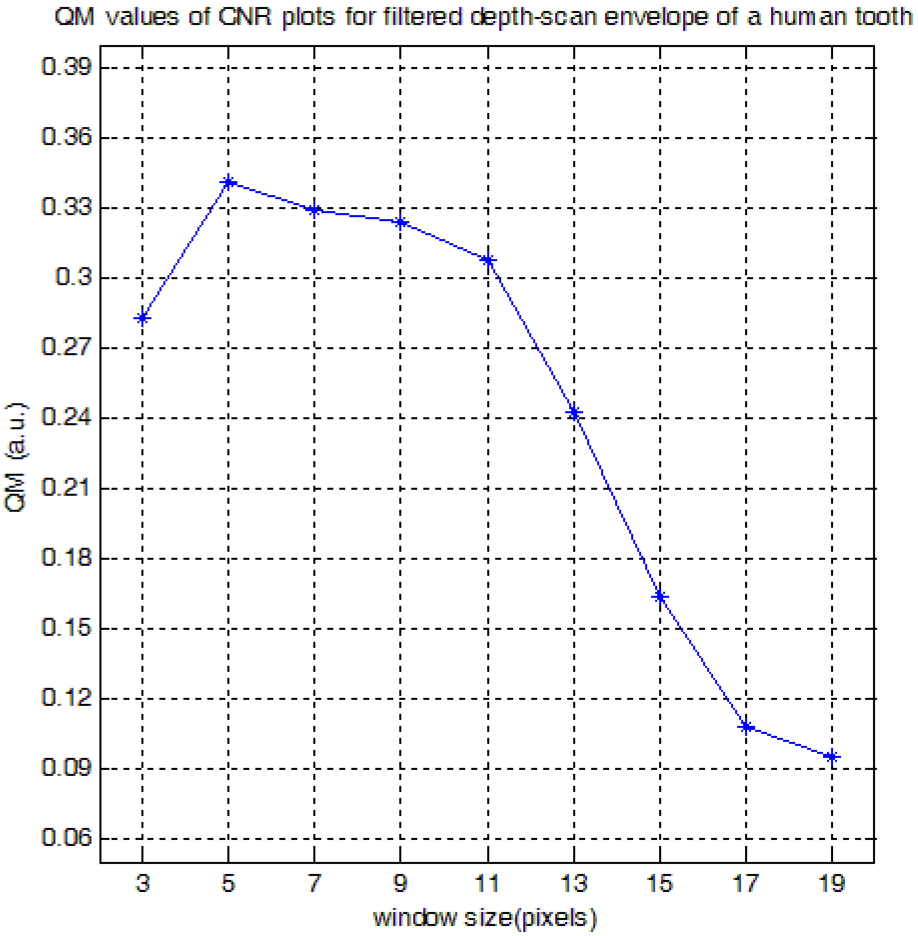

Figure 6.25: QM values of CNR plots of filtered depth-scan envelopes of a human tooth for different window sizes (3-19 pixels).

6.4.2 Discussion of imaging results for a human tooth

The filtered-OCT images of a human tooth are shown by Figures 6.15(a)-6.23(a). One filtered depth-scan envelope and its noise power are shown in Figures 6.15(b)-6.23(b) and Figures 6.15(c)-6.23(c), respectively. We observe that the power of the noise, Figures

6.15(c)-6.23(c), is limited to unity as per the design constraint of our filter, $\boldsymbol{h}^H \boldsymbol{C}\boldsymbol{h} = 1$. The contrast at each pixel of the filtered depth-scan is obtained using Eq. (6.28) and is shown for different window sizes in Figures 6.15(e)-6.23(e). The SNR values of the filtered depth-scan envelopes at each pixel are obtained using Eq. (6.26). These SNR values are shown in Figures 6.15(d)-6.23(d). By comparing these SNR plots with the SNR plot of the averaged depth-scan envelope, Figure 6.14(d), we note that the SNR values are increased overall after matched filtering. To have a quantitative comparison between the SNR plots of Figures 6.15(d)-6.23(d) and to decide on the best window size regarding to the SNR values, the $QM_{SNR_{y_{out}}}$ values are obtained using Eq. (6.32) and shown on Figure 6.24. From this figure, we note that the maximum value of $QM_{SNR_{y_{out}}}$ is obtained for the depth-dependent matched filter of window size 15 pixels. In addition, the CNR values at each pixel of the filtered depth-scan envelopes are obtained using Eq. (6.28) and Eq. (6.30). The CNR values for the averaged depth-scan envelope (red plot) and the filtered depth-scan envelope (blue plot) are shown in Figures 6.13(f)-6.1(f). A comparison of these CNR plots (red plot and blue plot) demonstrates that the CNR values of a filtered depth-scan envelope are higher than the CNR of an averaged depth-scan envelope. To have a quantitative comparison between the CNR plots of Figures 6.15(f)-6.23(f) and to decide on the best window size regarding the CNR values, the $QM_{CNR_{y_{out}}}$ values are obtained using Eq. (6.34) and are shown on Figure 6.25. From this figure, we note that the maximum value of $QM_{CNR_{y_{out}}}$is obtained using the depth-dependent matched filter of window size 5 pixels. In addition by considering the results of our filter, we note that the filtered image of Figure 6.16(a) visually has a good contrast. Therefore, we conclude that *for this sample* a window size of 5 pixels is the best window size.

Chapter 7

Conclusions & Future work

7.1 Conclusions

Achieving higher depth of imaging is an important goal in all types of OCT systems. Having higher depth of imaging allows the study of features and structures of a sample from higher depths. In biomedical applications, it is useful for physicians to see deeper regions in tissue, to diagnose potential abnormalities. One main factor that affects the depth of OCT imaging is the presence of noise. Therefore studying the statistical properties of noise in OCT data would be very useful in proposing new image processing methods to increase the depth of OCT imaging.

In the first part of this thesis we obtain an empirical estimate of the second order statistics of noise by using a sequence of Time domain (TD) OCT images. These estimates confirm the non-stationary nature of noise in TD-OCT. One reason of this non-stationary noise is its dependence on the reflected signal from an object; thereby it is also depth-dependent for non-homogenous objects. In the second part of the thesis these estimates are used to design a depth-dependent matched filter to maximize the SNR and increase the CNR in TD-OCT. By applying our filter to images of vascular rabbit tissue and images of a human tooth, both SNR and CNR were increased for higher imaging depths.

7.2 Future work

An important practical limitation of our depth-dependent matched filter is the need to repeat the OCT imaging several times to have accurate estimates of noise statistics. This could be practical problem for the real time OCT imaging. Potential implementation of this filter using a Field Programmable Gate Array **(**FPGA) based computing platform would be an important project for the future. Since there was no assumption about the type of OCT imaging system in the derivation of our matched filter, we anticipate that this filter will work for other types of OCT imaging such as Fourier domain OCT. The verification of this assumption could be performed in the future.

References

[1] D. Huang, E. A. Swanson, C. P. Lin, J. S. Schuman, W. G. Stinson, W. Chang, M. R. Hee, T. Flotte, K. Gregory, and C. A. Puliafito, “Optical coherence tomography.,” *Science*, vol. 4, no. 4, pp. 198–204, 1991.

[2] A. F. Fercher, W. Drexler, C. K. Hitzenberger, and T. Lasser, “Optical coherence tomography: principles and applications,” *Reports on Progress in Physics*, vol. 66, p. 239, 2003.

[3] D. Stifter, “Beyond biomedicine: a review of alternative applications and developments for optical coherence tomography,” *Applied Physics B*, vol. 88, no. 3, pp. 337–357, 2007.

[4] J. G. Fujimoto, *Optical coherence tomography imaging: Technology and applications*. IEEE, 2011, pp. 1–1.

[5] S. S. Sherif, C. C. Rosa, C. Flueraru, S. Chang, Y. Mao, and A. G. Podoleanu, “Statistics of the depth-scan photocurrent in time-domain optical coherence tomography,” *Journal of the Optical Society of America A*, vol. 25, no. 1, pp. 16–20, 2008.

[6] B. E. Bouma and G. J. Tearney, *Handbook of Optical Coherence Tomography*, vol. 6162. Marcel Dekker, 2002, pp. p. 44–45.

[7] B. E. A. Saleh and M. C. Teich, *Fundamentals of Photonics*, vol. 45, no. 11. Wiley-Interscience, 2007, p. 1177.

[8] A. G. Podoleanu, “Unbalanced versus balanced operation in an optical coherence tomography system,” *Applied Optics*, vol. 39, no. 1, pp. 173–182, 2000.

[9] A. Chennu, “Optical Coherence Tomography,” *Erasmus*, 2008.

[10] M. Choma, M. Sarunic, C. Yang, and J. Izatt, “Sensitivity advantage of swept source and Fourier domain optical coherence tomography,” *Optics Express*, vol. 11, no. 18, pp. 2183–2189, 2003.

[11] Mark E. Brezinski, *Optical Coherence Tomography: Principles And Applications* . USA: Elsevier Inc.

[12] P. Targowski, “Complex spectral OCT in human eye imaging in vivo,” *Optics Communications*, vol. 229, no. 1–6, pp. 79–84, 2004.

[13] S. Yun, G. Tearney, J. De Boer, N. Iftimia, and B. Bouma, “High-speed optical frequency-domain imaging,” *Optics Express*, vol. 11, no. 22, pp. 2953–2963, 2003.

[14] M. Wojtkowski, A. Kowalczyk, R. Leitgeb, and A. F. Fercher, “Full range complex spectral optical coherence tomography technique in eye imaging,” *Optics Letters*, vol. 27, no. 16, pp. 1415–7, 2002.

[15] D. Merino, C. Dainty, A. Bradu, and A. G. Podoleanu, “Adaptive optics enhanced simultaneous en-face optical coherence tomography and scanning laser ophthalmoscopy,” *Optics Express*, vol. 14, no. 8, pp. 3345–3353, 2006.

[16] D. L. Marks, A. L. Oldenburg, J. J. Reynolds, and S. A. Boppart, “Digital algorithm for dispersion correction in and stratified media,” *Applied Optics*, 2003.

[17] M. H. Lang, “Optical Coherence Tomography: System Design and Noise Analysis,” *ReportRiso Natl Lab*, vol. 1278, no. July, p. 65, 2001.

[18] R. S. Caprari, A. S. Goh, and E. K. Moffatt, “Noise and speckle reduction in synthetic aperture radar imagery by nonparametric Wiener filtering,” *Applied Optics*, vol. 39, no. 35, pp. 6633–6640, 2000.

[19] S. Sudha, G. R. Suresh, and R. Sukanesh, “Speckle noise reduction in ultrasound images by Wavelet thresholding based on weighted variance,” *International Journal*, vol. 1, no. 1, pp. 7–12, 2009.

[20] M. Mansourpour, M. A. Rajabi, S. Filtering, and A. Filter, “Effects and performance of speckle noise reduction filters on active radar and sar images,” *Image Rochester NY*, vol. 2, no. 1/W41, pp. 1 – 6, 2000.

[21] J. M. Schmitt, S. H. Xiang, and K. M. Yung, “Speckle in Optical Coherence Tomography,” *Journal of Biomedical Optics*, vol. 4, no. 1, p. 95, 1999.

[22] A. Ozcan, A. Bilenca, A. E. Desjardins, B. E. Bouma, and G. J. Tearney, “Speckle reduction in optical coherence tomography images using digital filtering,” *Journal of the Optical Society of America. A, Optics, image science, and vision*, vol. 24, no. 7, pp. 1901–10, Jul. 2007.

[23] J. W. Goodman, “Some fundamental properties of speckle,” *Journal of the Optical Society of America*, vol. 66, no. 11, pp. 1145–1150, 1976.

[24] S.-W. Huang, S.-Y. Yang, W.-C. Huang, H.-M. Chiu, and C.-W. Lu, “Study on image feature extraction and classification for human colorectal cancer using optical coherence tomography,” *Techniques*, vol. 8091, p. 80911Y–80911Y–4, 2011.

[25] A. Pizurica, L. Jovanov, B. Huysmans, V. Zlokolica, P. De Keyser, F. Dhaenens, and W. Philips, “Multiresolution denoising for optical coherence tomography: a review and evaluation,” *Current Medical Imaging Reviews*, vol. 4, no. 4, pp. 270–284, 2008.

[26] Y. Wu, D. Clarke, A. Mathew, I. Nicoud, and X. Li, “Automated segmentation of tissue structures in optical coherence tomography data,” *Journal of Biomedical Optics*, vol. 16, no. 3, p. 034046, 2011.

[27] A. Wong, A. Mishra, K. Bizheva, and D. a Clausi, “General Bayesian estimation for speckle noise reduction in optical coherence tomography retinal imagery,” *Optics express*, vol. 18, no. 8, pp. 8338–52, Apr. 2010.

[28] J.-T. Oh and B.-M. Kim, “Artifact removal in complex frequency domain optical coherence tomography with an iterative least-squares phase-shifting algorithm,” *Applied optics*, vol. 45, no. 17, pp. 4157–64, Jun. 2006.

[29] J. Ho, D. P. E. Castro, L. C. Castro, Y. Chen, J. Liu, C. Mattox, C. Krishnan, J. G. Fujimoto, J. S. Schuman, and J. S. Duker, “Clinical assessment of mirror artifacts in spectral-domain optical coherence tomography,” *Investigative ophthalmology & visual science*, vol. 51, no. 7, pp. 3714–20, Jul. 2010.

[30] S. Ortiz, D. Siedlecki, L. Remon, and S. Marcos, “Optical coherence tomography for quantitative surface topography,” *Applied optics*, vol. 48, no. 35, pp. 6708–15, Dec. 2009.

[31] Y. Li, “Beam deflection and scanning by two-mirror and two-axis systems of different architectures: a unified approach,” *Applied Optics*, vol. 47, no. 32, pp. 5976–5985, 2008.

[32] V. Westphal, A. Rollins, S. Radhakrishnan, and J. Izatt, “Correction of geometric and refractive image distortions in optical coherence tomography applying Fermat’s principle.,” *Optics express*, vol. 10, no. 9, pp. 397–404, May 2002.

[33] W. Drexler and J. G. Fujimoto, *Optical coherence tomography: technology and applications*, vol. 7156, no. May. Springer, 2008, pp. 715606–715606–9.

[34] B. J. Davis, T. S. Ralston, D. L. Marks, S. A. Boppart, and P. S. Carney, “Autocorrelation artifacts in optical coherence tomography and interferometric synthetic aperture microscopy,” *Optics Letters*, vol. 32, no. 11, pp. 1441–1443, 2007.

[35] A. Ozcan, M. J. Digonnet, and G. S. Kino, “Minimum phase function-based processing in frequency domain optical coherence tomography systems,” *Journal of the Optical Society of America A*, vol. 23, no. 7, pp. 1669–1677, 2006.

[36] A. Ozcan, M. J. F. Digonnet, and G. S. Kino, “Coherence tomography systems,” *America*, vol. 23, no. 7, pp. 1669–1677, 2006.

[37] S. C. Sekhar, R. A. Leitgeb, A. H. Bachmann, and M. Unser, “Logarithmic transformation technique for exact signal recovery in frequency-domain optical-coherence tomography,” *Techniques*, vol. 6627, pp. 1–6, 2007.

[38] M. J. Everett, K. Schoenenberger, B. W. Colston, and L. B. Da Silva, “Birefringence characterization of biological tissue by use of optical coherence tomography,” *Optics Letters*, vol. 23, no. 3, pp. 228–230, 1998.

[39] B. Park, M. Pierce, B. Cense, and J. De Boer, “Real-time multi-functional optical coherence tomography,” *Optics Express*, vol. 11, no. 7, pp. 782–793, 2003.

[40] T. Fabritius, S. Makita, Y. Hong, R. Myllylä, and Y. Yasuno, “Automated retinal shadow compensation of optical coherence tomography images,” *Journal of Biomedical Optics*, vol. 14, no. 1, p. 010503, 2009.

[41] M. J. A. Girard, N. G. Strouthidis, C. R. Ethier, and J. M. Mari, “Shadow removal and contrast enhancement in optical coherence tomography images of the human optic nerve head,” *Investigative Ophthalmology & Visual Science*, vol. 52, no. 10, pp. 7738–48, 2011.

[42] R. J. Zawadzki, A. R. Fuller, S. S. Choi, D. F. Wiley, B. Hamann, and J. S. Werner, “Correction of motion artifacts and scanning beam distortions in 3D ophthalmic optical coherence tomography imaging,” *Proceedings of SPIE*, vol. 6426, pp. 642607–642607–11, 2007.

[43] S. H. Yun, G. Tearney, J. De Boer, and B. Bouma, “Motion artifacts in optical coherence tomography with frequency-domain ranging,” *Optics Express*, vol. 12, no. 13, pp. 2977–2998, 2004.

[44] D. Sacchet, M. Brzezinski, J. Moreau, P. Georges, and A. Dubois, “Motion artifact suppression in full-field optical coherence tomography,” *Applied Optics*, vol. 49, no. 9, pp. 1480–1488, 2010.

[45] R. De Kinkelder, J. Kalkman, D. J. Faber, O. Schraa, P. H. B. Kok, F. D. Verbraak, and T. G. Van Leeuwen, “Heartbeat-induced axial motion artifacts in optical coherence tomography measurements of the retina,” *Investigative Ophthalmology & Visual Science*, vol. 52, no. 6, pp. 3908–3913, 2011.

[46] A. Podoleanu, I. Charalambous, L. Plesea, A. Dogariu, and R. Rosen, “Correction of distortions in optical coherence tomography imaging of the eye,” *Physics in Medicine and Biology*, vol. 49, no. 7, pp. 1277–1294, 2004.

[47] Y. M. Liew, R. a McLaughlin, F. M. Wood, and D. D. Sampson, “Reduction of image artifacts in three dimensional optical coherence tomography of skin in vivo,” *Journal of biomedical optics*, vol. 16, no. 11, p. 116018, Nov. 2011.

[48] J. Welzel, C. Reinhardt, E. Lankenau, C. Winter, and H. H. Wolff, “Changes in function and morphology of normal human skin: evaluation using optical coherence tomography,” *The British journal of dermatology*, vol. 150, no. 2, pp. 220–225, 2004.

[49] M. Mogensen, H. A. Morsy, L. Thrane, and G. B. E. Jemec, “Morphology and epidermal thickness of normal skin imaged by optical coherence tomography,” *Dermatology Basel Switzerland*, vol. 217, no. 1, pp. 14–20, 2008.

[50] M. D. Kulkarni, C. W. Thomas, and J. A. Izatt, “Image enhancement in optical coherence tomography using deconvolution,” *Electronics Letters*, vol. 33, no. 16, 1997.

[51] Y. Liu, Y. Liang, G. Mu, and X. Zhu, “Deconvolution methods for image deblurring in optical coherence tomography.,” *Journal of the Optical Society of America. A, Optics, image science, and vision*, vol. 26, no. 1, pp. 72–7, Jan. 2009.

[52] Y. Liu, Y. Liang, G. Mu, and X. Zhu, “Two-dimensional image sharpening in optical coherence tomography by deconvolution,” *Proceedings of SPIE*, vol. 6826, no. 2007, pp. 682608–682608–9, 2007.

[53] K. Wang, Z. Ding, M. Chen, C. Wang, T. Wu, and J. Meng, “Deconvolution with fall-off compensated axial point spread function in spectral domain optical coherence tomography,” *Optics Communications*, vol. 284, no. 12, pp. 3173–3180, Jun. 2011.

[54] I. Jan, C. Chiu, E. Tien, and G. Jan, “Study on Deconvolution Algorithms for Optical Coherent Tomography,” vol. 23, no. 2, pp. 73–77, 2003.

[55] E. Lam and J. Goodman, “Iterative statistical approach to blind image deconvolution,” *Journal of the Optical Society of America A*, vol. 17, no. 7, pp. 1177–84, 2000.

[56] Q. Wu, F. A. Merchant, and K. R. Castleman, *Microscope image processing*, vol. 57, no. 5. Academic Press, 2008, p. 548.

[57] G. R. Ayers and J. C. Dainty, “Iterative Blind Deconvolution Method and its Application,” *Optical Letters*, vol. 13, no. 7, pp. 547–549, 1988.

[58] K. Banaszek, A. S. Radunsky, and I. a. Walmsley, “Blind dispersion compensation for optical coherence tomography,” *Optics Communications*, vol. 269, no. 1, pp. 152–155, Jan. 2007.

[59] T. S. Ralston, D. L. Marks, F. Kamalabadi, and S. a Boppart, “Deconvolution methods for mitigation of transverse blurring in optical coherence tomography,” *IEEE transactions on image processing : a publication of the IEEE Signal Processing Society*, vol. 14, no. 9, pp. 1254–64, Sep. 2005.

[60] G. Kail, C. Novak, B. Hofer, and F. Hlawatsch, “Blind Monte Carlo detection-estimation method for optical coherence tomography,” *IEEE International Conference on Acoustics Speech and Signal Processing (2009)*, no. 1, pp. 493–496, 2009.

[61] I. Hsu, C. Sun, C. Lu, C. C. Yang, C. Chiang, and C. Lin, “manipulation and a retrieval algorithm in optical coherence tomography,” *Applied Optics*, vol. 42, no. 2, pp. 227–234, 2003.

[62] E. Bousi, I. Charalambous, and C. Pitris, “Modulated deconvolution for resolution improvement in Fourier Domain Optical Coherence Tomography,” *Biomedicine*, vol. 7889, pp. 1–6, 2011.

[63] Y. Yasuno, J.-I. Sugisaka, Y. Sando, Y. Nakamura, S. Makita, M. Itoh, and T. Yatagai, “Non-iterative numerical method for laterally superresolving Fourier domain optical coherence tomography,” *Optics express*, vol. 14, no. 3, pp. 1006–20, Feb. 2006.

[64] J. Schmitt, “Restoration of Optical Coherence Images of Living Tissue Using the CLEAN Algorithm,” *Journal of Biomedical Optics*, vol. 3, no. 1, pp. 66–75, 1998.

[65] P. D. Woolliams, R. a Ferguson, C. Hart, A. Grimwood, and P. H. Tomlins, “Spatially deconvolved optical coherence tomography,” *Applied optics*, vol. 49, no. 11, pp. 2014–21, Apr. 2010.

[66] G. Liu, S. Yousefi, Z. Zhi, and R. K. Wang, “Automatic estimation of point-spread-function for deconvoluting out-of-focus optical coherence tomographic images using information entropy- based approach,” *Biomedicine*, vol. 19, no. 19, pp. 18135–18148, 2011.

[67] S. Pal, D. Sheet, A. Chakraborty, and J. Chatterjee, “Comparative Evaluation of Speckle Reduction Algorithms in Optical Coherence Tomography,” *Engineering*, pp. 0–3, 2010.

[68] J. M. Schmitt, S. H. Xiang, and K. M. Yung, “Speckle in optical coherence tomography,” *Library*, vol. 4, no. 1, pp. 95–105, 1999.

[69] M. Bashkansky and J. Reintjes, “Statistics and reduction of speckle in optical coherence tomography,” *Optics letters*, vol. 25, no. 8, pp. 545–7, Apr. 2000.

[70] J. Rogowska and M. E. Brezinski, “Evaluation of the adaptive speckle suppression filter for coronary optical coherence tomography imaging,” *IEEE transactions on medical imaging*, vol. 19, no. 12, pp. 1261–6, Dec. 2000.

[71] D. C. Adler, T. H. Ko, and J. G. Fujimoto, “Speckle reduction in optical coherence tomography images by use of a spatially adaptive wavelet filter,” *Optics letters*, vol. 29, no. 24, pp. 2878–80, Dec. 2004.

[72] D. L. Marks, T. S. Ralston, and S. a Boppart, “Speckle reduction by I-divergence regularization in optical coherence tomography,” *Journal of the Optical Society of America. A, Optics, image science, and vision*, vol. 22, no. 11, pp. 2366–71, Nov. 2005.

[73] P. Puvanathasan and K. Bizheva, “Speckle noise reduction algorithm for optical coherence tomography based on interval type II fuzzy set.,” *Optics express*, vol. 15, no. 24, pp. 15747–58, Nov. 2007.

[74] G. J. Tearney, B. E. Bouma, and J. G. Fujimoto, “High speed phase and group-delay scanning with a grating-based phase control delay line,” *Optics Letters*, vol. 22, no. 23, pp. 1811–1813, 1997.

[75] I. Forward and B. S. Data, “Inverse scattering, dispersion, and speckle in optical coherence tomography,” *Transform*, no. i, pp. 119–146, 2008.

[76] E. Brinkmeyer and R. Ulrich, “High-resolution OCDR in dispersive waveguides,” *Electronics Letters*, vol. 26, no. 6, p. 413, 1990.

[77] A. Kohlhaas, C. Fromchen, and E. Brinkmeyer, “Data corrected by a numerical algorithm,” *Lightwave*, vol. 9, no. 11, pp. 1493–1502, 1991.

[78] J. F. de Boer, C. E. Saxer, and J. S. Nelson, “Stable carrier generation and phase-resolved digital data processing in optical coherence tomography,” *Applied optics*, vol. 40, no. 31, pp. 5787–90, Nov. 2001.

[79] A. Fercher, C. Hitzenberger, M. Sticker, R. Zawadzki, B. Karamata, and T. Lasser, “Numerical dispersion compensation for partial coherence interferometry and optical coherence tomography,” *Optics express*, vol. 9, no. 12, pp. 610–5, Dec. 2001.

[80] M. Wojtkowski, V. Srinivasan, T. Ko, J. Fujimoto, A. Kowalczyk, and J. Duker, “Ultrahigh resolution, high speed, Fourier domain optical coherence tomography and methods for dispersion compensation,” *Optics Express*, vol. 12, no. 11, pp. 2404–2422, 2004.

[81] N. Lippok, P. Nielsen, and F. Vanholsbeeck, "Dispersion compensation in spectral domain optical coherence tomography," *Techniques*, vol. 8091, no. 2, pp. 2–5, 2011.

[82] K. Takada, "Noise in optical low-coherence reflectometry," *IEEE Journal of Quantum Electronics*, vol. 34, no. 7, pp. 1098–1108, 1998.

[83] A. M. Rollins and J. A. Izatt, "Optimal interferometer designs for optical coherence tomography," *Optics Letters*, vol. 24, no. 21, pp. 1484–1486, 1999.

[84] B. Saleh, *Photoelectron statistics with applications to spectroscopy and optical communication*. Springer, 1978, vol. 1, 1978. .

[85] J. Rice, "On generalized shot noise," *Adv. Appl*, vol. Probab. 9, pp. 553–565, 1977.

[86] B. Picinbono, "Photoelectron Shot Noise," *Journal of Mathematical Physics*, vol. 11, no. 7, p. 2166, 1970.

[87] L. Mandel and E. Wolf, *Optical Coherence and Quantum Optics*, vol. 64, no. 11. Cambridge University Press, 1995, p. 1192.

[88] B. M. Oliver, "Thermal and quantum noise," *Proceedings of the IEEE*, vol. 53, no. 5, pp. 436–454, 1965.

[89] M. I. Skolnik, *Radar Handbook*, vol. 7, no. 1. McGraw-Hill, 1990, p. 1328.

[90] G. Turin, "An introduction to matched filters," *IEEE Transactions on Information Theory*, vol. 6, no. 3, pp. 311–329, 1960.

[91] C. W. Helstrom, *Elements of Signal Detection and Estimation*, no. 3. Prentice Hall, 1995, pp. 630–635.

[92] S. Haykin, *Adaptive filter theory*, vol. 29, no. 2. Prentice Hall, 2003, p. 997.

[93] P. J. Rousseeuw and G. Molenberghs, "Transformation of non positive semi-definite correlation matrices," *Communications in Statistics, Theory and Methods*, vol. 4, no. 22, pp. 965-984, 1993.

Appendix A

A.1 SNR relation of input and output of envelope detector

An electronic configuration that is usually applied to obtain the envelope of a signal is shown in Figure A.1. In general, this is similar to the electronic configuration that is used for demodulation of AM radio signals [89].

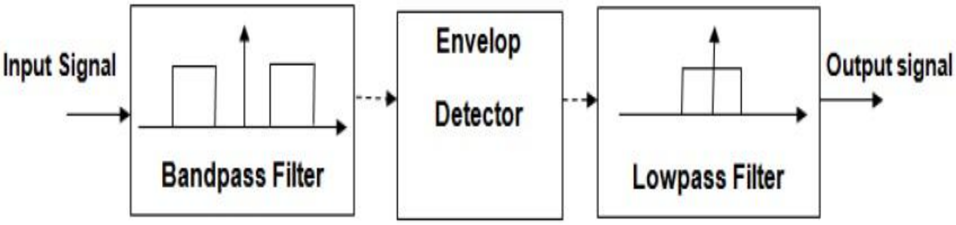

Figure A.1: Envelope detector (demodulator) block diagram.

As this Figure shows, the envelope detector (demodulator) is preceded by a band-pass filter and is followed by a low-pass filter. There is always a loss in the values of the SNR at the output of demodulator in compare to the SNR values at its input, named as the loss factor [89]. In this appendix, we write the mathematical relationship that exists between the input SNR and the output SNR of an envelope Detector [89]. The SNR is defined as the ratio of output power due to the desired signal to the output power due to the noise [89],

$$SNR = \frac{P_{sig}}{P_{Noise}}, \tag{A.1}$$

where P_{sig} denotes the power of desired signal and P_{Noise} is the power of noise. To obtain the loss factor of an envelope detector, first the power of desired signal and noise at the input and output of envelope detector (demodulator) are obtained. Suppose that the Amplitude Modulated (AM) signal $s_i(t)$ is denoted by,

$$s_i(t) = A[1 + m(t)]cos(\omega_c t) = A[1 + m(t)]cos(2\pi f_c t)$$

$$s_i(t) = Acos(\omega_c t) + Am(t)cos(\omega_c t), \qquad \text{(A.2)}$$

where $m(t)$ is the amplitude modulate term, therefore, the power of the carrier signal, $Acos(\omega_c t)$, is obtained by,

$$P_c = \frac{A^2}{2}. \qquad \text{(A.3)}$$

In addition, $Am(t)cos(2\pi f_c t)$ term determines the side band signal, that has the power of,

$$P_{SB} = \frac{A^2}{2}\overline{m^2(t)}, \qquad \text{(A.4)}$$

where, $\overline{m^2(t)}$ is the time average of the square of the amplitude modulate term, $m(t)$. Using Eq. (A.3) and Eq. (A.4), the total power of signal, $s_i(t)$, is given by,

$$P_{s_i} = P_c + P_{SB} = \frac{A^2}{2}(1 + \overline{m^2(t)}\,)\,. \qquad \text{(A.5)}$$

The noise of the system is represented using,

$$n(t) = n_c(t)cos(\omega_c t) - n_s(t)sin(\omega_c t), \qquad \text{(A.6)}$$

and the power spectral densities,$n_c(t)$ and $n_s(t)$ are:

$$G_{n_c}(f) = G_{n_s}(f) = G_n(f_c - f) + G_n(f_c + f). \qquad \text{(A.7)}$$

These power spectral densities, $G_{n_c} = G_{n_s} = \eta$, are shown by Figure A.2.

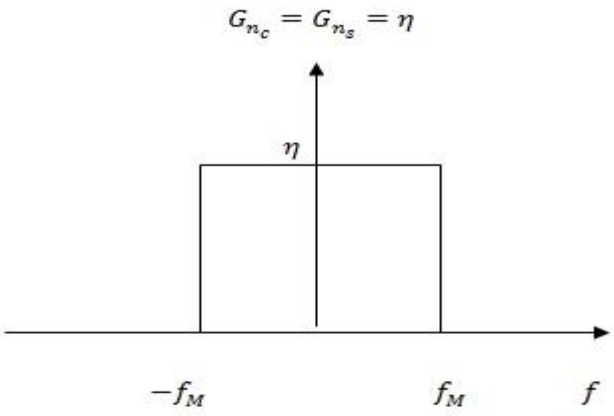

Figure A.2: Power spectral densities of $\boldsymbol{n_c(t)}$ and $\boldsymbol{n_s(t)}$.

The power spectral density of noise is equal to the $\frac{\eta}{2}$ after passing through the band-pass filter [89] and is shown by Figure A.3.

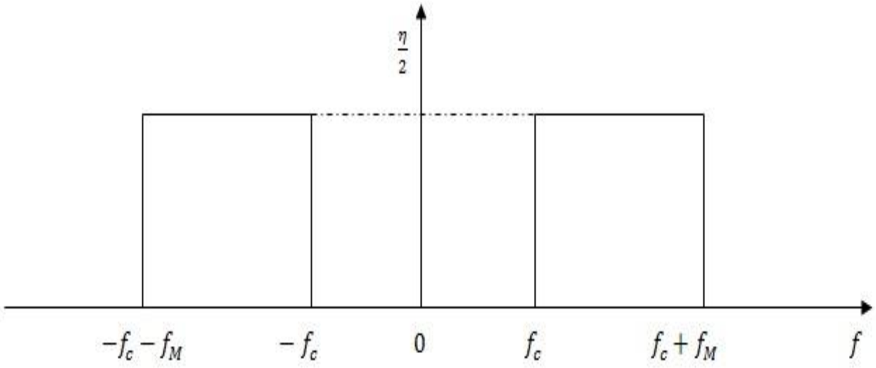

Figure A.3: Power spectral densities of $\boldsymbol{n_c(t)}$ and $\boldsymbol{n_s(t)}$ after passing through a band-pass filter.

The power spectral density of noise, $P_{n_{input}}$, at the input of envelope detector and after band-pass filtering is obtained by,

$$P_{n_{input}} = 2f_M \times \frac{\eta}{2} = \eta f_M. \tag{A.8}$$

Using Eq. (A.5) and Eq. (A.8), the value of SNR at the input of envelope detector is obtained by [89],

$$SNR_{Env_{input}} = \frac{P_{s_{Env-input}}}{P_{n_{Env-input}}} = \frac{\frac{A^2}{2}(1+\overline{m^2(t)})}{\eta f_M}. \tag{A.9}$$

The input signal of the detector,s_{input}, is the sum of the desired signal, s_i and the noise term n ,

$$s_{input}(t) = s_i(t) + n(t) =$$

$$A[1+m(t)]cos(\omega_c t) + n_c(t)cos(\omega_c t) - n_s(t)sin(\omega_c t) =$$

$$\{A[1+m(t)]) + n_c(t)\}\ cos(\omega_c t) - n_s(t)sin(\omega_c t), \tag{A.10}$$

where, A is the amplitude of the carrier signal, $Acos(\omega_c t)$.The output of envelope detector just prior to the low-pass filtering is given by,

$$s_{Env}(t) = \sqrt{\{A[1+m(t)]) + n_c(t)\}^2 + {n_s}^2(t)} =$$

$$\sqrt{(A^2[1+m(t)]^2 + 2A[1+m(t)]n_c(t) + {n_c}^2(t) + {n_s}^2(t)}. \tag{A.11}$$

Since the distribution of $n_c(t)$ and $n_s(t)$ are Gaussian, if the standard deviations of $n_c(t)$ and $n_s(t)$ be much smaller than the carrier amplitude A, we have [91],

$$\sqrt{\overline{{n_c}^2(t)}} \leq A \Longrightarrow n_c(t) \leq A$$

$$\sqrt{\overline{{n_s}^2(t)}} \leq A \Longrightarrow n_s(t) \leq A\ . \tag{A.12}$$

Using this, noise-noise terms in the Eq. (A.11) can be dropped, leaving us with the following approximation,

$$s_{Env}(t) = \sqrt{(A^2[1+m(t)]^2 + 2A[1+m(t)]n_c(t) + {n_c}^2(t) + {n_s}^2(t)} \cong$$

$$\sqrt{A^2[1+m(t)]^2 + 2A[1+m(t)]n_c(t)} =$$

$$A[1+m(t)]\sqrt{1+\frac{2n_c(t)}{A[1+m(t)]}}. \qquad \text{(A.13)}$$

Using the mathematical approximation of,

$$\sqrt{1+x} \cong 1+\frac{x}{2}, \qquad \text{(A.14)}$$

we can simplify the Eq. (A.13) as,

$$s_{Env}(t) \cong \quad A[1+m(t)] + \ n_c(t). \qquad \text{(A.15)}$$

The signal power at the output of the envelope detector and after the low-pass filtering and by neglecting the DC term A is equal to the,

$$P_{s_{Env-output}} = A^2\overline{m^2(t)}\,. \qquad \text{(A.16)}$$

In Figure A.2, it was shown that the spectral density of $n_c(t)$ is equal to the,η, therefore the power of noise at the output of envelope detector and after low-pass filter is obtained as,

$$P_{n_{Env-output}} = 2\eta f_M. \qquad \text{(A.17)}$$

Therefore, the SNR at the output of envelope detector is be given by,

$$SNR_{Env_{Ouput}} = \frac{P_{s_{Env-output}}}{P_{n_{Env-output}}} = \frac{A^2\overline{m^2(t)}}{2\eta f_M}. \qquad \text{(A.18)}$$

Using Eq. (A.9) and Eq. (A.18), the relation between the SNR values at the input and output of an envelope detector is obtained,

$$\gamma = \frac{\overline{m^2(t)}}{1+\overline{m^2(t)}}, \qquad \text{(A.19)}$$

Appendix B

Design Depth dependent matched filter code

```
clear all;
clc;
colormap(jet)
close all;
% ------Load Data------------------------------
cd 'C:\.......’;
[no_a_scan_pixels, no_a_scans, no_images] = size(rabit3interf);
a_scans = rabit3interf(500:2500,:,1:no_images);
[no_a_scan_pixels, no_a_scans, no_images] = size(a_scans);
%---------------------Construct the Envelope of photocurrents--------------
for k = 1 : no_images
        a_scans(:,:,k) = abs(a_scans(:,:,k) + sqrt(-1) *
hilbert(a_scans(:,:,k)));
end

a_scans_before_thresh=a_scans;
a_scans=a_scans./max(max(max(a_scans))); %normalize OCT images-------------

%------Threshold all OCT images-----------------------------------
for k = 1 : no_images
    max_image_value = max(max(a_scans(:,:,k)));
   for j = 1 : no_a_scans
        for l = 1 : no_a_scan_pixels
            if (a_scans(l,j,k)/max_image_value < 0.01)
                a_scans(l,j,k) = 0;
            end
        end
    end
end

%------ Determine selected OCT image-------------------
k = 3;
initial_image = a_scans(:,:,k);

% -----obtain the average of all images-----------------------
avg_image = mean(a_scans,3); % average on third dimension

%-----Process A scans----------------------------------------
a_scans_filtered = zeros(no_a_scan_pixels, no_a_scans, no_images);
for j = 1:no_a_scans
    avg_a_scan = avg_image(:,j);

% obtain the covariance of selected a_scan from all images
    a_scan_cov_matrix = zeros(no_a_scan_pixels);
    a_scan_cor_matrix = zeros(no_a_scan_pixels);
for kk = 1 : no_images
 a_scan_cor_matrix = a_scan_cor_matrix + a_scans(:,j,kk) *
 a_scans(:,j,kk)'; % correlation matrix
```

```
end
a_scan_cov_matrix = (a_scan_cor_matrix/no_images) - (avg_a_scan *
avg_a_scan');  % subtract outer product of mean


% --------Obtain and plot average A scan power-----------------------------
    avg_a_scan_power = avg_a_scan .* avg_a_scan;
    size(avg_a_scan_power);
% -------Obtain Noise Power------------------------------------------------
    a_scan_noise_power = diag(a_scan_cov_matrix,0);

% -------plot signal to noise ratio----------------------------------------
    snr_dB = 10 * log10(avg_a_scan_power ./ a_scan_noise_power);

% -------decide on an odd window size by some% method
    window_size =7;
    half_window_size = floor(window_size/2);
    count1=0; %count number of windows that are full Rank
    count2=0; %count number of windows that are not full Rank

 for i = half_window_size + 1 : (no_a_scan_pixels - half_window_size)
    window_avg_a_scan = avg_a_scan(i - half_window_size : i +
half_window_size);
    norm_window_avg_a_scan=norm(window_avg_a_scan); %Calculate norm of signal
inside window
    window_cov_matrix1 = a_scan_cov_matrix(i - half_window_size : i +
half_window_size, i - half_window_size : i + half_window_size);
    [Q1 D1]=eig(window_cov_matrix1); %Eigen decomposition of windows
Covariance Matrix
    D1=abs(D1); %make absoulute value of Eigen-Values
    window_cov_matrix=Q1*D1*Q1'; %Reconstruct windows Covariance matrix using
new Eigen-Values
    rank_values(i) = rank(window_cov_matrix);

 if (rank_values(i)== window_size)
    eigen_rhs = window_cov_matrix\ window_avg_a_scan;
    mahalanobis_dist =window_avg_a_scan' * eigen_rhs ;
    filter = (1 / sqrt(mahalanobis_dist)) * eigen_rhs;
%   norm_values(i) = norm(filter);
   for kk = 1 : no_images
       a_scans_filtered(i,j, kk) = a_scans(i - half_window_size : i +
half_window_size,j ,kk)'*  filter;
   end
    count1=count1+1;

 elseif (rank_values(i)~=window_size && norm_window_avg_a_scan~=0 )
    window_cov_matrix=eye(window_size); %Consider Identity Matrix instead of
Covariance Matrix
    eigen_rhs = window_cov_matrix\window_avg_a_scan;
    mahalanobis_dist =window_avg_a_scan' * eigen_rhs;
    filter = (1 / sqrt(mahalanobis_dist)) * eigen_rhs;
   %norm_values(i) = norm(filter);
   count2=count2+1;
   for kk = 1 : no_images
```

```
        a_scans_filtered(i,j, kk) = a_scans(i - half_window_size : i +
half_window_size,j ,kk)'*  filter;
    end
end
 end
rank_check(j,:)=rank_values;
size(find(rank_check(j,:)== window_size));
j
end
save ('filtered_data_Win_7', 'a_scans_filtered')
```

SNR and CNR analysis of averaged depth-scan

```
clear all;
clc;
colormap(jet)
close all
% --------------------------------------------------------------------------
cd 'C:\Users\Ameneh\Documents\MATLAB\OCT-Data\research-
thesis\MyProject_Mfiles-October2011\New_test11_4_November-Results\Sherif
code-January-2012\Matched filter\New_Data_Analysis\Rabbit';

%load data
load rabit3interf;
load filtered_data_Win_19
[no_a_scan_pixels, no_a_scans, no_images] = size(rabit3interf);

a_scans = rabit3interf;
a_scans = rabit3interf(500:2500,:,1:no_images);

%obtain data size
[no_a_scan_pixels, no_a_scans, no_images] = size(a_scans);

mm_per_pixel = 4/3700;

total_depth_mm = no_a_scan_pixels * mm_per_pixel;

vertical_scale = linspace (0, total_depth_mm, no_a_scan_pixels);
horizontal_scale = linspace(0, no_a_scans);

%obtain envelope
for k = 1 : no_images
        a_scans(:,:,k) = abs(a_scans(:,:,k) + sqrt(-1) *
hilbert(a_scans(:,:,k)));
end

% Threshold all OCT images
for k = 1 : no_images
    max_image_value = max(max(a_scans(:,:,k)));
    for j = 1 : no_a_scans
        for l = 1 : no_a_scan_pixels
            if (a_scans(l,j,k)/max_image_value < 0.01)
```

```
                a_scans(1,j,k) = 0;
            end
        end
    end


end
 a_scans1= a_scans;

% %scale OCT image
for k = 1 : no_images

    max_b=max(max(a_scans(:,:,k)));
    max_f=max(max(a_scans_filtered(:,:,k)));
    scale=max_f/max_b;
    a_scans(:,:,k)=scale.*a_scans(:,:,k);

end

% Select image number 3 and an A-scan to process
k=3
j = 300

% obtain the average of selected a_scan from all images
avg_image = mean(a_scans,3); % average on third dimension
avg_a_scan = avg_image(:,j);

% Display thresholded and normalized selected OCT image
scrsz=[50,50,600,600];
figure('Position',scrsz);
initial_image = a_scans(:,:,k);
subplot(3,2,1), imagesc(horizontal_scale, vertical_scale, avg_image);
xlabel('Pixels')
ylabel('Imaging depth (mm)')
title('(a) Averaged OCT image')
axis tight
%  cb = colorbar;
pause

subplot(3,2,2), plot(vertical_scale, avg_a_scan)
xlabel(' Imaging depth (mm)')
ylabel('Pixel value (a.u.)')
axis tight
title('(b) Averaged depth-scan envelope')
grid on
pause

%Obtain and plot the variance of averaged A-scan in windows of size three
window_size =3;
half_window_size = floor(window_size/2);
Var_value=zeros(size(a_scans,1),1);
for i = half_window_size + 1 : (no_a_scan_pixels - half_window_size)
    window_avg_a_scan = avg_a_scan(i - half_window_size : i +
half_window_size);
```

```
    Var_value(i,1)=mean(window_avg_a_scan.^2)-(mean(window_avg_a_scan)).^2;
%obtain variance of averaged A-scan in window of size 3 pixels using:
Var=E[s^2]-(E[s])^2
end

subplot(3,2,5), plot(vertical_scale,Var_value)
axis ([0 max(vertical_scale) min(Var_value)
max(Var_value)+0.1*max(Var_value)])
xlabel('Imaging depth (mm)')
ylabel('Contrast (a.u.)')
title('(e)Averaged depth-scan contrast')
grid on

% obtain the covariance of selected a_scan from all images
a_scan_cor_matrix = zeros(no_a_scan_pixels);
a_scan_cov_matrix = zeros(no_a_scan_pixels);
for kk = 1 : no_images
        a_scan_cor_matrix = a_scan_cor_matrix + a_scans(:,j,kk) *
a_scans(:,j,kk)'; % obtain correlation matrix
end
a_scan_cov_matrix = (a_scan_cor_matrix/no_images) - (avg_a_scan *
avg_a_scan');  % obtain covariance matrix

%plot covariance matrix
% subplot(2,2,3), image(a_scan_cov_matrix);
% cb = colorbar;
pause

% Obtain and plot average A scan power
avg_a_scan_power = avg_a_scan .* avg_a_scan;
size(avg_a_scan_power)

% subplot(3,1,2), plot(avg_a_scan_power)
% axis tight
% title('Average power of A scan envelope')
% pause

% plot variance of selected A-scan
a_scan_noise_power = diag(a_scan_cov_matrix,0);
subplot(3,2,3), plot(vertical_scale,a_scan_noise_power);
title('(c)Averaged depth-scan noise power')
xlabel('Imaging depth (mm)')
ylabel('Pixel value (a.u.)')
axis tight
grid on
pause

% obtain and plot signal to noise ratio
snr_dB = 10 * log10(avg_a_scan_power ./ a_scan_noise_power);

subplot(3,2,4), plot(vertical_scale, snr_dB)
xlabel('Imaging depth (mm)')
ylabel('SNR (dB)')
title('(d)Averaged depth-scan SNR')
axis ([0 max(vertical_scale) -10 20])
```

```
grid on

[x y]=find(isnan(snr_dB));
snr_dB(x,y)=0;
mean(snr_dB)

%obtain CNR
% Figure_merit is CNR
Figure_merit=Var_value./ a_scan_noise_power;
Figure_merit(isnan(Figure_merit))=0;
Figure_merit(isinf(Figure_merit))=0;
subplot(3,2,6), plot(vertical_scale,Figure_merit)
axis ([0 max(vertical_scale) min(Figure_merit)
max(Figure_merit)+0.1*max(Figure_merit)])
xlabel('Imaging depth (mm)')
ylabel('CNR (a.u.)')
title('(f) Averaged depth-scan CNR')
grid on
cd 'C:\Users\Ameneh\Documents\MATLAB\OCT-Data\research-
thesis\MyProject_Mfiles-October2011\New_test11_4_November-Results\Sherif
code-January-2012\Matched filter\New_Data_Analysis\Rabbit\Win-3-Var-
Calc\Figure_of_Merit\new-Agust18'
%save data
save ('snr_dB', 'snr_dB')
save('avg_image','avg_image')
save('Var_value','Var_value')
save('Figure_merit_win19','Figure_merit')
m=Figure_merit(find(Figure_merit~=0));
mean_Figure_merit=mean(m)
```

SNR and CNR analysis after matched filtering

```
clear all;
clc;
colormap(jet)
close all
% -----------------------------------------------------------------------
cd 'C:\....’;

%load data
load filtered_data_Win_19
load Figure_merit_win19
plot(Figure_merit)
pause
Figure_merit_before_filt=Figure_merit;
load Var_value
Var_old=Var_value;
load snr_dB
snr_dB_before_Filt=snr_dB;
[no_a_scan_pixels, no_a_scans, no_images] = size(a_scans_filtered);
 %----------------------------------------------------------------------
a_scans = a_scans_filtered;
mm_per_pixel = 4/3700;
```

```
total_depth_mm = no_a_scan_pixels * mm_per_pixel;
vertical_scale = linspace (0, total_depth_mm, no_a_scan_pixels);
horizontal_scale = linspace(0, no_a_scans);
k = 3;
% Display thresholded selected OCT image
scrsz=[50,50,600,600];
figure('Position',scrsz);
initial_image = a_scans(:,:,k);
subplot(3,2,1), imagesc(horizontal_scale, vertical_scale, initial_image);
xlabel('Pixels')
ylabel('Imaging depth (mm)')
title('(a) OCT image after filtering')
axis tight
pause
% Select an A-scan to process
j = 300
% obtain the average of selected a_scan from all images
avg_image = mean(a_scans,3); % average on third dimension
avg_a_scan = avg_image(:,j);
a_scans_sig=a_scans(:,j,k);
subplot(3,2,2), plot(vertical_scale, a_scans_sig)
xlabel('Imaging depth (mm)')
ylabel('Pixel value (a.u.)')
axis tight
title('(b) one sample depth-scan envelope')
grid on
pause
%Obtain and plot variance of filtered A-scan in windows of size 3 pixels
window_size =3;
half_window_size = floor(window_size/2);
Var_value=zeros(size(a_scans,1),1);
 for i = half_window_size + 1 : (no_a_scan_pixels - half_window_size)
    window_a_scans_sig = a_scans_sig(i - half_window_size : i +
half_window_size);
    Var_value(i,1)=mean(window_a_scans_sig.^2)-(mean(window_a_scans_sig)).^2;
%obtain variance of averaged A-scan in window of size 3 pixels using:
Var=E[s^2]-(E[s])^2
 end
subplot(3,2,5), plot(vertical_scale,Var_value)
axis ([0 max(vertical_scale) min(Var_value)
max(Var_value)+0.1*max(Var_value)])
xlabel('Imaging depth (mm)')
ylabel('Variance (a.u.)')
title('(e) Depth-scan contrast ')
grid on
% obtain the covariance of selected a_scan from all images
a_scan_cor_matrix = zeros(no_a_scan_pixels);
a_scan_cov_matrix = zeros(no_a_scan_pixels);
for kk = 1 : no_images
        a_scan_cor_matrix = a_scan_cor_matrix + a_scans(:,j,kk) *
a_scans(:,j,kk)'; % correlation matrix
end
a_scan_cov_matrix = (a_scan_cor_matrix/no_images) - (avg_a_scan *
avg_a_scan');  % subtract outer product of mean

% Obtain and plot average A scan power
avg_a_scan_power = a_scans_sig .* a_scans_sig;
```

```
% Obtain and plot average noise power
a_scan_noise_power = diag(a_scan_cov_matrix,0)
pause
subplot(3,2,3), plot(vertical_scale,a_scan_noise_power);
title('(c) Depth-scan noise power')
xlabel('Imaging depth (mm)')
ylabel('Pixel value (a.u.)')
axis tight
grid on
pause
% plot signal to noise ratio
snr_dB = 10 * log10(avg_a_scan_power ./ a_scan_noise_power);
snr_dB(isnan(snr_dB))=0;
snr_dB(isinf(snr_dB))=0;
subplot(3,2,4), plot(vertical_scale, snr_dB)
xlabel('Imaging depth (mm)')
ylabel('SNR (dB)')
title('(d) Depth-scan SNR')
axis ([0 max(vertical_scale) -10 max(snr_dB)+8])
grid on
pause
%obtain CNR
a_scan_noise_power=round(a_scan_noise_power);
Figure_merit=Var_value./a_scan_noise_power;
Figure_merit(isinf(Figure_merit))=0;
Figure_merit(isnan(Figure_merit))=0;
subplot(3,2,6), plot(vertical_scale, Figure_merit)
hold on ,plot(vertical_scale,Figure_merit_before_filt,'r')
legend('CNR after filter','CNR before filter','Location','best')
max1=max(Figure_merit);
max2=max(Figure_merit_before_filt);
dd=abs(max2-max1);   %use to define the range of yaxis in plot
axis ([0 max(vertical_scale) min(Figure_merit) 0.1*max1+max1])
title('(f) Depth-scan CNR')
xlabel('Imaging depth (mm)')
ylabel('CNR (a.u.)')
grid on

%obtain mean of SNR
% Figure_merit is CNR
[x y]=find(isnan(snr_dB_before_Filt));
snr_dB_before_Filt(x,y)=0;
m=snr_dB_before_Filt(find(snr_dB_before_Filt~=0));
mean_before_filter=mean(m)

[x y]=find(isnan(snr_dB));
snr_dB(x,y)=0;

m=snr_dB(find(snr_dB~=0));
mean_after_filter=mean(m)

m=Figure_merit(find(Figure_merit~=0));
mean_Figure_merit=mean(m)
```